An advanced prototyping process for highly accurate models in biomedical applications

Von der Fakultät für Ingenieurwissenschaften, Abteilung Maschinenbau der
Universität Duisburg-Essen
zur Erlangung des akademischen Grades

DOKTOR-INGENIEUR

genehmigte Dissertation

von

Timon Mallepree
aus
Velbert

Referent: Prof. Dr.-Ing. Diethard Bergers
Korreferent: Associate Prof. Dr. Ian Gibson
Tag der mündlichen Prüfung: 23.02.2011

Vorwort

Die vorliegende Arbeit entstand während meiner Tätigkeit als wissenschaftlicher Mitarbeiter, an der Professur für Produktionstechnologie und Produktentwicklung - Fakultät für Ingenieurwissenschaften - der Universität Duisburg-Essen.

Mein besonderer Dank gilt Herrn Univ.-Prof. Dr.-Ing. Diethard Bergers für die Betreuung und die wissenschaftliche Unterstützung meiner Arbeit. Ihm möchte ich sehr herzlich für sein Vertrauen und seine wohlwollende Förderung danken, die maßgeblich zum Erfolg dieser Arbeit beigetragen hat.

Herr Associate Prof. Dr. Ian Gibson ist tätig an der National University of Singapore und ist Mitbegründer der *Global Alliance of Rapid Prototyping Associations* (GARPA). Für die Übernahme des Korreferats und das Interesse an meiner Arbeit möchte ich mich herzlich bedanken.

Teile des Inhalts der Arbeit wurden im Rahmen des DFG-Forschungsprojekts *„Klinische und experimentelle Untersuchungen zur Morphologie und Dynamik des Nasen-Lumens und deren Einfluss auf Atemströmung und Klimatisierung der Atemluft“* in interdisziplinärer Kooperation erstellt. Allen Projektpartnern möchte ich ausdrücklich für die gute Zusammenarbeit und die freundliche Unterstützung danken.

Herrn Reinhard Giese und Herrn Klaus Werner möchte ich für die uneingeschränkte Unterstützung bei den Laborarbeiten danken. Den studentischen Mitarbeitern Herrn Adrian Czaykowski und Herrn Felix Sbrzesny danke ich für ihren engagierten Einsatz der wesentlich zum Erfolg der Arbeit beigetragen hat.
Ferner bedanke ich mich bei den Herren Dr.-Ing. Jörg Lubnau, Dr.-Ing. Jens Standke und Dipl.-Ing. Oliver Kower für deren Unterstützung und stete Diskussionsbereitschaft.

Besonderer Dank gebührt meiner Familie für die liebevolle Unterstützung und das immerwährende Verständnis für meine zeitliche Inanspruchnahme.

Duisburg, Februar 2011 Timon Mallepree

Contents

Glossary

Abbreviations

2D	Two-dimensional
3D	Three-dimensional
A_n	Agger nasi
ASCII	American standard code for information interchange
CAS	Computer-assisted surgery
CAD	Computer-aided design
CAM	Computer-aided manufacturing
CFD	Computational fluid dynamics
C_i	Concha inferior
CLDATA	Cutter location DATA file
C_m	Concha medius
CMB	Controlled metal build-up
CMM	Coordinate measurement machine
CNC	Computerized numerical control
C_s	Concha superior
CT	Computed tomography
DICOM	Digital imaging and communications in medicine
ENT	Ear, nose, and throat
FDM	Fused deposition modeling
FOV	Field of view
FWHM	Full width at half maximum
gpp	Post-processor file SolidCAM
H_{sl}	Hiatus semilunaris
HU	Hounsfield units
I_e	Infundibulum ethmoidale
IGES	Initial graphics exchange specification
LI	Linear interpolation algorithm
LLM	Layer laminate manufacturing
mac	Post-processor file SolidCAM
MC	Marching cube
Mimics	Materialise's interactive medical image control system
MPP	Medical prototyping process
MRI	Magnetic resonance imaging
NC	Numerical control

M_{ni}	Meatus nasi inferior
M_{nm}	Meatus nasi medius
M_{ns}	Meatus nasi superior
NCG	German NC-Gesellschaft
NURBS	Nonuniform rational B-splines
PC	Personal computer
PCP	Positioning and clamping principle
PIV	Particle image velocimetry
PMMA	Polymethylmethacrylate
P_u	Processus uncinatus
RAM	Random access memory
RE	Reverse engineering
RPM	Revolutions per minute
RP	Rapid prototyping
SLA	Stereolithography
S_n	Septum nasi
STEP	Standard for the exchange of product model data
SLS	Selective laser sintering
STL	Standard triangulation language
VDID	German industrial designer union
VP	Virtual prototyping
VR	Virtual reality
VRML	Virtual reality modeling language

Symbols

α	Intersection-point
a_e	Radial cutting depth
a_p	Axial cutting depth
axD_i, ayD_i	Centre of circles
Å	Wavelength
b	Pixel
C	Collimation
cm^2	Square centimeter
D	Tool diameter
D_i	Radius

D_w	Detector width
GB	Gigabyte
Ghz	Gigahertz
g/cm^3	Gram per cubic centimeter
f_i	Feed
$\vec{g}$	Gradient vector
kB	Kilobyte
kV	Kilovolt
l	Measuring length
MB	Megabyte
mm	Millimeter
µm	Micrometer
µ	Absorption coefficient
π	Pi
R_a	Average surface finish
S_i	Slice increment
S_n	Nose model slices
σ	Standard deviation
T	Threshold
t	Iso value
v_c	Cutting rate
v_f	Feed rate
V_i	Normal vector
v_i	Voxel
W_i	Angle (test model)
X_n	Test model slice
xs, ys	Seed point
y	Profile deviation

1. Introduction

Planning surgery for surgical intervention, to evaluate the success of an executed surgical intervention, is among keys factors necessary for ensuring quality of minimally invasive surgery. The field of medicine dealing with computer-aided preparation of surgical interventions, which assists medical interventions such that they are as minimally invasive as possible, requires further research.

The worldwide demand for cutting-edge medical engineering technologies has created an impetus in today's research to launch revolutionary technologies. Specifically, enhanced support processes for high precision in diagnostics, surgery planning, and patient treatment are in demand. In ear, nose, and throat (ENT) surgery, complex defects and unknown processes remain to be discovered, e.g., the physiology and pathophysiology of human nasal breathing. Medical modeling allows researchers to obtain knowledge about complex formal structures within the human body and makes spatial analysis of structures and their effects on flow processes (e.g., nasal airway) possible. Moreover, model-based planning procedures support the analysis of final surgical outcomes with respect to patient-specific computer-assisted surgery (CAS) planning.

Medical modeling techniques, known as biomodeling, provide the possibility to reconstruct three-dimensional (3D) models of anatomical templates of the human body. Reverse engineering (RE) technologies for capturing anatomical structures are available and include: computed tomography (CT), magnetic resonance imaging (MRI), and laser scanning (Hieu & Zlatov et al., 2005). Along with the development of medical image scanning technologies, rapid improvements in medical image processing have revolutionized the planning of medical surgery. Since Alberti (Alberti, 1980) first published the notion of generating 3D models via CT images, research has resulted in high quality processes for generating spatial structures of the human anatomy. In the meantime, technologies such as virtual prototyping (VP) and rapid prototyping (RP) have come into focus for processing reconstructed 3D medical image data. New medical perspectives have been provided by computer-assisted 3D diagnostic and treatment planning, simulation of surgery, 3D design of individual implants (Eufinger et. al, 1995; Hierl et al., 2006) and the connection between 3D techniques and navigation (Kliegis, Ascherl, Kärcher, 1995; Gibson et al., 2006; D'Urso et al., 1999; Truscott, & de Beer, 2007). In the past, 3D visualization of medical image data was only possible on computer screens and was therefore insufficient for surgeons who were more familiar operating with complex 3D geometries. Several steps have been made to process real 3D visualizations of medical models using VP and RP technologies (Hieu et al., 2005; Beneke, Metzen, Bergers, 2003; Mankovich, Cheeseman, Stoker, 1990). Today's VP and RP applications are instrumental for shortening product development processes. In 1987, it was considered a success to generate 3D RP models by applying a single process of operations to computer

data (Gebhardt, 2003). Today, however, it is possible to produce technical prototypes using almost fully automated processes. Medical models are dimensionally accurate models of human anatomy generated by means of medical image data, using a medical imaging system (e.g., CT). They offer surgeons important and state-of-the-art technological aids for various medical applications. Virtual reality (VR), as a VP tool, has found many useful applications in computer-assisted surgery, as well (Cai et al., 2004; Gibson et al., 1997; Klein et al., 2000). 3D visualizations can play an important role in presurgery planning in terms of supporting medical experts in navigating difficult anatomically shaped geometries.

To date, results in the field of RP have mainly been made in response to industrial and mechanical engineering demands (Gibson et al., 2006). In such typical engineering processes as the manufacturing of technical prototypes, 3D CAD (computer-aided design) data are available and form the basis for RP. In order to reconstruct facsimiled medical models of existing anatomical parts, the process of producing RP models does not begin with the preparation of an already fully defined 3D CAD model, but with the generation of 3D models by RE. To generate a 3D model, medical image information about a specific part is needed. A technique is needed to process this image data for the generation of 3D models. The medical modeling technique known as biomodeling provides the possibility to reconstruct 3D models of anatomical templates of parts of the human body. To date, most studies investigating the analysis and application of medical image data are restricted to either visualization, and the required model reconstruction algorithms (Shi et al., 2006; Kalender, 1995), or to post-application tasks (Hieu & Zlatov et al., 2005; Gibson et al., 2006). These important studies have not focused on addressing the precise parameters needed in the overall process for VP and RP, with respect to generating complex anatomical models. Therefore, a VP and RP procedure needs to be developed such that it integrates the whole run of capturing medical image data to deriving accurate virtual and physical volume models.

The present thesis aims to develop a prototyping process in medicine that enables the generation of medical models. To support this, a classification of RP and VP procedures in the field of medical applications is set up. The capabilities of virtual and physical models in surgery planning are demonstrated by introducing a concept of how medical models support CAS. An unsolved problem in manufacturing medical models using RP technologies is the accuracy of the reverse engineered and subsequently manufactured RP models (Gibson, 2005b; Gibson et al., 2006). This issue has been dealt with in some previous studies. Lill et al. (1992) reconstructed a CT model from a real skull, and fabricated a physical model by milling hardened polyurethane foam. The reconstructed model deviated from the original skull by 1.47 mm on average. A study by Barker et al. (1994) analyzed the dimensional

accuracy of an RP model replicated from CT scanning of a bone skull and determined a mean difference of 1.9 mm. Further investigations of Wulf et al. (2001) have demonstrated that it is possible to achieve mean deviations of ± 0.79 mm using medical images from scans with 1-mm slice thickness and the RP procedure of stereolithography (SLA). The study of Choi et al. (2002) investigated the failures generated during the fabrication of a skull RP model. The average error was 0.62 mm. These former studies on the accuracy of medical RP models have not dealt with different scan protocols in evaluating possible deviations. They have also not differentiated between possible sources of error, such as the imaging system used, the 3D reconstruction process, and the manufacturing procedure. Previous investigations did not quantify the relative contribution of geometrical form to total deviation of a model. An additional limitation is the accuracy of triangulation procedures in 3D reconstruction. According to Giannatsis (2007), the virtual model construction phase contributes considerably to observed inaccuracies. The complete procedure and its related parameters of virtual model generation are of interest in order to provide accurate and reliable medical models for medical prototyping procedures.

Complex individual anatomical models have traditionally been reproduced with additive RP procedures, which result in models of limited translucency and accuracy. Recent studies have introduced a general methodology for applying RP to specific research areas of biomedical fluid mechanics (Hopkins et al., 2000, Chong et al., 1999, Kim, 2004). For instance, De Zélicourt et al. (2005) used the additive RP procedure of stereolithography to study a specific case of cardiovascular fluid dynamics. However, the resulting level of translucency was rather poor. This situation would demand the use of a procedure that enables the generation of translucent models for fluid analysis. The subtractive method most ideally suited to this is computer numerically controlled (CNC) machining (Petzold et al., 2005, Liu et al., 2006). Therefore, former studies of Hastrich (2006) are ongoing in order to generate anatomical free-form surfaces of full transparency. Specific milling parameters are being evaluated to obtain a fully transparent model. In practice, experimental studies are being performed to obtain decisive parameters for a computer-aided manufacturing (CAM) procedure that will enable the derivation of machine code for milling accurate, complex-shaped anatomical surfaces.

First, the present thesis describes the use of prototyping an anatomically correct human nose by means of validated process parameters. Several studies (Kim, 2004; Croce et al., 2006; Shi, 2006; Hörschler et al., 2006; Finck et al., 2007; Hopkins et al., 2000; Schreck et al, 1993; Hahn et al, 1993) have attempted to produce a medical RP or VP model of the human nose to enable the analysis of nasal anatomy and airflow behavior. This includes contributions to our knowledge of the nose's conditioning of inspired air and particle

distribution. However, several limitations have been identified related mainly to inconclusive accuracy and process parameters in model generation. Literature dealing with medical nose models has traditionally used tomographic slices spaced 2 or 4 mm apart (Hopkins et al., 2000, Schreck et al, 1993, Hahn et al, 1993). Such large slice increments introduce a degree of generalization in the final outcome. In small and thin regions (e.g., the ostium connecting the main nasal airway to the sinuses) or in thin regions of the nasal cavities, abrupt changes in the airway (e.g., the vestibule or the turbinate heads) occur. A 3D reconstruction made from evaluated tomographic images using determined parameters could prevent capturing anatomical features in sufficient detail. Croce et al. (2006) used a plastinated specimen of the nasal cavities and maxillary sinuses in order to perform flow analysis experimentally. One important restriction of this study was that it was not possible to vary different anatomical configurations, in terms of comparing the situation before and after surgical treatment. In contrast the present thesis introduces an RP method that enables analysis of different nasal airway configurations, by exchanging focused layers of the model that represent the region of interest. A transparent facsimile model using RP is generated respecting nasal human airways including left and right nasal cavities and ostia that connect sinuses to upper airways.

Prototyping of the human hip is the second example whereby validated process parameters are used. Various studies have dealt with human hip models for surgical planning and biomechanical engineering (Kang et al., 2002, Verdonschot et al., 1993, Handels et al., 2000). Previous work mainly relates to simulation and biomechanics (Verdonschot et al., 1993, Kang et al., 2002, Jourdan & Samida, 2009) or visualization and presurgery planning (Handels et al., 2000, Lee et al., 2007, Said et al., 2008). As a result, complete process parameters are not focused upon in these studies. A valid statement about the accuracy of medical hip models is also missing. The present thesis sets out to address this issue by presenting accurate prototyping of medical hip models.

Chapter 2 presents state-of-the-art in biomodeling, RP, and VP. The focus of this chapter is concentrated on limitations in medical image data processing and related applications that arise due to unspecified process parameters. Further, taking into account the different process steps stated in Chapter 2, specific demands on RP and VP for medical use will be formulated in Chapter 3. These proposed demands form the basis for developing an integrated concept of how RP and VP can be embedded in fields of application in medicine (Chapter 4). A complete process development for processing medical models by RP and VP is presented in Chapter 5. Complex anatomical models are in the focus of interest. Subsequently, the presented process is applied to the virtual and physical modeling of the human nose and human hip, exemplified in Chapters 6 and 7.

2. Prototyping in biomedical engineering

“Biomedical engineering integrates physical, chemical, mathematical, and computational sciences and engineering principles to study biology, medicine, behavior, and health. It advances fundamental concepts; creates knowledge from the molecular to the organ systems level; and develops innovative biologics, materials, processes, implants, devices and informatics approaches for the prevention, diagnosis, and treatment of disease, for patient rehabilitation, and for improving health (NIH, 1997).”

Biomedical engineering is a fast-paced discipline that provides products that serve modern medicine. Specifically, biomedical products support diagnosis, therapy, and scientific research. To meet high medical standards, various demands exist for biomedical products. Typical standards such as function, ergonomics, and cost efficiency are subject to the highest demands on accuracy and surface finishes. RP and VP technologies can be useful instruments in biomedical engineering for producing physical and virtual medical models for various medical applications. RP encompasses a wide range of technologies and applications which involve the manufacturing of free-form-shaped geometries as rapidly and efficiently as possible. The various definitions of RP mainly converge in stating that RP is a technology that allows fast and automated fabrication of physical objects directly from virtual 3D CAD data without significant process planning related to part features and geometry (Grimm, 2004; Gibson, 2005; Bergers, 2009a). Further, RP is called “rapid” because it can prototype parts very rapidly in many cases, that is, in hours rather than in days or weeks (Noorani, 2006). Such descriptions of RP emphasize the strength of RP in rapidly fabricating models of any shape, by making virtually generated models tangible. Such demands can be met by the wide range of uses made available by RP, for medical applications. The most important applications for medicine are the design, development, and manufacturing of medical models and instrumentations (Noorani, 2006), which succeed the production of virtual and physical anatomical models for presurgery planning. The present RP process in manufacturing models for applications in early stages of product development processes consists of three main processes (Sauer et al., 2004). These processes are the process of data generation, data processing and data use (Fig. 2-1). The first process generates needed starting data that are the basis for succeeding operations. There are two possibilities for data generation. One possibility is to carry out a RE process in order to generate model data. A possible field of use is medicine, whereby two-dimensional (2D) medical images are generated by tomography devices (e.g., CT scanner). An additional way of generating model data is the design of a model using a 3D CAD system in order to create 3D model data. The typical field of generating parts or assembly groups with CAD systems is that of engineering.

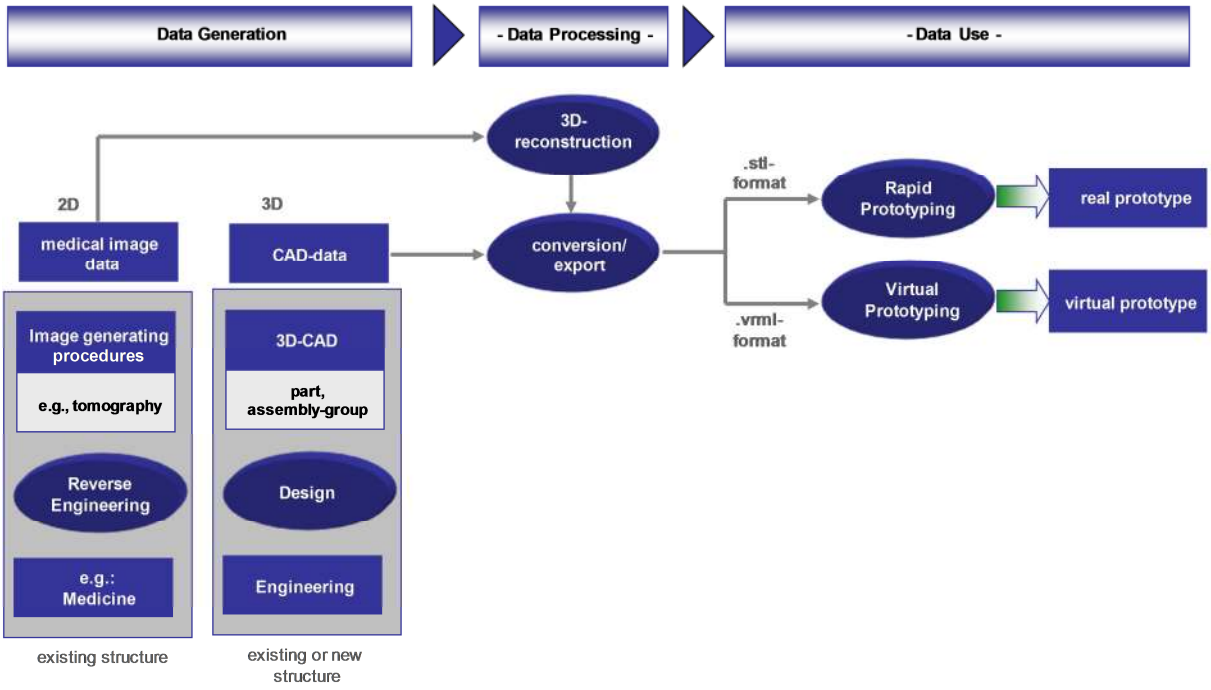

Figure 2-1: RP and VP (adapted from Sauer et al., 2004).

The process of data processing contains the needed data conversion in order to generate either .STL (standard triangulation language) files for RP processes or .VRML (virtual reality modeling language) files for VP operations.

To date, RP and VP applications are used mainly in product development processes as shown in Figure 2-2. RP is used in all phases of the product development process. The product development process, sales, and service are also supported by VP applications. RE applications support data acquisition during planning and concept phases of product development. Possible failures in early stages of the product development process can be detected more easily using RP and VP. Especially, before a product is intended for series production, possible changes in the definition of the product have to be identified to reduce costs for later adjustments.

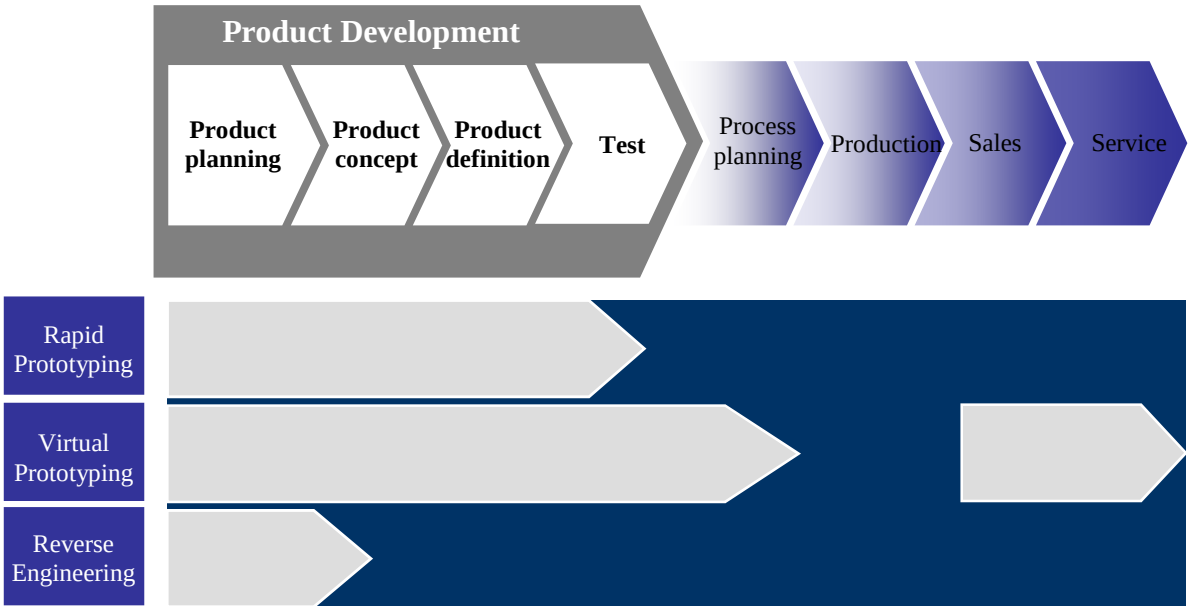

Figure 2-2: Prototyping in product development (Bergers, 2009a).

The benefits of using RP and VP in supporting the product development process are reduced lead times to generate models, improved ability to visualize geometry due to physical existence, earlier detection and reduction of design errors, and increased capability to estimate properties of parts and models. Especially in medicine, these benefits are necessary but often missing.

2.1 Biomodeling

Medical models are generated from patient data that are derived from computerized medical imaging (CT, MRI, ultrasonic imaging, etc.). The two main tomography techniques are CT and MRI. CT technology is normally used for bony tissues, while MRI scans generate images of soft-tissue regions (Gibson, 2005). A comparison of the advantages and disadvantages of MRI and CT scanners is situation-dependent. In terms of image data processing, the standardized image intensity (Hounsfield units) of CT data (Chapter 2.1.2.2) is relatively easier to process than MRI data, where the intensity can vary from protocol to protocol. In MRI, this can lead to difficulties in detection of organ boundaries (Bartz, 2005) and is a disadvantage for 3D reconstruction processes. However, MRI has advantages in scanning soft tissues and does not apply radiation to patients. Summarizing the advantages and disadvantages of CT and MRI imaging, CT technique enable the generation of images with an intensified representation of tissue boundaries. This is because threshold settings in segmentation can be applied more precisely, reducing possible model deviation. Therefore, the present thesis refers to content and developments based on CT imaging.

The process of medical RE encompasses the following three process steps:

- Tomographic scan (CT)
- Segmentation and 3D reconstruction
- Conversion to RP data format (.STL) or VP data format (.VRML)

The objective of running these process steps is to obtain a complete representation of part of a patient's body as a 3D model in.STL file or .VRML file format. Further application of these data supports VP or RP.

2.1.1 Anatomical terminology

When referring to medical imaging of human anatomy the relative positions of organs, extremities, and other specific features are only useful if the body is in a known position. It is standard to assume that the body is in position when describing relative positions of anatomy. The principal axis of the human is through the centre of the body running from head to feet; this is referred to as the long axis (Fig. 2-3).

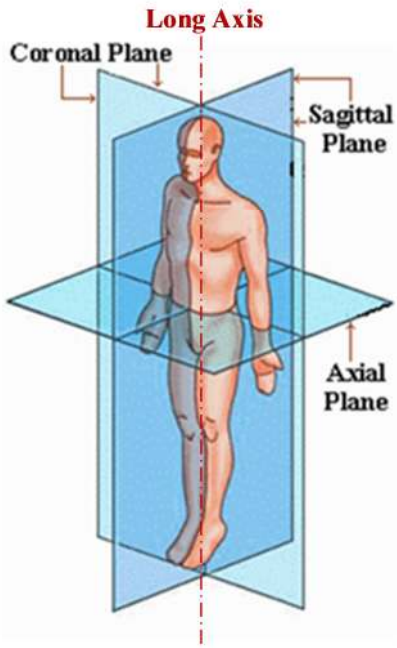

Figure 2-3: Anatomical planes (adapted from Spinuniverse, 2009).

Once the anatomical position is set, perpendicular planes divide the body. The transverse plane which runs through the body perpendicular to the long axis is defined as the axial plane. The coronal and sagittal planes lie perpendicular to the axial plane. Thus, the final defined position of the part of interest allows capturing human anatomy in all three dimensions.

2.1.2 Medical imaging

The process of obtaining CT data for later 3D reconstruction begins with the selection of an appropriate scan protocol related to the reconstruction case in question. Once a patient's body is positioned in the scanning machine according to the body part concerned, a scan protocol has to be determined (Fig. 2-4). A volume scan is initiated and is followed by an internal slice interpolation process that generates a set of image slices.

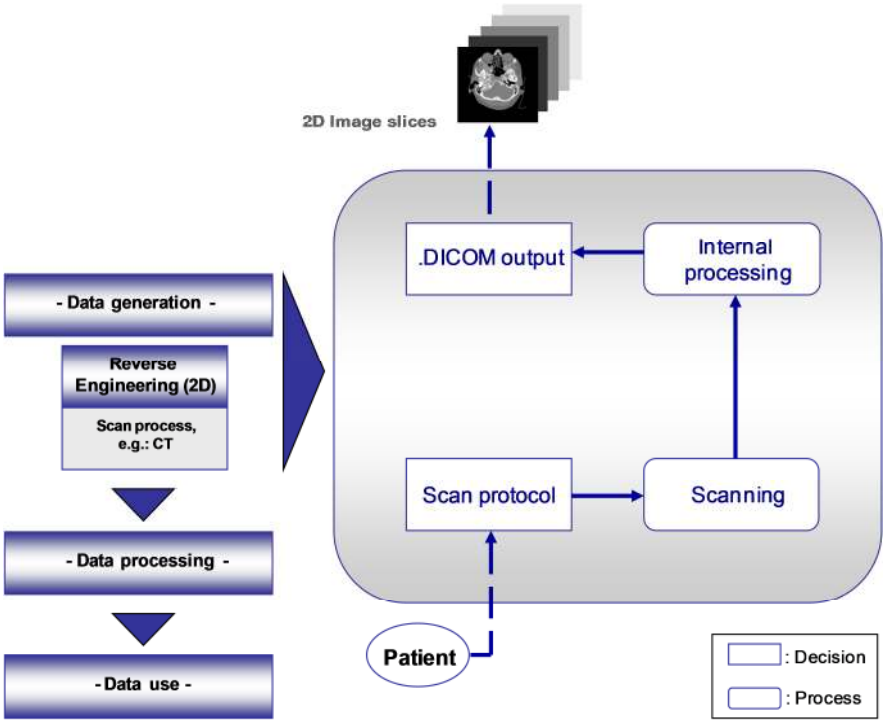

Figure 2-4: Reverse engineering in medicine

Finally, a complete set of 2D images ready for later 3D reconstruction is generated. The output format of these images is .DICOM (digital imaging and communications in medicine) format (see Chapter 2.1.5).

2.1.2.1 CT Scanning

Today's spiral CT technology, which was invented in the early 1990, represents a fundamental step in the generation of volume scans. However, such technology only permitted scans of one slice at one time. The main disadvantage of single-slice CT technology lies in the unsatisfying volume coverage in the longitudinal direction (z-direction). In 1998, the principle CT manufacturers introduced multislice CT scanners to the market, which enabled simultaneous scanning of various slices. Today, CT scanners can scan up to 64 image slices per rotation (e.g., Siemens Somatom Definition with 64 detector arrays). Moreover, such developments permit scanning at a higher resolution in the longitudinal

direction. Nevertheless, appropriate scanning parameters need to be set in order to provide accurate data sets for 3D reconstruction. The principle of X-ray technology involves using a short wavelength of light to penetrate a material under consideration. X-rays are electromagnetic radiations having wavelengths ranging from 100 to 0.01 Å (Noorani, 2006). The shorter an X-ray's wavelength is, the greater its energy and power of penetration. An X-ray is generated whenever high-voltage electrons strike a material object. The absorption of X-radiation by any substance depends strongly on its density and atomic weight (Noorani, 2006). The CT is one of the most important tools in radiology today, even in industrial RE processes. After Radon pronounced the basic mathematical principles of X-ray technology, the time was ripe to introduce the first CT machine, late in the year 1970 (Prokop et al., 2006).

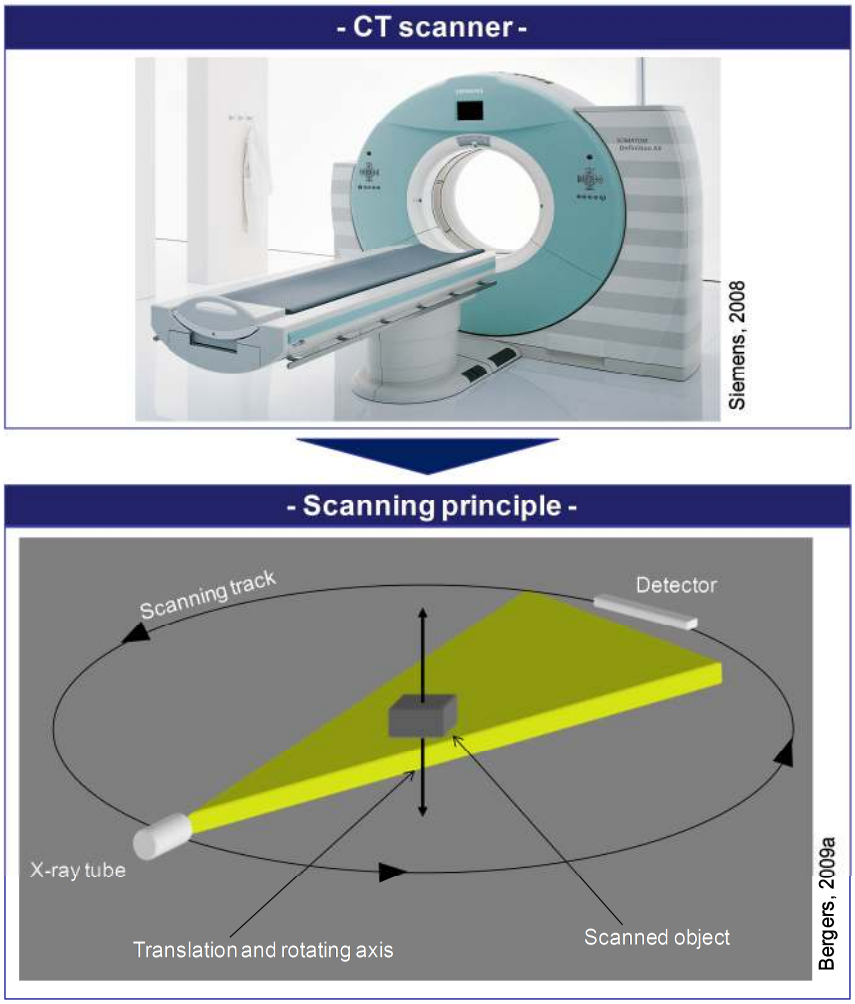

Figure 2-5: CT Scan process (adapted from Siemens, 2008; Bergers, 2009a)

A CT machine involves an X-ray that scans a patient from different directions (Fig. 2-5). Through a process of parallel collimation, X-rays are formed into a thin fan, which then defines appropriate slice thickness (Prokop et al., 2006). After the X-ray fan has crossed the considered body part, the transmitted X-rays are captured by detectors. With the use of inverse Radon transformation, local radiation is reconstructed for every point in the scanned

slice. The local absorbed radiation dose is then calculated as so-called “CT values” (Prokop et al., 2006).

Figure 2-6: CT Internal reconstruction process (adapted from Prokop et al., 2006)

In the scanning process, 500–1500 different absorption values are captured by the scanner for each position of the tube and each detector row to generate an absorption profile for obtaining the raw data (Fig. 2-6). The internal image reconstruction starts with the definition of the considered field of view (FOV). In this way, each ray traveling from the tube to the detector is captured. The objective is to project all rays backwards by collecting all of the different rays together that are captured (Prokop et al., 2006). The result is a undefined washy image. In order to rework an unfinished image, several rays are combined into one projection to filter the emerging absorption profile with an edge, stressing mathematical convolution. This so-called reconstruction filter allows setting spatial resolution and image noise by varying between smooth and high resolution (Fig. 2-6).

The reconstruction filter, a kernel function, enhances high-contrast or low-contrast structures. Therefore, the kernel needs to be adjusted to the object of interest. For example, in cases, where bony structures are most important, a kernel with strong edge-enhancing characteristics should be selected to visualize small gaps. For the differentiation of soft tissue structures (e.g., muscles and mucosa) a kernel with a lower local frequency filter and smoothing features has proved to be efficient (Falk et al., 1995). There are several manufacturers (e.g., Siemens, Toshiba) that sell CT scanners, which use their own specific reconstruction filters, and these are not made public. After using an appropriate reconstruction filter, CT values are coded in gray values to present a gray value-generated image. After the internal reconstruction, voxel-based data sets are available (Fig. 2-5). In order to obtain an appropriate data set for 3D reconstruction arbitrary scan parameters have to be selected.

2.1.2.2 3D Acquisition parameters

The acquisition of medical image data by medical imaging scanners depends on a defined scan protocol. Raw data are generated in the scanning machine in terms of deriving .DICOM data that contain the scanned medical image slices. The objective is to process the .DICOM data by specific segmentation methods along a 3D modeling process.

In the discovery and evaluation of appropriate parameters for deriving 3D geometry data, the acquisition of useful data must be ensured using a scan protocol. The following parameters have to be evaluated before scanning begins:

(1) Scanner determination
(2) Scan direction and position
(3) Resolution
(4) Field of view (FOV)
(5) X-ray dose (CT)
(6) Slice thickness
(7) Slice increment
(8) Filter algorithm

In the imaging of bony structures, CT has a distinct advantage because of the large difference in attenuation between bones and soft tissues (1). Although the soft tissue contrast in CT is less optimal for 3D reconstruction than MRI, CT has its advantage in tissue structures where there is a large difference in attenuation values, for example, in air-containing structures such as the nasopharynx, trachea, and larynx (Kung & Fung, 1994). Therefore, CT imaging technology is selected as the appropriate application in the present thesis. The scan direction and position depends on the particular situation (2). The resolution (3) depends on the image matrix that has to be set. A CT image consists of a quadratic image matrix that can contain between 256×256 and 1024×1024 pixels but is normally defined by 512×512 pixels. A higher resolution corresponds to a higher X-ray dose (5), and this has to be preset. The typical value set for head and body scanning is 120 kV (Somatom Sensation, Siemens). Each scanned slice is defined by a specific thickness (6). The end result is that every single pixel has been transformed into a voxel (Fig. 2-7).

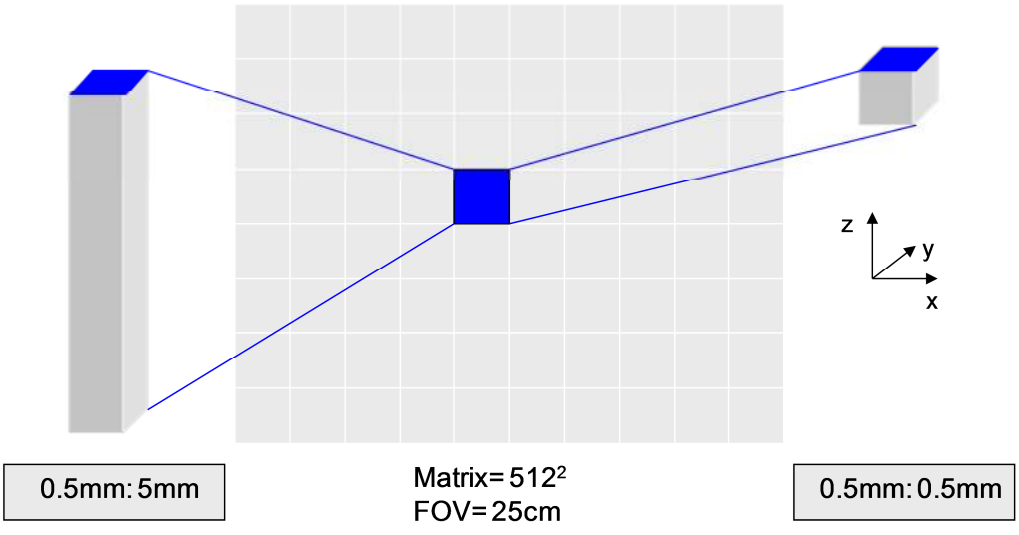

Figure 2-7: Voxel and slice thickness (adapted from Prokop et al., 2006)

The size of a voxel follows from the chosen matrix size, the set FOV (4), and the defined slice thickness (Prokop et al., 2006). In most cases, the voxel is formed like a bar. The consequence is that the pixel size is orientated on the slice plane (*x*–*y* plane) 5–10 times smaller than the slice thickness (z-direction). That resulting unequally formed voxel (anisotropy) can be only improved by taking smaller slice thicknesses.

Along the reconstruction process every voxel is directed to a specific value, which represents the absorption coefficient (μ) for that particular voxel. The CT value is defined as follows, and is determined in Hounsfield units (HU):

$$CT = 1000 \times \frac{(\mu - \mu_{water})}{\mu_{water}} \qquad \text{(II-1)}$$

The Hounsfield scale begins at a value of –1000 for air, 0 for water, and is unlimited in the positive extent. The available range for a CT value depends on the specific machine and has to be differentiated according to bit depth, which is defined as bits per pixel, e.g., –1024 to 3071 HU have 12 bits. Figure 2-8 shows a CT scale exemplifying –1000 up to 3000 HU. Difficult to determine are the soft tissues including fat, low protein liquids, and fresh blood.

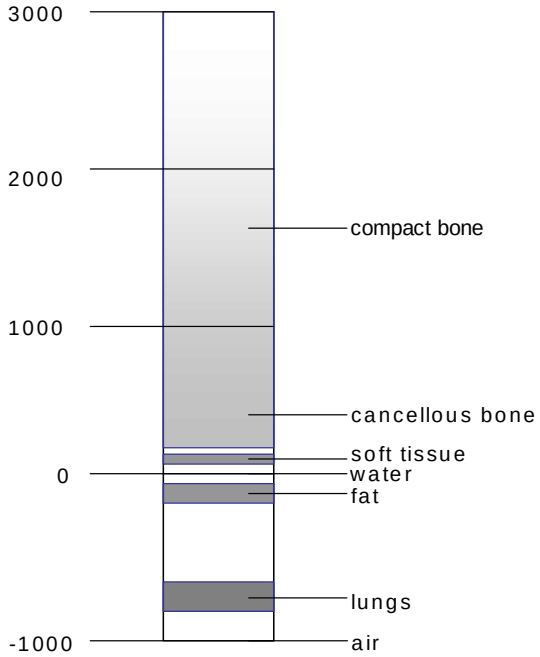

Figure 2-8: CT Value scale (adapted from Prokop et al., 2006)

In general, it is important to set characteristic CT values for typical scanned materials to allow an exact determination of the considered parts. The human eye is able to detect a limited amount of gray values ranging from approx. 40–100 gray values (Prokop et al., 2006). Therefore, the complete CT value scale is not represented along a CT scan such that the inability of differentiating structures with low density differences is avoided. Only a part of that

whole scale is shown in the CT window. Therefore, the window setting defines the range and level. That is, the range sets image contrast and the level sets brightness.

An important parameter to consider is nominal slice thickness (6) or slice collimation, which is determined by the appropriate collimation of the radiation dose during acquisition. As mentioned, the slice thickness determines the anisotropy of the resulting voxels. Therefore, the X-ray fan has to be adjusted. Every slice is determined by an X-ray composed of a divergent fan. To optimize the fan, additional apertures have to be installed to focus the slice profile (Fig. 2-9a). Because points that are not localized in the region of interest influence object points that are positioned in the region of interest, plan slices are not possible to scan. The degree to which an object point contributes to a slice is described by the slice profile (Fig. 2-9b).

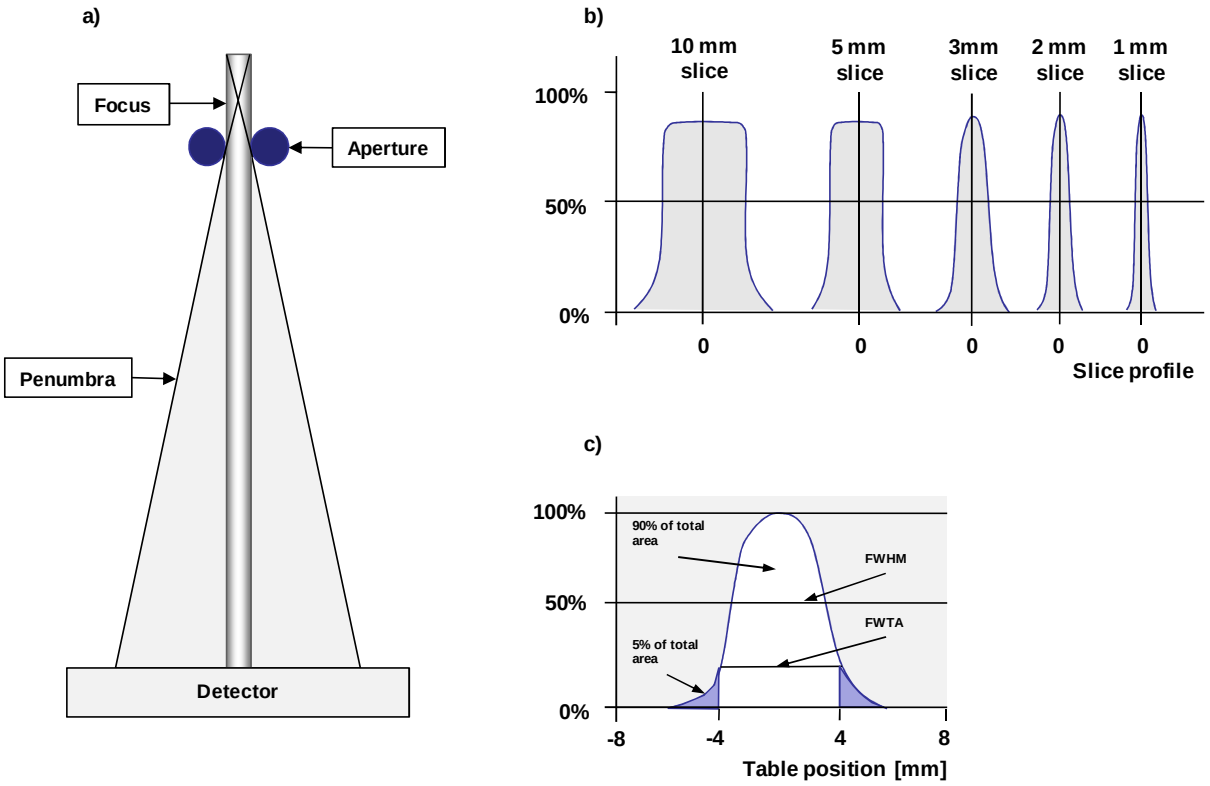

Figure 2-9 a-c: CT Slice profile (adapted from Prokop et al., 2006)

As Figure 2-9a shows, the ideal slice profile is a rectangle, the width of which represents desired slice thickness. Real slice profiles have a rounded form because related regions contribute to image composition (Prokop et al., 2006). As presented in Figure 2-9b, larger slices are not characterized by rounded angles to the extent that thinner slices are.

The full width at half maximum (*FWHM*) is normally specified as a measure of the width of the slice profile (Fig. 2-9c). This measure represents slice collimation or slice thickness (Prokop et al., 2006). The difference between slice collimation and slice thickness is related to the scanner type. Here, single-detector scanners and multidetector scanners may be

differentiated, in which various slices per rotation are scanned (see Chapter 2.1.2.1). In a single detector scanner, the width of the slice is determined by the collimator (Bushberg, 2002). As shown in Figure 2-10, a multidetector scanner scans various slices simultaneously (e.g., four slices shown in Fig. 2-10B). Here, the collimator determines the outer two edges of the scanned slices.

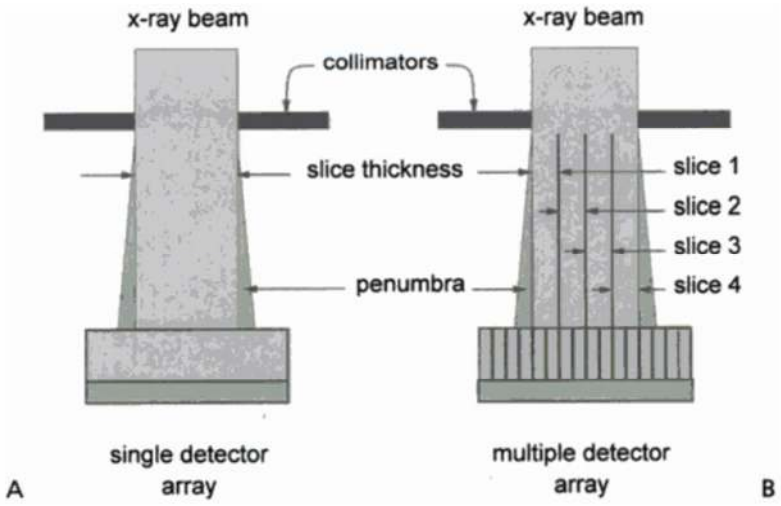

Figure 2-10: Slice thickness and collimation (Bushberg, 2002)

A related acquisition parameter is slice increment (7), which is the table transition distance during a 360° scan. In this context, the so-called pitch is an important parameter to set because it is pitch that finally generates radiation toward the patient and defines image quality. For single-detector scanners the pitch is defined as the collimator pitch (Bushberg, 2002):

$$Collimator\ pitch = \frac{table\ movement\ [mm]\ per\ 360°\ rotation\ of\ gantry}{collimator\ width\ [mm]} \quad \text{(II-2)}$$

A pitch less than 1 generates an image of higher quality but more radiation dose to the patient. A typical pitch used is 1.5 (Bushberg, 2002).
Scanners with multiple detector arrays need a corrected pitch definition (Bushberg, 2002):

$$Detector\ pitch = \frac{table\ movement\ [mm]\ per\ 360°\ rotation\ of\ gantry}{detector\ width\ [mm]} \quad \text{(II-3)}$$

Here, pitch is defined by detector width (D_w). The difference between single and multiple detector arrays is shown in Figure 2-11:

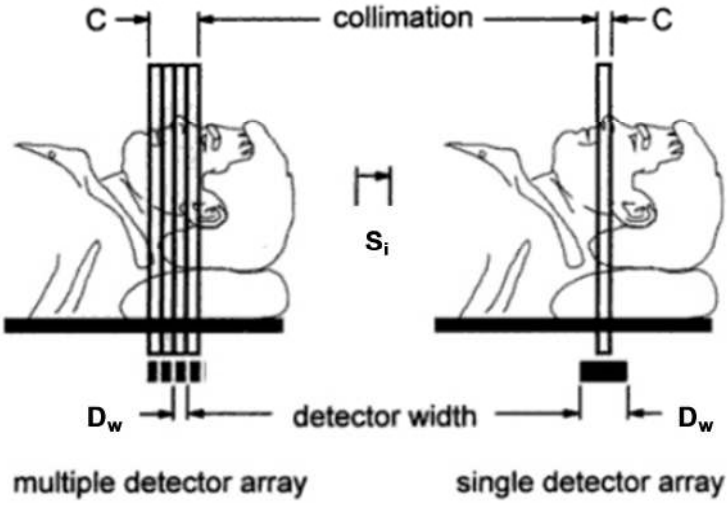

Figure 2-11: Pitch (adapted from Bushberg, 2002)

If S_i is the slice increment, C the collimation width, and D_w the detector width, the collimator pitch is defined as S_i/C and the detector width as S_i/D_w. For example, a detector pitch of 3 for a four-detector scanner is equivalent to a collimator pitch of 0.75 (3/4).

2.1.3 Segmentation of medical images

A digital image consists of a finite number of picture elements named pixels (Bergers, 2009b). These pixels are arranged vertically and horizontally on a grid representing differences in brightness (gray scale values). Medical images consist of gray scale values. For 3D reconstruction, a medical image data set has to be edited to commute the sequence into related regions or structures. In medicine, segmentation is the process of defining anatomical structures originating from tomographic image data. Segmentation arranges an image into regions of equal conditions (Wiltgen, 1999). Objects are localized and isolated (Bergers, 2009b), i.e., an image set is arranged into its constituent objects. But, the process of segmentation itself is normally not an end in itself. Instead, segmentation is preparatory for succeeding operations such as 3D reconstruction, the analysis of tissues, or the analysis of pathological images.

Before starting segmentation a preprocess of filtering has to be conducted. Especially in cases in which high resolution scans are needed the noise is often too high. In CT imaging, the noise level depends on the magnitude of X-ray dose. Appropriate filters are needed in order to reduce increasing noise. As shown in Figure 2-12, noise leads to rough images and later to rough surfaces.

Filters usually work as a kernel that can be visualized as an arbitrary set of points moving across an image (see Figure 2-12).

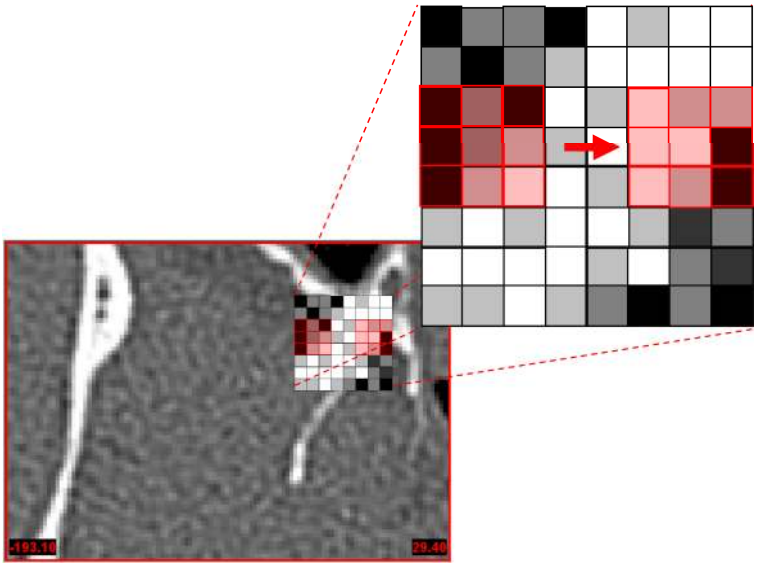

Figure 2-12: Image filtering

Pixels within the kernel are selected for filtering. Aside from this rather simplified classification, numerous modifications exist. (For explicit and technical reviews of filtering techniques, the reader is referred to: Preim & Bartz, 2007;; Russ, 2006; Bankman, 2000.)

In general, it is supposed that noise occurs at high frequency. Therefore, low-pass filters are used for noise reduction (Preim & Bartz, 2007). The design of these filters is based on suppositions regarding the amplitude and distribution of noise. There are several filtering approaches to in the literature.

Predefined noise reduction filters ensure that the mean gray value remains the same after the filter is applied. A typical noise reduction filter is the mean and Gaussian filter. The mean filter is applied by iterating over all pixels and replacing image intensity with a weighted average of neighboring pixels (Preim & Bartz, 2007). The Gaussian filter convolves the image with a Gaussian kernel in order to reduce the noise using a Gaussian distribution. The main problem with both noise reduction filters is that they are rather inflexible in terms of taking the full characteristics of an image into account; they typically smudge edges leading to a washy image. The difficulty of edge detection in segmentation is more difficult for this reason.

A noise reduction filter that leads to better edge detection is the so-called median filter, which takes into account image intensities of the local neighborhood. The median filter replaces the original gray value of a pixel by the median of gray values of pixels in the specified neighborhood. Instead of exchanging the pixel value with the mean of neighboring pixel values, the median filter replaces it with the median of those values (Dhawan et al., 2008).

An advanced filtering technique, curvature flow, attempts to remove noise from an image by maintaining boundaries. Curvature flow filtering is a method used for both smoothing and

enhancement and is based on curvature flow interpretation of the geometric heat equation (Malladi & Sethian, 1995); smoothing is realized by diffusion, which is controlled by minimum and maximum criterion that are determined in reference to local gradient and curvature. Diffusion results when local image brightness diffuses due to a concentration difference with neighboring pixels. Once a level is set such that all noise below that level is removed, all features above that level will be preserved (Sethian, 1996). Diffusion speed is proportional to the curvature of the contours. Therefore, the higher the time is set for selecting the gradients, the more details that are smoothed in an image. And conversely, the lower the time is set, the slower the computation of level-set evolution, and the more details that are preserved.

In any case, the problem remains that resolution will decrease if a smoothing operation is carried out. Applying smoothing filters results in a smooth image but details are ultimately reduced (Fig. 2-13).

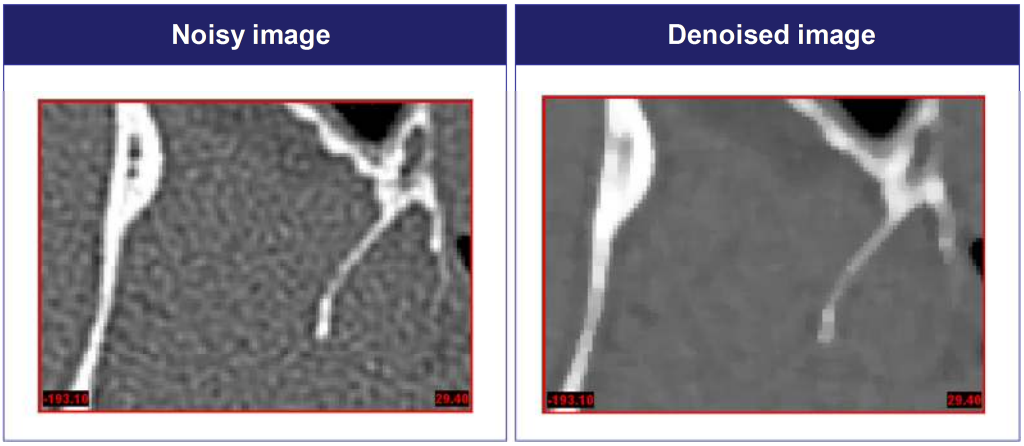

Figure 2-13: Image noise

The conclusion is that the higher the native contrast difference is, the less impact the noise will have on the correct arrangement of pixels. In conducting CT scans for 3D reconstruction, it is essential to know the appropriate parameters for actual application. There are four classes of segmentation processes to consider (Wiltgen, 1999):

(1) The segmentation procedure of sorting gray values according to their similarity.
(2) The point-oriented procedure of identifying objects by their gray values.
(3) The segmentation procedure of sorting gray values according to their abrupt change.
(4) The edge-orientated procedure of identifying objects by their edges.

The most important procedure is the segmentation procedure of identifying objects by their gray values (2). Here, the gray value is the decisive factor if a pixel belongs to an object or not. The gray value scale is used to define a threshold that makes it possible to divide an object with equal gray values from the background. The basis for that procedure is the

histogram of an image. Important procedures that apply this principle include (1) thresholding and (2) region growing.

The basis of thresholding (1) is the histogram and the value range of an image. It is supposed that the considered object is presented in a closed range of the complete gray value scale. The final separation of object and background is carried out by defining the threshold *T* (Wiltgen, 1999):

$$b'(x,y) = \begin{cases} b(x,y); b(x,y) \geq T \\ 0 \quad\quad ; b(x,y) < T \end{cases} \tag{II-4}$$

Hereby, pixels (b) can be related to an object if they are above *T* while pixels under *T* can be sorted to the background and not to the object. Important to note is that some parts of an image can be related to a segmented object although they do not belong to that specific object. This effect results when selected gray values lie within the same gray value distribution purely by accident. The best-suited method is the manual execution threshold and is considered the most accurate segmentation procedure (Bowers et al., 2009).

The segmentation procedure that compares the pixels of a region with a selected starting pixel or seeding point is that of region growing (2). The region-growing operation involves the definition of one or more seeding points (x_s, y_s) in an image according to their gray value b (x_s, y_s). The process starts by taking the seeding point's gray value and comparing it with the proceeding distance of every other pixel (*x, y*). The following term confirms the pixel's gray values:

$$|b(x,y) - b(x_s,y_s)| \leq T \tag{II-5}$$

The basic concept of region growing is that a selected seed point is used to connect consecutive neighboring voxels, with the provision that selected threshold (*T*) determined by the seeding points gray value is not exceeded. The threshold for the deviation of a gray value of the next-related pixel compared with the gray-value of the seed point (x_s, y_s) is defined by *T*. The approach aims to find merging criteria to obtain homogenous regions (Ayache et al., 1996). Figure 2-14 depicts different stages (1–4) of a region-growing algorithm. From a user-defined seed point (*x*), more and more voxels are aggregated that fulfill the inclusion criterion (Preim, & Bartz, 2007).

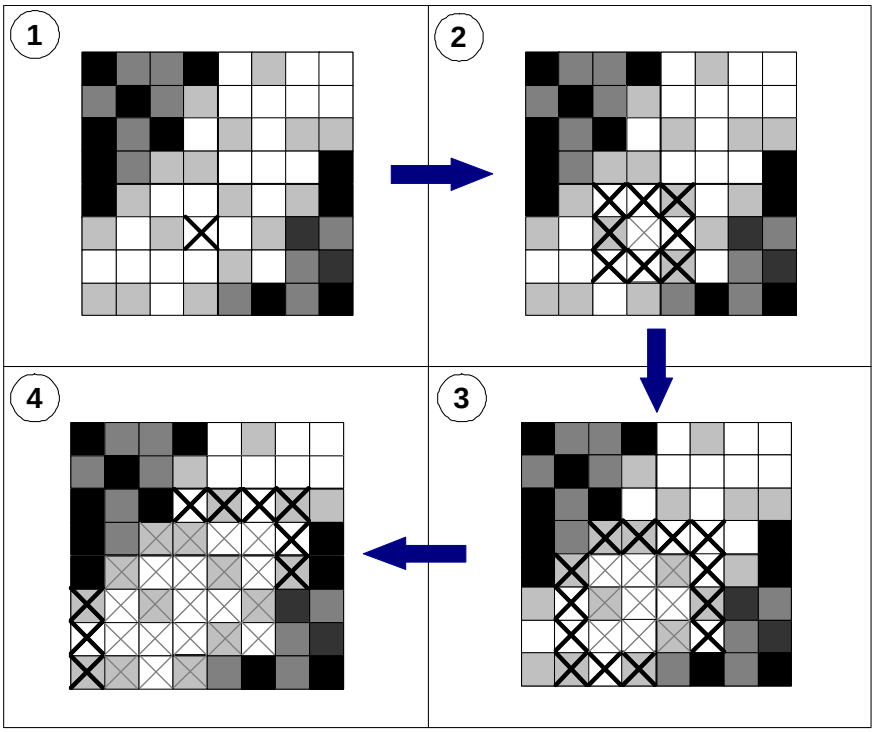

Figure 2-14: Region growing procedure (adapted from Preim & Bartz, 2007)

A current wave front (*X*) is defined by successively found voxels that fulfill the threshold criterion defined by the seed point. After the geometric forms in the scanned images are defined, the successively scanned 2D images are used to connect the forms in the third dimension.

2.1.4 3D Reconstruction of medical images

To carry out a 3D reconstruction process using data scanned by tomography, there are several 3D reconstruction parameters by which the complete modeling process is determined. These parameters are speed, data handling, and accuracy. After the acquisition of image data sets using appropriate acquisition parameters, image reconstruction follows to determine the final data set. The following parameters have to be set:

(1) Internal interpolation methods of scanner
(2) slice thickness
(3) slice increment.

In the use of spiral and multidetector scanning machines, a reconstruction failure occurs every 360° rotation. This effect depends on the con tinuous table feed that leads to artifacts. Failures are caused by the principal problem that the first and last projection along a

complete 360° rotation deliver different data, due to continuous table shift. Therefore, an internal interpolation method of the raw data is essential to attain a complete 360° data set of projections for the considered table position in one plane. One such algorithm that can run the interpolation is a linear method called 360° LI (Linear interpolation). The basic principle of this method is that the algorithm interpolates for every angle (equaling 360° in total) between the two projections, which are then located to the given z-position. Two 720° rotations are needed to run this interpolation with the result that the rotation failure is nearly eliminated. However, the slice profile increases in width as a result. Another algorithm used is the 180° LI method. Here, the fact that radiation absorption is nonanisotropic is used to virtually calculate a second spiral for interpolating the real sequence with the corresponding angles of both spirals (Prokop et al., 2006). The most frequently used reconstruction algorithm is the 180°LI interpolation method with a pitch of 1. This value prohibits an increase of slice thickness with respect to slice increment (Prokop et al., 2006).

The second 3D reconstruction parameter to consider is the slice thickness. Important to note is that in traditional CT the width of the slice profile is the same as the chosen slice increment. For the spiral CT scanner and multidetector CT machine an effective slice thickness is calculated because here, it depends on different factors such as table feed and interpolation algorithms (Prokop et al., 2006).

The third and main parameter that must be set is the slice increment or reconstruction increment. In general, the slice increment is defined as the space between the interpolated (internally calculated in CT machine) slices (Prokop et al., 2006). The choice of an appropriate slice increment is an important parameter due to the fact that there is no information available about the gray value distribution between slices (Fig. 2-15).

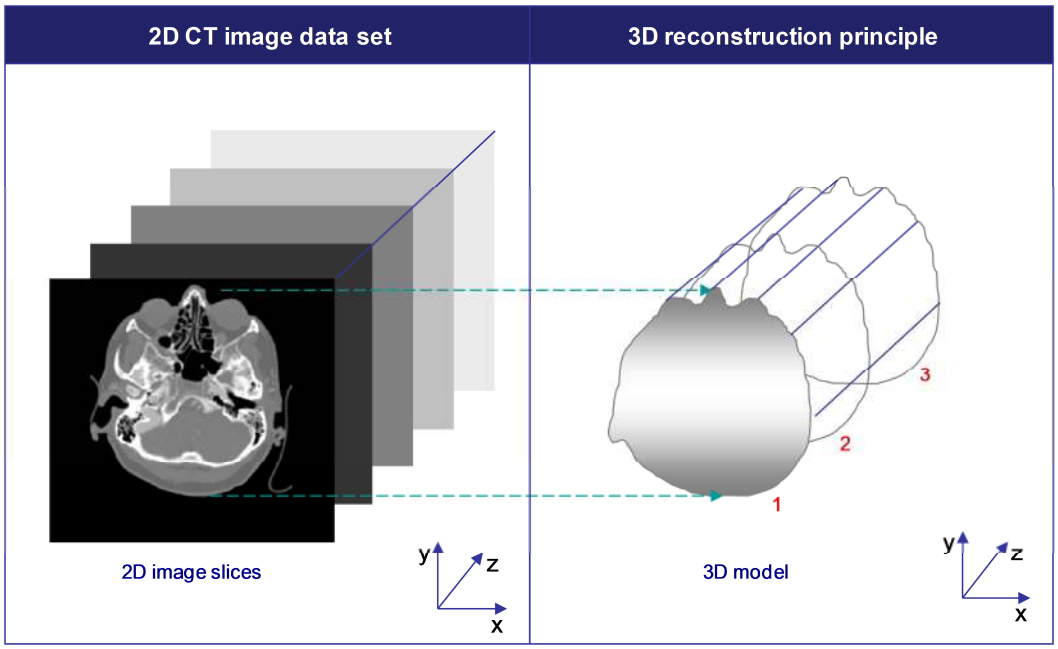

Figure 2-15: 3D reconstruction principle

There are three possibilities for selecting an optimal slice increment. The first method is to take the same value for slice thickness and slice increment as seen in Figure 2-16 to ensure that no gaps exist.

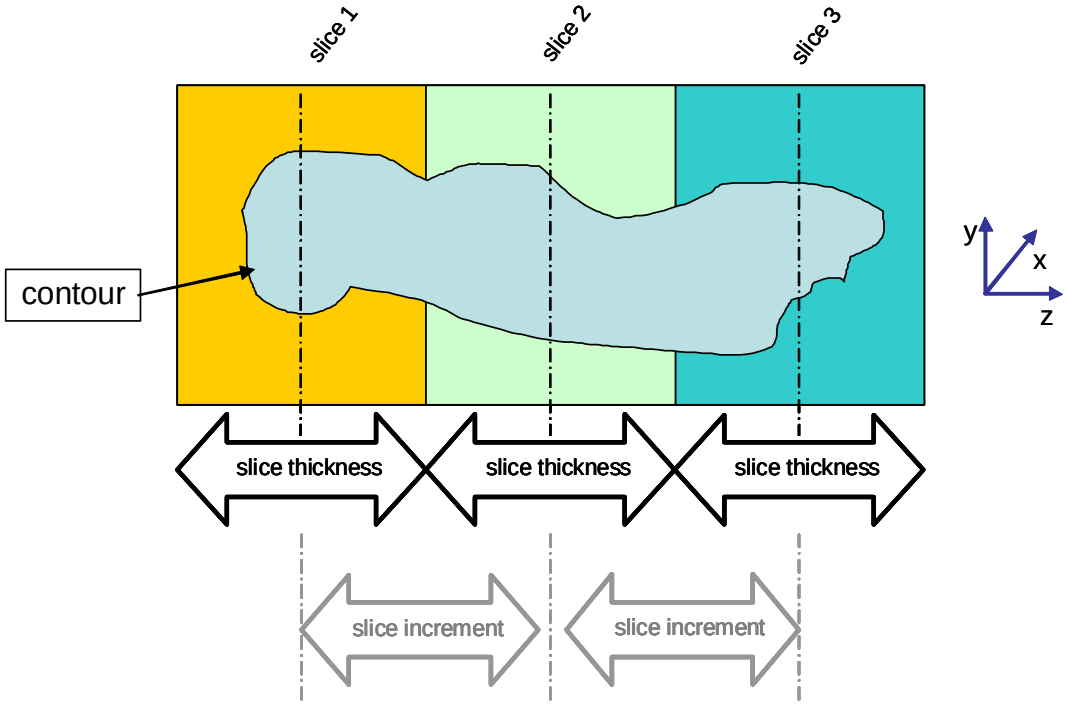

Figure 2-16: Coherence of slice thickness and slice increment

The second method applies if the original contours should be reconstructed in detail, and the slices should be overlapping to some degree. The result is that the original contours, which are represented by several slices, are positioned closer to each other (compare Fig. 2-16). The third method involves choosing a larger slice increment value as chosen for slice thickness, for purposes of making a rough scan.

2.1.4.1 Surface meshing

For a 2D dataset describing a landscape, the value at each point represents height. When connecting points of equal height, iso-lines are generated, which are commonly used in elevation maps. In 3D, the corresponding connected components are called iso-surfaces. These are commonly used when visualizing volumetric data generated by tomographic scans. In this case the values in the dataset represent the density at a certain point and can be used to locate parts of interest, such as bone structure.

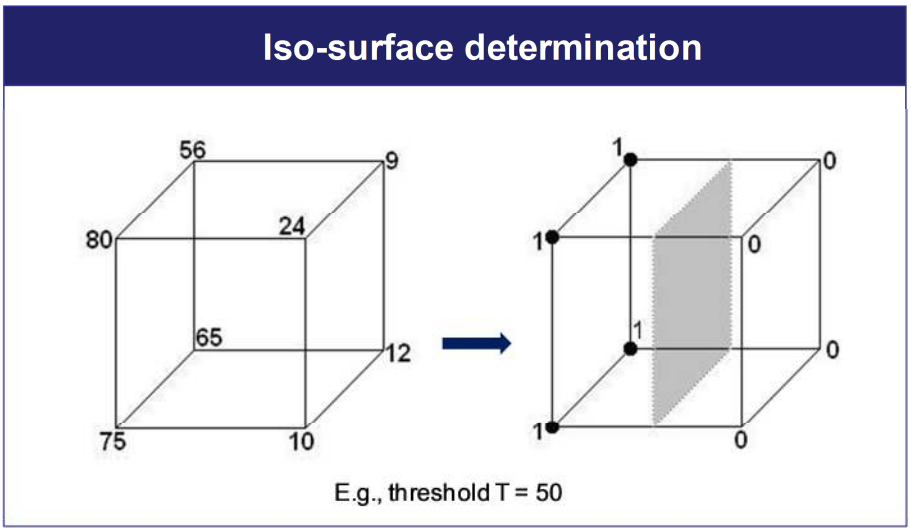

Figure 2-17: Iso-surface (adapted from Kirschner, 2006)

A very efficient method to construct the 3D surface was first described in 1987 by Lorensen and Cline (Lorensen & Cline, 1987). Their so-called marching cube (MC) algorithm creates a polygonal surface representation of a scalar field for a surface with a constant value (Fig. 2-17). In the case of CT, this represents a certain material density. MC has become the de facto standard algorithm for generating polygonal models of 3D implicit surfaces (Bennamoun, 2001). The algorithm uses a divide-and-conquer approach and works by determining how the iso-surface, the surface that represents a defined constant value from segmentation, intersects each cell. Given an iso-value *T*, each corner in a cell can be classified as being either above or below *T*. LI shows that the iso-surface must intersect any edge, which has one corner above, and the other corner below, *T* (or vice versa). Thus, there are 2^8 = 256 different ways in which the iso-surface can intersect the cell. Due to symmetry, these 256 cases are reduced to 14 as presented in Figure 2-18.

When the corners (e.g., x_1, x_2) have been classified, the threshold *T* (*X**) and the case has been found, the intersection point α along each edge is calculated using linear interpolation.

$$X^* = \alpha x_1 + (1 - \alpha) x_2 \qquad \text{(II-4)}$$

Then, normal vectors needed for shading the surface are calculated at each corner. For calculating normal vectors it is assumed that the direction of the gradient vector ($\vec{g}$) is normal to the surface. For calculating gradient vectors of a surface, the gradient vectors at the eight cube vertices are calculated first. Then, the gradient at the point of intersection (mesh vertex) is calculated via linear interpolation.

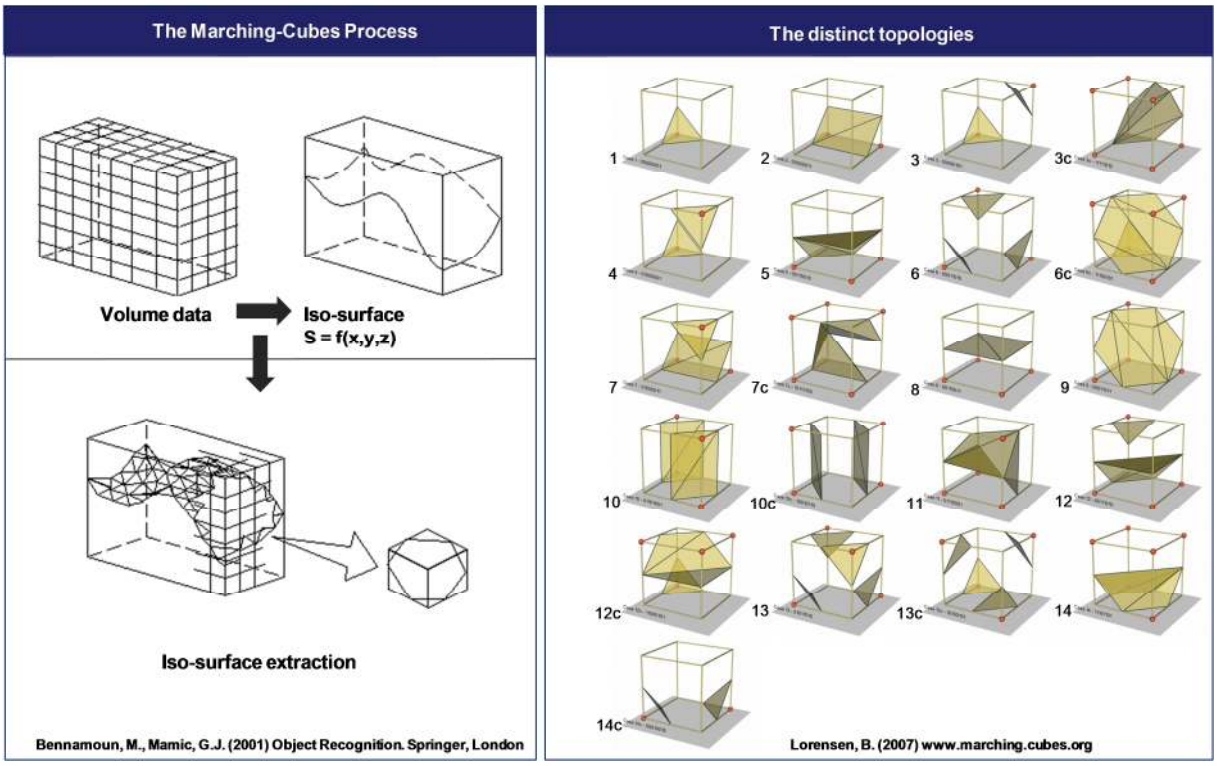

Figure 2-18: Marching cubes algorithm

Normalization generates the needed normal vector. In sequence, processing occurs as follows (Lorensen & Cline, 1987):

- Read four slices into memory
- Scan two slices and create a cube from four neighbors on one slice and four neighbors on the next slice (Fig. 2-19)

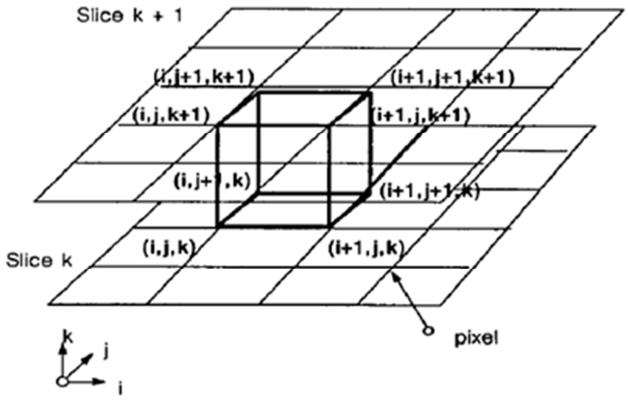

Figure 2-19: Marching cubes procedure (Lorensen, 1987)

- Calculate an index for the cube by comparing the eight density values at the cube vertices with the surface constant
- Using the index, look up the list of edges from a precalculated table (Fig. 2-18)
- Using the densities at each edge vertex, find the surface edge intersection via linear interpolation

- Calculate a unit normal at each cube vertex using central differences
- Interpolate the normal to each triangle vertex
- Output the triangle vertices and vertex normals

Often, the MC algorithm generates surfaces that are too rough-edged. The typical task in mesh editing is to smooth rough surfaces by removing the surface intersection points from the center to the corner of the cube. A disadvantage in using this reconstruction principle is the approximation by linear interpolation and the often seen large number of triangles (Schroeder et al., 1992). This problem persists in generating high-resolution scans and makes mesh editing and associated triangle reduction necessary. However, the results of reconstruction ultimately depend on the quality of the originally generated data.

2.1.4.2 3D Reconstruction failures

There are parameters that do not result in well-shaped geometric 3D models. The main problem for a valid 3D reconstruction is the edge resolution of structures represented by pixels along the z-axis, which is the length axis of a patient. The length of edges is determined by the chosen slice thickness and slice increment. When both parameters are selected as too high, the total length of edges is not scanned and the exact geometry cannot be reconstructed. The following effects are caused by an inaccurately chosen slice thickness, slice increment, and associated adjustments:

(1) Resolution → “staircase effect”
(2) Partial volume effect → blurred edges
(3) Noise → surfaces not well-shaped

If the interslice distance is too large, there is information lost about the real geometry in it. Figure 2-20 shows how a lack of image information is responsible for a roughly resolved surface.

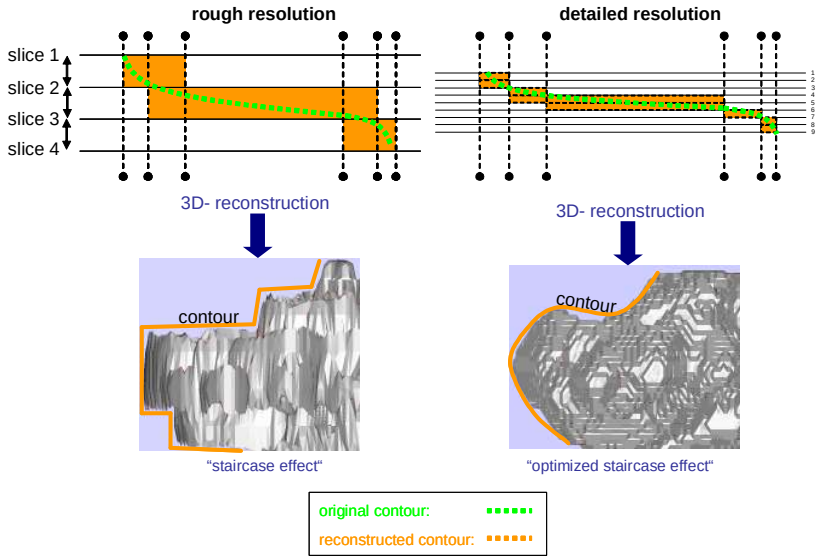

Figure 2-20: Surface resolution

As demonstrated in Figure 2-20, more detailed resolution can be interpolated much better (1) and results in a rounded anatomical contour. This may be compared with the use of a rough resolution, which leads to the typical "staircase effect". Here, the original contour in z-direction is approximately based on geometrical information given by the original slice contours. With greater distance between the original contour slices, there is a loss of data. Thus, the resulting resolution is as good as the slice increment that has been chosen. The partial volume effect (2) occurs due to the fact that the gray value of a voxel represents only an average value of the radiant absorption of material that is positioned within it (Klein & Broeckel, 2005). The results are blurred edges that are difficult to catch for segmentation.

Figure 2-21 shows the principle of a partial volume effect. The gray voxels (v_1 …, v_5) that should represent the blue tube are calculated by the average tone of the amount of gray-value given by the tube. Two voxels are shown to describe this effect. The first one (v_2) has less additional information about the tube (less blue) than the second one (v_3).

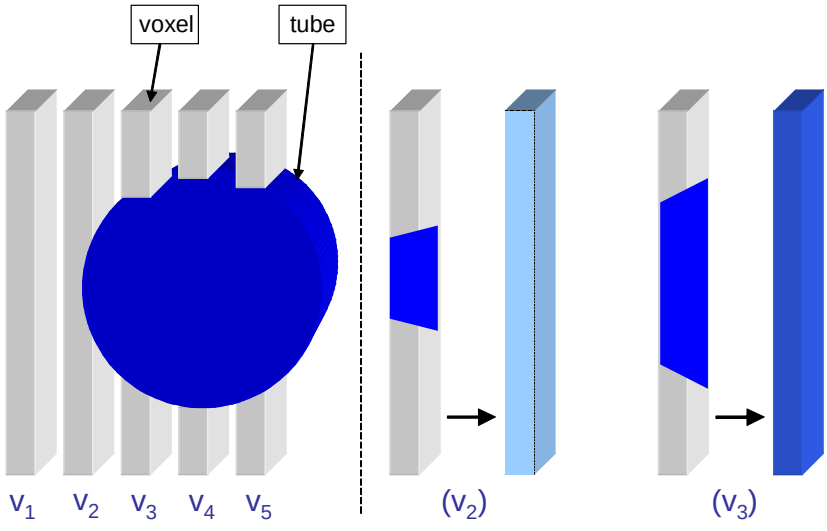

Figure 2-21: Partial volume effect (adapted from Rogalla, 2006)

The result is that voxel v_3 has a darker gray value than voxel v_2. Nevertheless, in both cases the exact geometry or contour is blurred and the tube is not caught accurately with that size of a voxel.

Another effect occurring during the 3D reconstruction process involves the noise of an image (Chapter 2.1.3). Noise is a parameter that is determined by the dose of radiation of detectors in the CT. A typical case of high noise occurs when level of radiation is small with respect to slice thickness. To remedy this, a reconstruction filter (kernel) in the CT can be used for smoothing. However, smoothing is limited due to decreasing regional resolution inherent in the smoothing process. Figure 2-22 represents the principles of, and effects caused by, high noise.

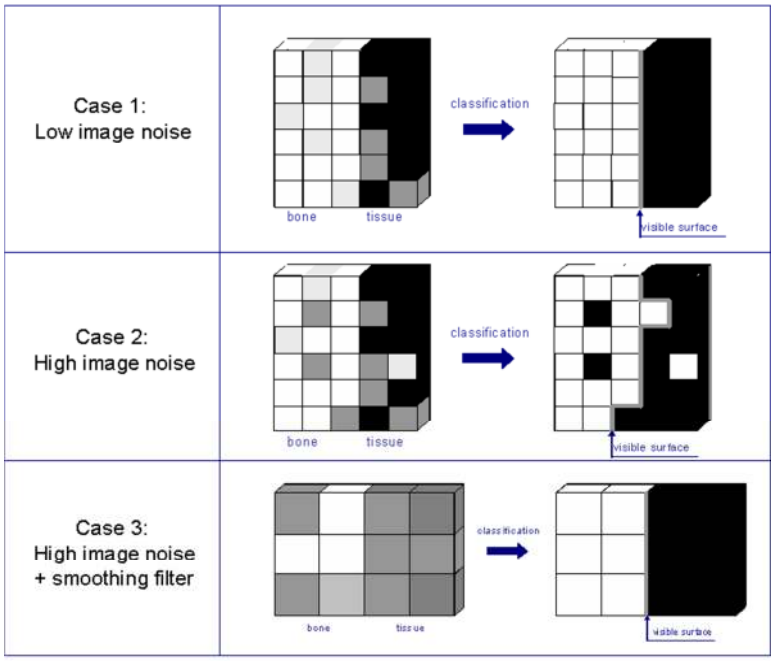

Figure 2-22: Noise effect (adapted from Rogalla, 2006)

In case 1, low noise and a good resolution adjustment are shown. The tissues are well separated and the surface is smooth. Half of the given slice thickness increases the image noise by a factor of approximately √2 (Rogalla, 2006). That result can be seen in case 2 where pixels have randomly chosen density values. They will be positioned by the classification principle to the next related region. The resulting effect is that the surface looks rough. Moreover, there are isles of false selected pixels within the already separated regions. In case 3, a smoothing filter is used additionally for noise reduction.

The present thesis employs the Taubin filter for smoothing in order to withstand typical problems of shrinkage due to applying the frequently used Laplacian filter for smoothing. Laplacian smoothing changes the position of the vertices, but does not add or remove any vertices. One limitation of this type of smoothing lies in the fact that the triangles slide across

the mesh (Bray, 2004). This movement pushes the mesh towards more regular triangulation. The effect of that sliding leads to a distortion of the shape of the mesh. For applications in which accuracy plays a role, shape distortions should be avoided. Taubin smoothing relies on the use of two filtering steps, one inwards and one outwards, to approximately preserve the volume of the mesh (Bray, 2004). Nevertheless, inaccuracy cannot be avoided completely.

2.1.5 File format

The exchange of generated medical image data is only possible if data are defined according to a general standard. Without this, it would be difficult to run related processes that use medical image data. A standard format was passed in 1983, defined as ACR-NEMA standard (DICOM Homepage, medical.nema.org/ 2008). The following design objectives of the ACR-NEMA standard have been formulated:

- The transfer of image data that are not manufacturer-related
- The design of an image archive that can be used by different departments
- The creation of a database for diagnostic information that can be accessed globally

Most of these objectives had still not been realized before the introduction of the .DICOM format, a successor of the ACR-NEMA standard. Since the introduction of the .DICOM format, it is possible to make data transfers from scanners to a network (that supports data transfer) and then to external data mediums such as CD-ROM or USB-stick (Sonek, 2004).
A .DICOM file is a data stream that consists of single data elements (Raphan, 2004). A .DICOM file contains first the appropriate gray value information that comprise the images taken (e.g., JPEG-format). Secondly, a .DICOM file includes a header with important information about scan parameters including patient data, date, slice thickness, slice increment, resolution, image size, etc. A description of scan information based on specific attributes, which can be sorted, is shown in Figure 2-23.

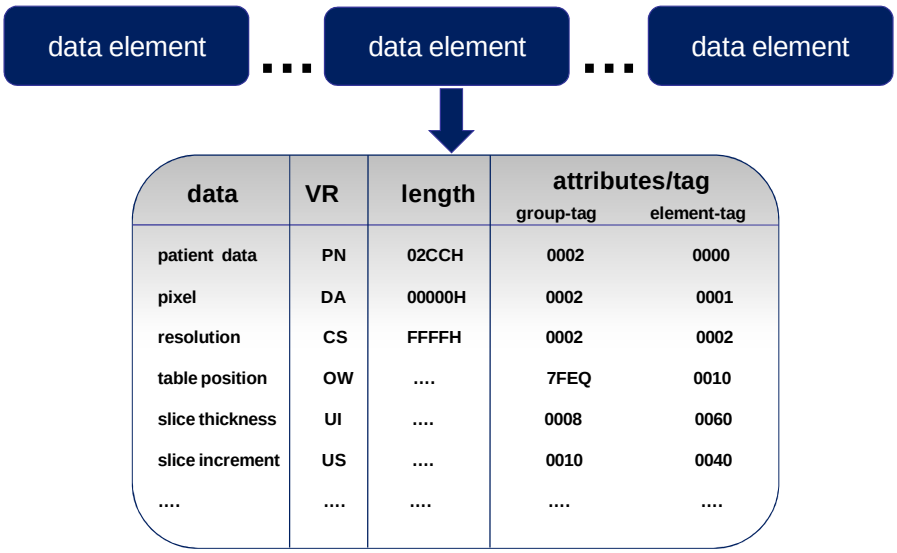

Figure 2-23: Example of a DICOM file header

The exact identification of an attribute is made possible by taking the appropriate tag, consisting of two 16-bit numbers. The first number, the group tag, indicates the relation to a specific group, and the second number, the element tag, identifies the element of the determined group. Together these numbers represent the format and type of data, for which values are shown in the column's value representation (Fig. 2-23). Additionally, a data element contains information about its length and can be either 16-bit or 32-bit. With the exact carrier identification information it is possible to create an object-coordination system using image coordinates of the pixels and the table position (Reinhart, 2002). By using the data information in combination with gray values of the image slices, it is possible to carry out a reconstruction process such that a 3D model is created. To date, an appropriate software tool that is able to conquer large .DICOM files for use in 3D reconstruction, is sought.

2.1.6 Software processing

A decisive point in the 3D reconstruction process is the use of a software tool capable of reconstructing accurate data models as well as suitable for subsequent engineering processes like RP. The worldwide commercial software leader in RP modeling technology, providing the most detailed and precise virtual 3D models available from medical data, is Materialise N.V. (Leuven, Belgium) interactive medical image control system (Mimics) (Gibson, 2005). Mimics can be used for visualization, segmentation, and 3D rendering of CT or MRI image sets. With Mimics, it is possible to display image data in all essential views: the original axial view of the image, the coronal and sagittal view using re-sliced data, and the calculated 3D view (Fig. 2-24).

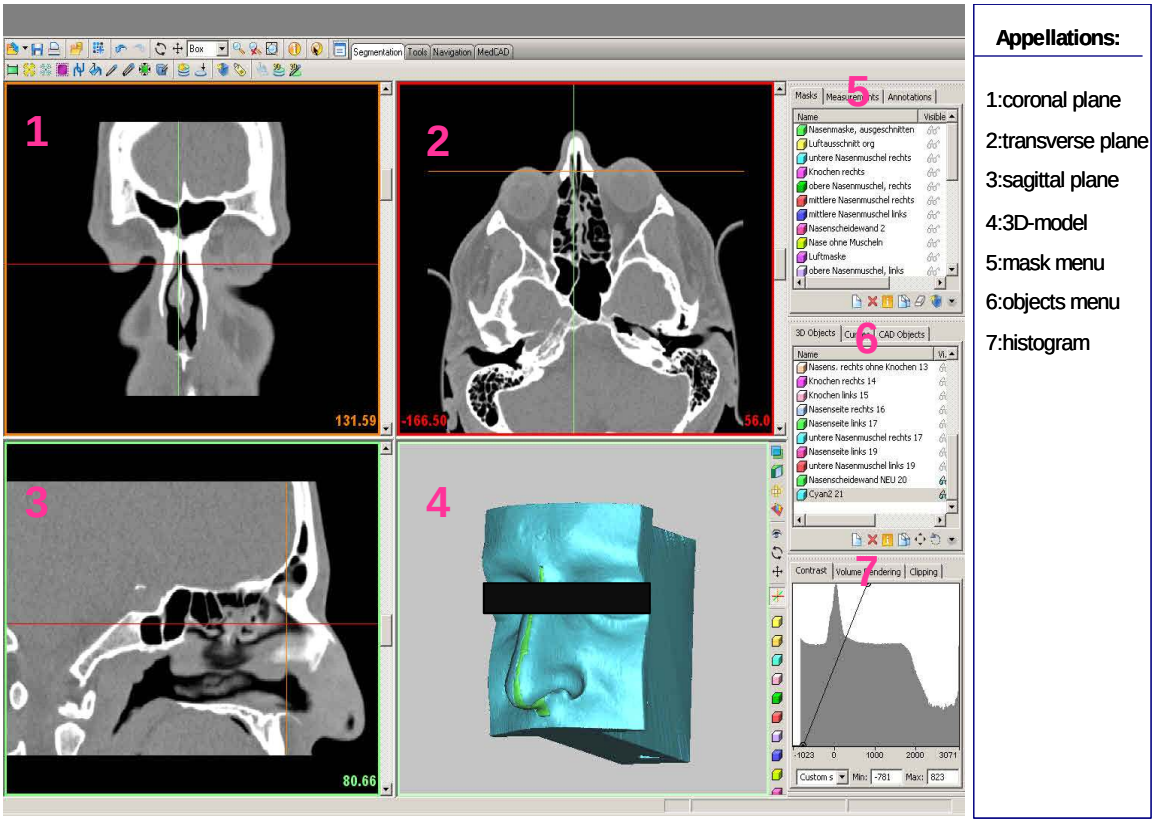

Figure 2-24: Mimics layout

The main operations performed by Mimics (Version 13) software for 3D reconstruction are:

(1) Thresholding
(2) Region growing
(3) Editing
(4) Dynamic region growing
(5) Morphology operations
(6) Boolean operations
(7) Cavity fill
(8) Import/export modules

The first operation carried out by Mimics to set up a segmentation mask is the thresholding function (1). A region of interest is defined by selecting a specific range of gray values, whereby the selected region's boundaries represent the upper and lower threshold values. Mimics software then allows the setup of masks in which all pixels from a selected range of gray values are highlighted. The region growing operation (2) is a segmentation tool used for the elimination of noise and the separation of structures and objects that are unrelated. Frequently used, an important function for drawing and erasing operations is the editing tool (3), which functions by setting local thresholds. The drawing and erasing function is typically

used for larger separation procedures such as those required in complex bone and tissue structures that cannot be segmented alone using the main thresholding function. The dynamic region growing tool (4) allows the specific segmentation of an object on the basis of the connectivity of gray values in a predetermined range of gray values. Another tool that is used for segmentation is the morphology function (5). This function is used for removing and adding pixels from the source mask for the purposes of copying into a target mask. Mimics offers the possibility of performing Boolean operations, which are essential (6). That is, different combinations of two specific segmentation masks are made possible with a subtraction, union, or intersection operation. These operations are typically used for the separation of joints. The function of cavity filling (7) is used for filling internal gaps of a segmented mask for the purpose of copying results to a new and optimized mask.

If objects under consideration are segmented systematically by setting up different segmentation masks, 3D models can be calculated using the MC surface meshing algorithm. Then, a 3D calculation may be run whereby parameters for resolution and filtering must be set. Related object information such as height, width, surface, volume, etc. may be added. Following 3D calculation, Mimics displays a 3D model using the advanced rendering option of OpenGL, which is a hardware acceleration function enabling high-quality renderings for the optimal display of 3D objects. Added to its basic functionality of object segmentation for conversion into 3D models, Mimics offers additional modules: the import module (8) and STL+ module (8) are relevant to this thesis.

The import module (8) allows importing 2D stacked uncompressed medical images from CT in a variety of formats such as the frequently used .DICOM file format. In this module it is possible to specify the appropriate slices that comprise the considered object. The STL+ module (8) is an interface that allows exporting generated 3D models as triangulated files (.STL or .VRML) (see Chapter 2.3) to subsequent applications. Overall, it is possible to export .STL files from a mask or a calculated 3D object. Two important options for reducing file size for easier handling in further data processing are triangle reduction and matrix reduction. By adjusting the matrix, the grouping of voxels to calculate triangles can be determined to reduce resolution. The function of triangle reduction allows the number of triangles to be reduced in the mesh. Accordingly, file size decreases and later manipulation of the file is facilitated. An additional function of the STL+ module is smoothing, which makes rough surfaces smoother. Mimics permit mesh editing by setting different parameters for triangle reduction and smoothing. The parameters relevant for the present thesis are depicted in Table 2-1.

Table 2-1: Mesh editing parameters

Parameter	Function
Triangle Reduction:	
Tolerance	Maximum deviation of triangles that build an aggregation of triangles, which deviate in relation to the set value for tolerance.
Edge Angle	Defines the maximum angle that triangles enclose in one plane before they will be linked to a different plane. Triangles with an angle smaller as the set edge angle will be modified.
Iterations	Defines the number of runs for reducing the data.
Mode	Defines the methodology of triangle reduction.
Smoothing:	
Iterations	Defines the number of runs for smoothing the surface.
Factor	Application of this factor controls weight (Taubin filter)

The use of tolerance enables the user to define deviation between the original contour and approximated contour (see Chapter 2.2.3). Setting the edge angle allows the angle of the normal vectors occurring in one plane to be determined. Mimics contains three different mesh simplification algorithms (modes): point, edge, or advanced edge. The differences between these algorithms are “where” in the object that is used, for simplifying the mesh. The mode point deletes the vertices in the mesh. The mode edge eliminates the edges first to reduce the number of triangles. Advanced edge is based on the edge mode and reduces triangles additionally (further details classified confidential by Materialise N.V. Leuven).

2.2 Rapid prototyping

Supporting and systematic tools are characteristic of the product development process. RP or as announced recently additive manufacturing (AM) (Gibson et al., 2010) is an important tool for reducing time and costs in such processes. Today, alternative ways are sought worldwide to develop higher quality products, faster, within traditional engineering fields as well as in related fields such as biomedical engineering. RP allows fast and automated fabrication of physical objects directly from virtual 3D CAD data without significant process planning related to part features and geometry (Gibson, 2005). Originally set up to increase the speed of prototype manufacturing in the manufacturing industry, RP can also be used for different applications, such as in medicine (Beneke et al., 2003).

The basic premise of RP divides a 3D manufacturing problem into several single manufacturing steps to reduce complexity (Lorenzen & Breitinger, 1997).

RP is widely known and based on various manufacturing principles: On one hand, there are the so-called additive RP processes of stereolithography (SLA), selective laser sintering

(SLS), fused deposition modeling (FDM), and 3D printing (3DP) for example. These additive RP processes are based on the principle of adding material in layers as required, without shaping machine tools in order to merge layers three-dimensionally (1-step procedure). On the other hand, there are the subtractive procedures of milling and turning that use cutting edges to generate a model. Their combination is the quasi-additive processing such as layer laminate manufacturing (LLM) and CNC based milling and joining (Bergers & Mallepree, 2010) that may be classified with additive RP procedures according to three process steps: contouring, joining, and finishing (3-step procedure) (Fig. 2-25).

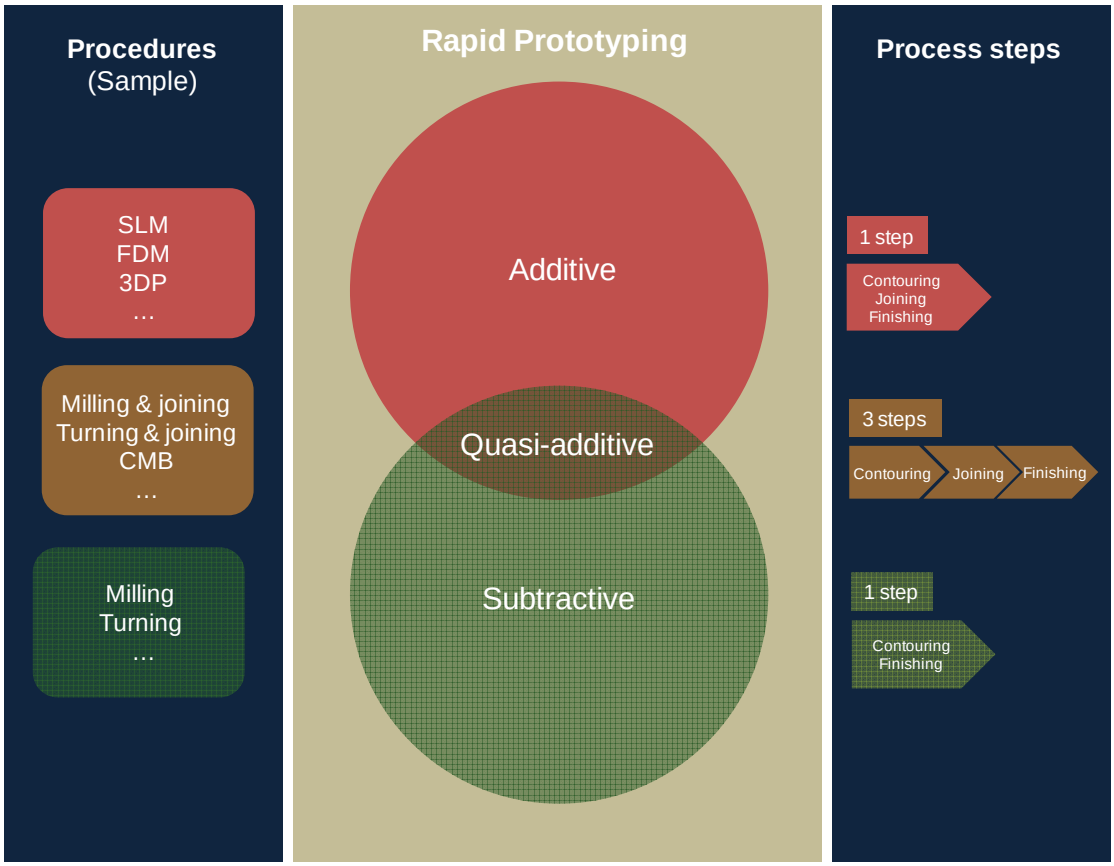

Figure 2-25: Classification of selected RP procedures (Bergers & Mallepree, 2010)

All RP procedures are based on a high level of automation to expediate manufacturing of models without time-consuming process interventions. From this perspective, RP procedures with more than one process step such as LLM or milling and joining have no deviating basis principle. These procedures are thus quasi-additive (Assmann, 2003). The requirements for a high accurate, fast, and economic manufacturing process can be fulfilled.

2.2.1 Classification of models and prototypes

Novel product ideas may be realized using RP, with physical models and prototypes. To date, a standardized designation for model and prototype is not defined. The German

industrial designer union (Verband Deutscher Industrie Designer e.V.; VDID) has differentiated models according to six different types: specimen, prototype, design model, ergonomic model, functional model, proportional model. In contrast, the German NC Gesellschaft e.V. (NCG) has organized the different models according to four different classes on the basis that the different models do not differ from each other to a significant degree (concept model, geometry prototype, functional prototype, technical prototype). In general, Gebhardt (2007) recommends orientation on the classification from VDID. Both classifications are designed with respect to industrial applications and are still under development. To date, such classifications do not comprise medical applications because of the difference in model generation and designated use. Therefore, the present thesis aims to find a model classification for medical applications (Chapter 4).

2.2.2 CNC Milling as a quasi-additive RP procedure

Chip removal processes belong to procedures that offer highest accuracy in shape and grade. Milling offers a wide range of machining scenarios from rough contouring to final finishing. Based on the German standard DIN 8580, the manufacturing methods are classified in six main groups, which are split up into sub-groups (Fig. 2-27).

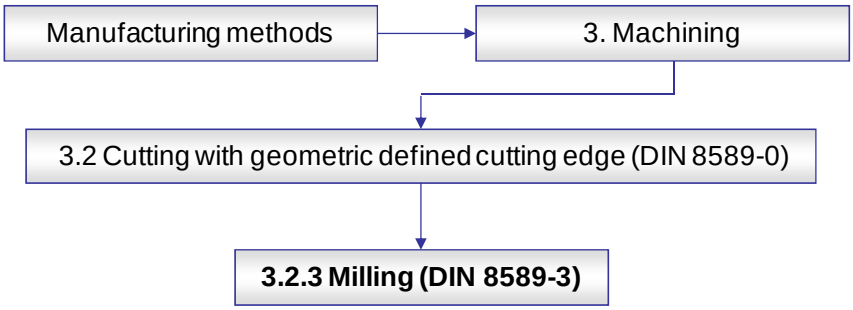

Figure 2-27: Manufacturing methods (adapted from DIN 8580, 2003)

The process of milling belongs to manufacturing methods within the main group “machining”. Machining is divided in sub-groups that are numbered accordingly. Milling is a sub-group of the group 3.2 “cutting with geometric defined cutting edge”. With respect to cutting the international standard is ISO 3002 (part 1-5). The terms for machining are defined internationally in the standard ISO 10791 (part 1-10). But, machining is not a singular process; these additional processes however, are not in focus of the present thesis.

In milling, a rotating tool with multiple cutting edges is moved slowly relative to a material to generate a plane or straight surface. The direction of feed motion is perpendicular to the tool's axis of rotation. The speed motion is provided by the rotating milling cutter. Therefore,

milling offers a wide range of application. The following paragraphs describe the main milling parameters that have to be considered if the aim is to generate a specific surface.

The three-step procedure of quasi-additive milling employs knowledge existing in the field of subtractive or machine manufacturing procedures, respectively. The decisive advantages in using CNC milling include the possibility to mill every material that is suited for machining, to mill models of high accuracy, to mill models in nearly every size (restricted only by available machine space), and to manufacture transparent models (Chapter 2.2.5). Compared with the RP procedure of SLS, the quality of surfaces is better within a decimal range. The accuracy of the geometry of an SLS-produced model can vary up to 0.6 mm (Assmann, 2003).

Due to this reason, CNC milling is considered an ideal process technology for manufacturing models for medical applications in which accuracy, transparency, and material issues all play major roles. Possible disadvantages may result in cases of complex geometries as source data. The basic challenge is to overcome the occurrence of undercuts (Fig. 2-28).

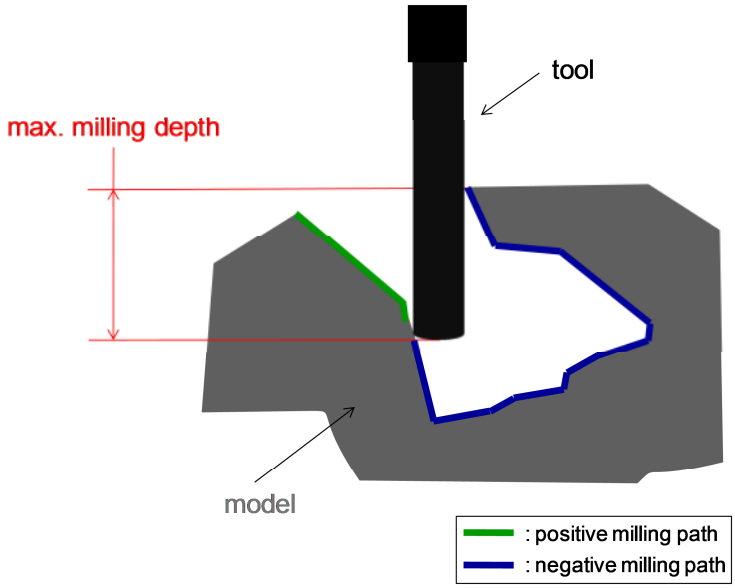

Figure 2-28: Undercuts in the case of complex geometries (3 axis machining)

As shown in Figure 2-28 in case of 3 axis machining it is impossible to mill a complete contour in a one-step process. There is only one contour that can be reached by the tool for operation (positive milling path, green line). The rest of the contour (negative milling path, blue line) is impossible to mill in the condition shown.

To overcome the problem of undercuts, a process of slicing the model at exactly the point that defines the maximum milling depth is suggested (Fig. 2-29).

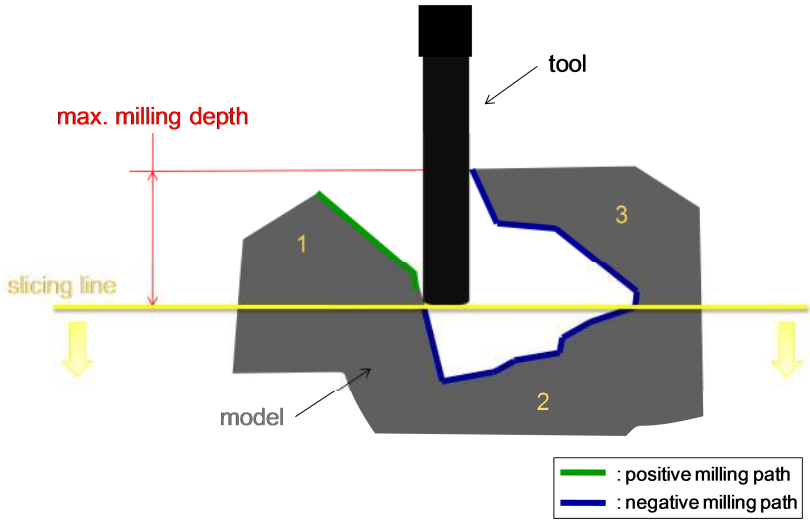

Figure 2-29: Slicing line

After the slicing is complete it is possible to mill the parts 2-3 (Fig. 2-30) in a single processing step. The consequence of slicing a model is that an appropriate joining principle has to be selected for completing the model (Fig. 2-30).

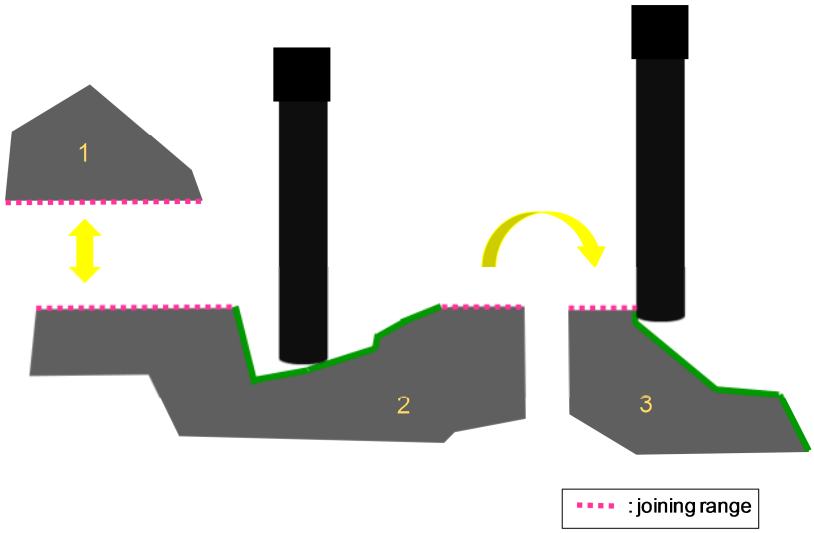

Figure 2-30: Sliced of milling components

As Figure 2-30 shows, there is a specific joining range along the slicing line for which an appropriate joining principle has to be selected.

If no undercuts are found on a model (e.g., cube), slicing and joining of layers are unnecessary. The principles of quasi-additive RP technology enforce a specific formulation procedure for the manufacture of a RP model based on 3D CAD data. The sequence of the quasi-additive RP process is shown in Figure 2-31:

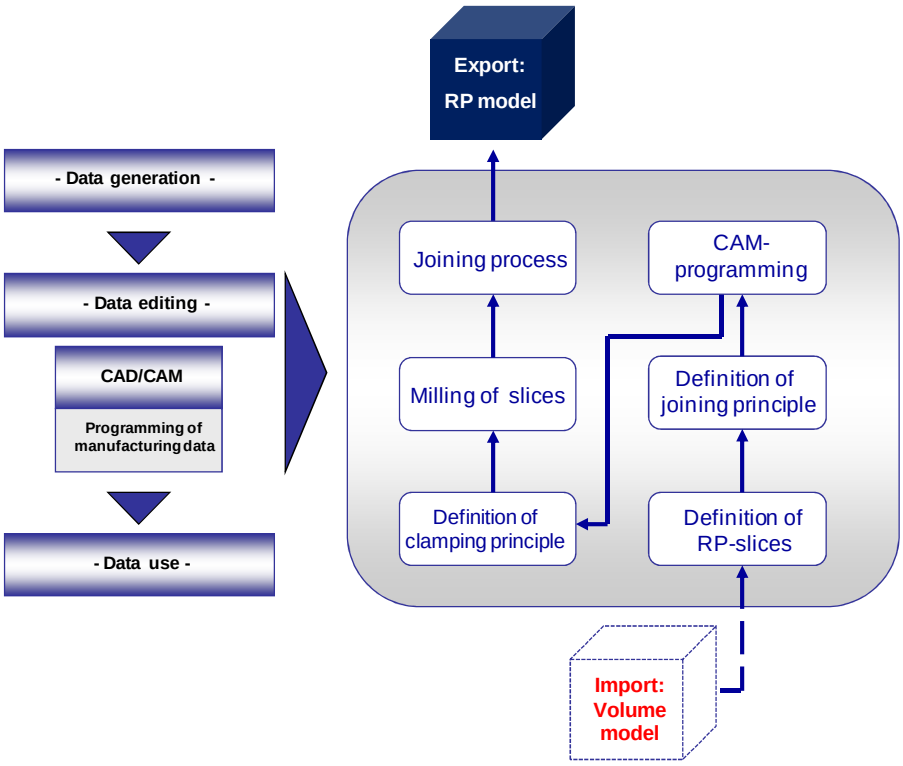

Figure 2-31: Quasi-additive RP process

Figure 2-31 shows that the quasi-additive RP process is differentiated into several processing steps. The process starts with importing an appropriate volume model, i.e., the generation of a 3D CAD model in a 3D CAD system (e.g., SolidWorks, Dassault Systèmes). The second step is the definition of slices to mill, which are oriented on maximal milling depth (Fig. 2-29) if undercuts are found. The next task is to determine the appropriate joining principle needed for the given case (e.g., communicational model, functional model). Then, each slice can be transferred into the CAM programming system to program the machine code for CNC milling. During CAM programming, an appropriate clamping principle has to be decided upon. Once the definition of clamping allows a sufficient repeat accuracy for exact joining, slices can then be milled. Afterwards, milled slices can be joined to complete a RP model.

A decisive factor in conducting the quasi-additive RP process is the selection of an appropriate slicing strategy that encompasses the succeeding process steps of clamping, milling, and joining. The challenge is to orient the procurement strategy precisely towards the case of use. The right strategy has to balance the decisive factors of accuracy, time, and costs.

An exemplary joining procedure is one with inner supporting geometries (Assmann, 2003). Here, required supporting elements are set as positive and negative. The idea behind the supporting elements, which are designed as tenon dowel joint, is that they serve on the one hand as needed joining elements and on the other hand as needed clamping element in the CNC milling machine. The first step in the manufacturing process is to manufacture the

supporting geometry in order to realize a clamping possibility. This is done for both side surfaces of the raw material used. For a part with positive-formed geometry, it is possible to use a standard clamping procedure because positive-formed supporting geometry gives a force application point for standard clamping elements. For clamping a part with the negative-formed supporting geometry, an appropriate sacrificial block is needed that contains the exact counterpart suitable for adaptation. The sacrificial block is only a temporal supporting clamp element that will be adapted to the supporting geometry. After manufacturing both parts, it is possible to join them using their respective supporting geometries. This guarantees that both parts will be joined very precisely (Assmann, 2003). Note, the tenon dowel joint can be designed additionally for more than two parts depending on the case in point, how many slices have to be made, and how many connections have to be set. Moreover, whether or not a model should be joined reversibly or irreversibly must be planned. Reversible connections often comprise the objective during product development processes when there is a need to vary several segments of a model. By designing models that are joined reversibly, the varied segments can easily be pasted into the existing model without the need to manufacture the complete model again. If a model needs to be manufactured for functional use, a solid connection must be defined where it is not a priority to provide a reversible connection. A lasting connection can be achieved by designing the tenon dowel joint as a friction-locked and positive-locking press-fitted assembly (Assmann, 2003). This assembly principle is realized by an interference fit that causes specific pressure forces. These forces are caused by the assembly procedure of both parts (parts A and B) whereby the geometries are damaged. Such pressure forces lead to a friction-locked connection in relation to a friction coefficient and friction surface. An additional joining possibility is to use a self-centering joining method such as serration. Standke (2008) suggests that serration makes reversible joining possible, even for functional prototypes.

Milling strategies

The surface finish is influenced mainly by the milling paths used. A previous study by Hastrich (2006) demonstrated that tool paths are always visible after machining even with the use of optimized parameters. Especially, stops of the tool are the cause of surface marks and appear in cases where tool path changes are needed or the tool dips into the work piece to start milling. Therefore, it is essential to reconcile tool paths with given geometry to avoid unnecessary stops that lower surface quality.

There are variety of options and parameters available for programming an appropriate CNC code to realize an accurate piece of work with high surface quality. For example, there are several possibilities as to how a tool can approach the surface (e.g., helical, tangential, curved). For an appropriate definition of tool approach, it is often necessary to define an

angle or radius in combination with the type of movement. With regard to milling the surface, there are several operational strategies possible (Fig. 2-32).

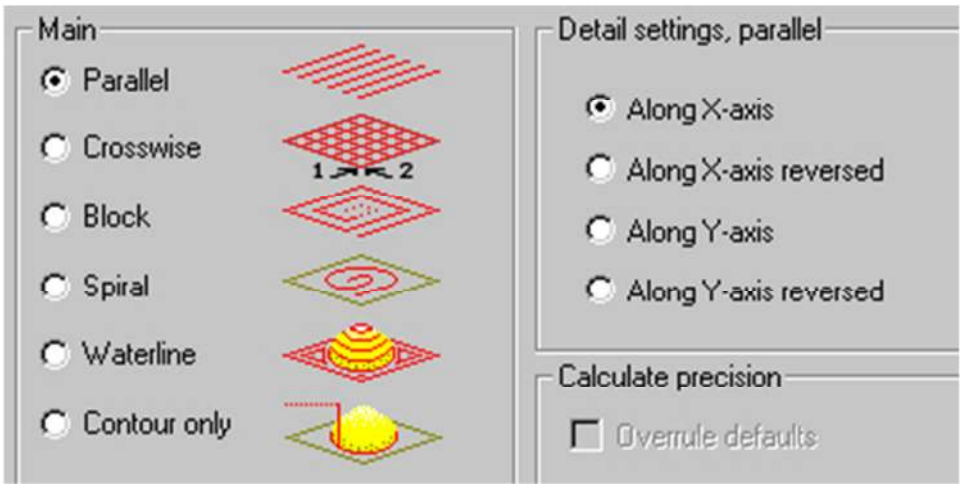

Figure 2-32: Milling strategies (Deskproto, 2010)

In summary, the most important milling strategies are as follows:

(1) Parallel, parallel in x- and y-direction, zig

a. Milling cutter operates in xy-plane, moves back in fast motion and operates again in xy-plane in offset of one increment; also possible (2)

(2) zig zag, meander, plane

a. Milling cutter operates in xy-plane and moves back parallel in xy-plane in offset of one increment

(3) Intersected

a. Combination of (1) and (2)

(4) Inside/outside, pocket inside/outside

a. Milling cutter operates from centre of geometry in a rectangular spiral from inside to outside or from outside to inside

(5) Helical, helical from inside to outside

a. Milling cutter operates from centre of geometry circular from inside to outside or from outside to inside

(6) Cut

a. Combination of (1) and (2)

(7) Z-constant, Z-plane, contours

a. Tool paths with constant Z-level (cutting depth, increment) along the contour of geometry

Cutting parameters

The cutting parameters determine how fast and how deep the milling cutter goes in a work piece, and how much material will be removed. The following cutting parameters influence surface finish the most:

- Revolutions per minute, rpm
- Feed rate, v_f
- Cutting rate, v_c
- Feed, f, f_z
- Infeed (Z-direction)
- Axial cutting depth, a_p
- Radial cutting depth, a_e
- Lateral off-set

The revolutions per minute are defined as [rpm], and describe the revolutions of the main control rod per minute. The feed rate (v_f) determines how deep the milling cutter goes in the work piece and is defined by [m/min]. The cutting rate (v_c) is related to the tool diameter and rpm and is defined by [m/min]. The cutting rate specifies the speed of the perimeter cutters in rotational direction (Böge, 1995). The feed (f) describes the rectilinear forward motion of milling cutters during operation (Knaur, 1988) with units defined as [mm/rpm]. If there are multiblade milling cutters in use, the feed will be described as feed per tooth (f_z) in [mm]. The difference of the level of the tool paths is specified by the infeed or z-infeed in [mm]. The axial cutting depth (a_p) and radial cutting depth (a_e), determine the axial and radial dimensions of the tool cutters, respectively (Böge, 1995). The cutting depth [mm] specifies how much material the milling cutter can remove in one sequence. Running a milling operation, the milling cutter racks out various tool paths. The lateral off-set describes how far tool paths have shifted relative to each other. This shifting has a wide influence on the geometric accuracy. Especially, precision of curvatures and free-formed surfaces is determined by lateral off-set. When lateral off-set is high, the appearance of staircase effects cannot be avoided.

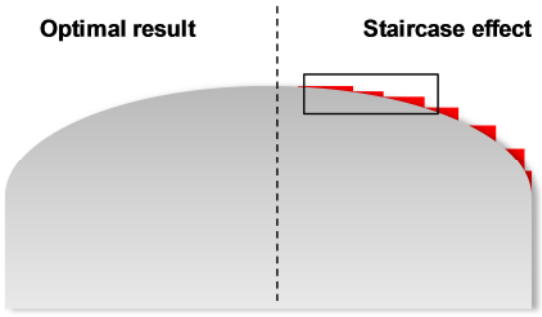

Figure 2-33: Staircase effect related to lateral off-set

Staircase effects shown in Figure 2-33 (red) will be generated if lateral off-set is chosen too high. In this case, curvature is square-cut in contrast to an optimal result, which can be achieved using an appropriate lateral off-set adjustment (e.g., under 1 mm).

The main effect of cutting speed on surface quality is in determining whether a chip is cut out or torn out. Cutting speed (v_c) is defined by the product of rpm (n), pi (π), and tool diameter (D) (Conrad, 2006).

$$V_c = D * \pi * n \tag{II-5}$$

An additional important influence on cutting material is the feed rate (v_f), which is defined by the product of feed (f) and rpm (n) (Conrad, 2006).

$$v_f = f * n \tag{II-6}$$

In general, when running a milling operation, two process steps are carried out. First, a rough contour is milled using a tool for roughing large chip volumes. The exact geometry is usually generated by smaller milling cutters in order to countersink small contours and tight pockets. By conducting such finishing procedures, smaller feeds and smaller lateral off-sets are typically selected to generate accurate models of high surface quality. If large parts or models with complex geometrical morphologies need to be manufactured, a rough finishing process can be added following standard roughing to reduce processing time. In this way, the removal of as much material as possible will be achieved before finishing starts, and where less chip volume can be subsequently removed. As already mentioned, cutting parameters can have a deep impact on accuracy and surface quality by controlling the action that takes place between tool and work piece. Thermal influences during cutting comprise another factor. Especially, in milling plastics, heat plays a role in cases where excellent surface finishes are needed. It is well known that plastics (e.g., thermoplastics) are limited heat conductors. The resulting heat is normally 75 % absorbed within the chip. Typically, 18 % is absorbed by the tool and 7 % by the work piece (Spur and Stöferle, 1979).

It is important to guide the heated chip away because it has the ability to heat up the work piece two-fold times more than the original cut (Spur and Stöferle, 1979). . Therefore, one should aim to generate many small chips to lead the heat away as quickly as possible, which is frequently supported by cooling lubricants.

2.2.3 File formats

Triangulated meshes are the de-facto standard in RE applications, largely due to their simplicity and to the possibility of file size reduction. The dominant file format in RP is the well-established .STL format, although it is not a standard. There are additional data formats used in RP applications such as .IGES (Initial Graphics Exchange Specification) or .STEP (Standard for the Exchange of Product model data), but these are not as widely established as the .STL format. The developments of CAD and CAM systems have lead to an integration of CAM modules in CAD systems. By that integration it is possible to generate machine codes in one system (CAD/CAM) by using the same data basis. With that enhancement it is possible to combine CAD and CNC code programming to operate one system in one process sequence.

STL

As mentioned, the .STL format is the dominating data format in RP data processes. The advantage .STL offers is that it allows independent usage by manufacturers, suppliers, and in particular, software developers (Gebhardt, 2007). However, the .STL format is an approximate representation of a true solid-surface model, and a huge amount of .STL data is needed to provide sufficient accuracy for RP. The basis of an .STL data set is the description of model surfaces by triangulation. .STL files are surface approximations of models generated by CAD or RE data processes (e.g., 3D reconstruction with medical images). The .STL format is a tessellation representation, which defines a 3D object by a series of triangular facets. Each triangular facet is defined by three vertices and a unit normal vector for the facet where the normal vector direction indicates the outside of the object (Lin, 2002). Figure 2-34 shows the description of a triangular facet needed for triangulation.

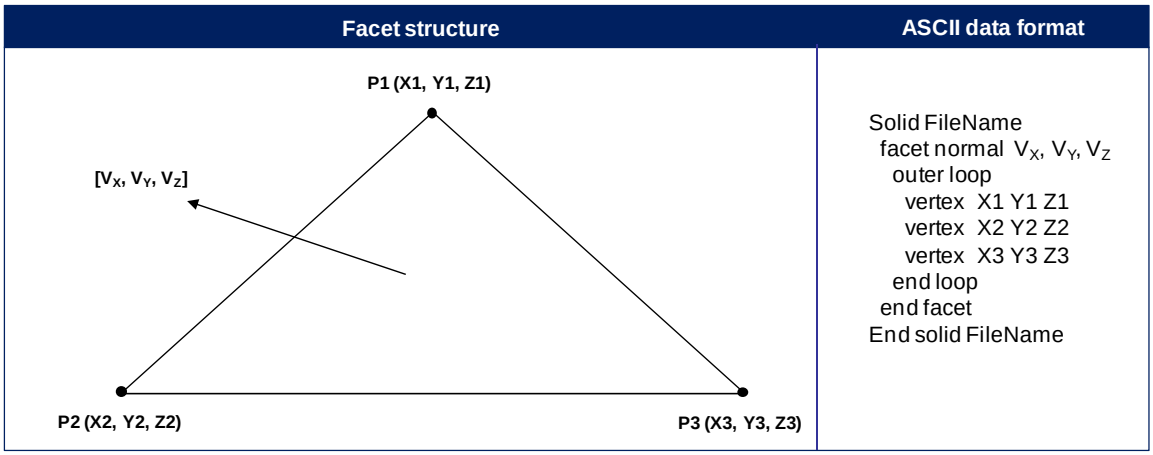

Figure 2-34: Triangulation principle (adapted from Lin, 2002)

The Cartesian coordinates system for three vertices are (*X1, Y1, Z1*), (*X2, Y2, Z2*), and (*X3, Y3, Z3*). The facet normal vector is (V_X, V_Y, V_Z). As depicted in Figure 2-34, a triangle

consists of three vertices and according edges. The normal vector defines the surface plane of the triangle (Fig. 2-34) and is positively vectored if being directed away from the volume. The presentation of complex and curved surfaces is described by triangles varied in size by a setted cusp height. That leads to approximated surfaces and models. To attain high surface quality such that higher approximations are derived, the number of set triangles has to be increased along with a fine adjustment of the cusp heights (Fig. 2-35).

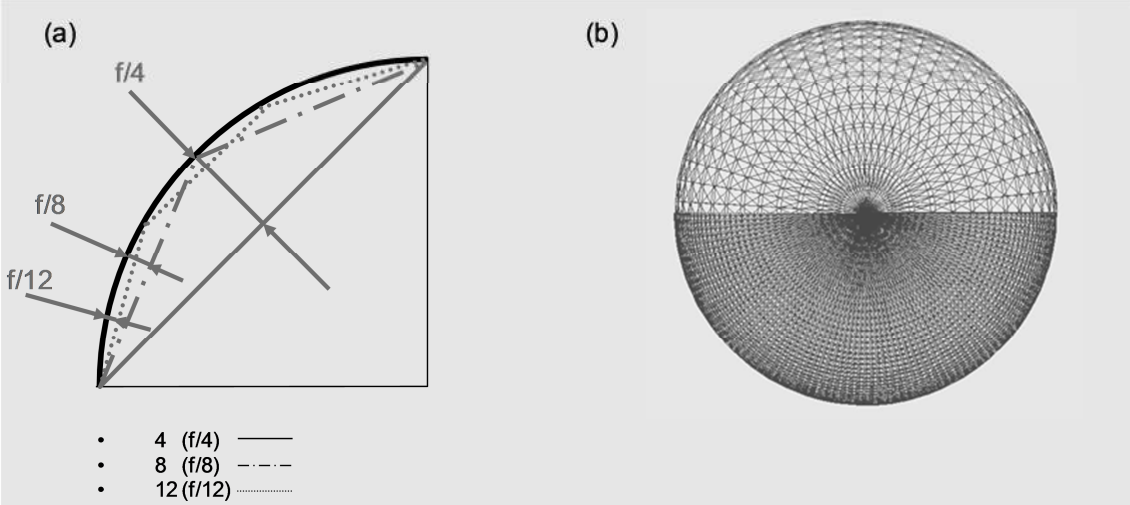

Figure 2-35: STL Approximation (Gebhardt, 2007)

Figure 2-35a shows the example of a circle that can be described by four (f/4), (f/8), and (f/12) straight lines (a). Figure 2-35b shows how the approximation influences the dimensional accuracy of a sphere. Generally, a larger number of triangles increases accuracy, but also the amount of data.

A decisive point in medical RP is the processing of large data volumes that are inevitably generated by 3D reconstructions from medical tomography data. There are two goals to medical RP using .STL: the first is to achieve very high quality and the second aim is to effectively operate with low data volumes so that arithmetic operations are performed faster. Unfortunately, when processing higher surface qualities, the volume of data increases disproportionately to the designated accuracy of the approximation (Zäh, 2006). A compromise thus has to be found (see Chapter 4).

Additionally, 16-bit attribute information can be added in an .STL file. Such attribute information is mostly used for coloring (Zäh, 2006). The attributes and coordinates of an .STL data set can either be generated as an ASCII (American Standard Code for Information Interchange) file or a binary file. A binary file has the advantage of generating smaller data volumes in comparison to ASCII source code that may be easier to read for humans. However, binary files are easier to read and to control for machines.

NC and CNC

NC is the abbreviation for numerical control (Kief, 2005). An NC program consists of a sequence of commands (e.g., words, sentences) controlling NC/CNC machine tools for the processing of predefined working steps. Accordingly, several movements of different axes can be carried out to realize arbitrary tool paths and to therefore process complex geometries at once (Kief, 2005).

The difference between a CNC program and an NC program is its input and controlling procedure. A CNC controller consists of one or more microprocessors which process work sequences. Addressing the controller, CNC software provides all the necessary functions such as positioning controller, speed controller, visualizations and editor, data saving and data processing.

An NC program is an overarching term for NC and CNC control. The generation of NC programs mostly proceeds in two sequential steps: In the first step, a CAM module calculates the trajectory of the cutting tool according to the designed part. In the second step, the tool path output as a machine controller independent Cutter Location DATA file (CLDATA), is converted by an NC postprocessor to a machine-specific NC program.
An NC program consists of an arbitrary number of sentences that describe the complete work sequence of a CNC machine's successive operations.

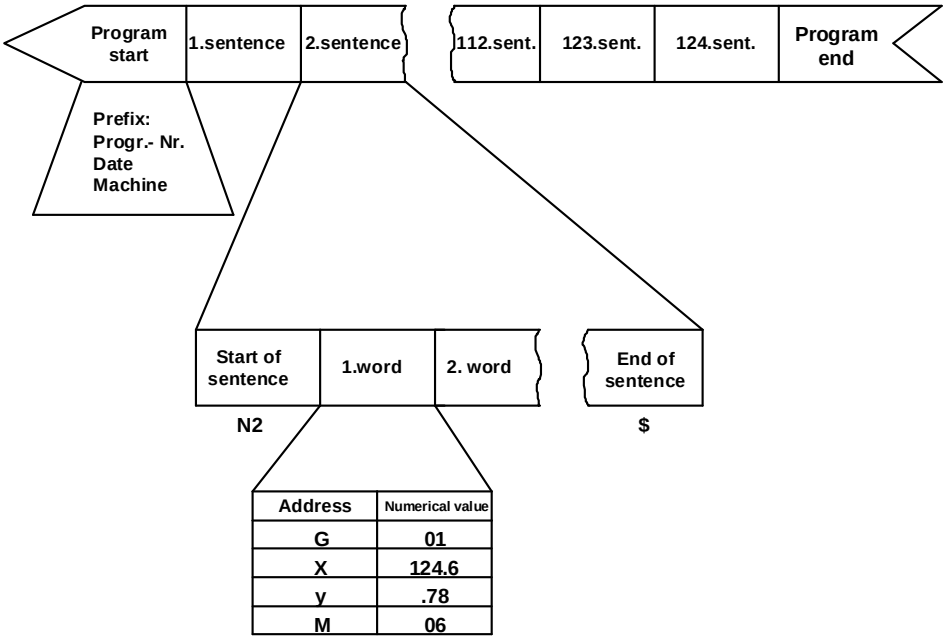

Figure 2-36: NC program structure (Kief, 2005)

The sentences in the NC program describe the geometrical working sequence and, if necessary, specific machine functions. Every sentence is related to a consecutive number and ends with the specific symbol $ (Fig. 2-36). Additionally, words in the sentences are

composed of address characters and numerical values. The address determines the function required for an operation by arranging the successive numerical values to the appropriate memory cell (Kief, 2005).
There are several commands that enable operation of a machine tool (Kief, 2005):

- **Geometrical commands**, used to realize relative movements between work piece and tool. Typical addresses are X, Y, Z, A, B, C,etc.
- **Technological commands**, used for selecting the feed rate (F), the spindle speed (S), and the tool (T)
- **Operating instructions**, used for selecting the type of movement (G)
- **Switching commands**, used for selecting the tools (T), and the operational settings, such as coolant supply on/off (M)
- **Subprogram commands**, used for repeating program steps (P, Q)

CAM applications typically use translators called post-processors to output a code that is optimized for a particular machine type or family.

2.2.4 Data processing

For generating machine code for manufacturing models specific data processes need to be run. Two possibilities are available for RP data processing: First, 3D CAD modeling can be carried out (Fig. 2-37). This process leads to CAD-internal or CAD-external data processes in CNC programming (Hastrich, 2005). This differentiation can be derived by Kief´s (2005) statement that in NC programming there are two possibilities: Either programming NC code directly in CAD system, i.e., CAD/CAM, or programming NC code in a separate NC programming system using imported geometry data from the CAD-system (Kief, 2005).
The CAD-internal data process is an integrated modeling and NC programming method using CAD and CAM in one plane. In CAD/CAM, the CAM module operates on the CAD-system kernel in order to use the geometric algorithms from the CAD platform for deriving the required NC code (Fig. 2-37)

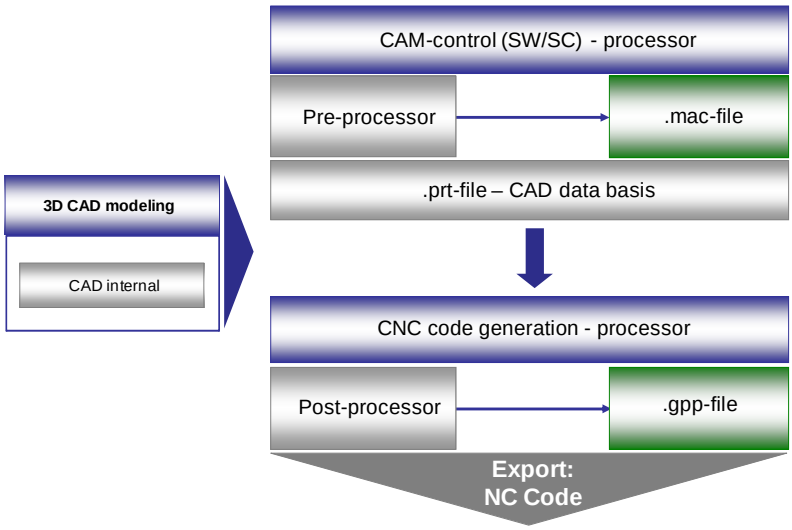

Figure 2-37: CAD internal process

For example, the use of the CAM module SolidCAM (SC) 2007 (SolidCAM GmbH) in combination with the 3D CAD system SolidWorks 2007, illustrates the typical data processes involved in running NC code programming (Fig. 2-37). The whole process is based on CAD data and starts with the generation of a control file (.mac-file) by a preprocessor to provide a post-processor machining operation. The post-processor operates a file containing the appropriate machine-related parameters (.gpp-file, G-Code) to generate NC code.

In conclusion, it has to be stated that the quality of a data process is characterized by its accuracy. Hereby, the CAD/CAM (CAD-internal) procedure serves as a highly accurate process. That is, data format conversions can be avoided thus reducing inaccuracies due to lost information. Moreover, that the CAD-internal procedure makes it possible to determine special operating procedures of specific surfaces, for later milling process. For example, it is possible to choose a cylinder (ruled surface) associated with a specific machining strategy. This automatic feature detection function is useful for 3D CAD models. But, the CAD/CAM (CAD-internal) procedure has the disadvantage that it cannot be operated with .STL files. In particular, for .STL file-based data processes, additional data processing possibilities have to be found. One such possibility is the CAD-external data process (Fig. 2-38). The CAD-external procedure is characterized by two different and independent procedures in data processing. The first procedure is standard 3D CAD modeling using the provided CAD functions in order to build a 3D CAD model (.prt-file) (Fig. 2-38).

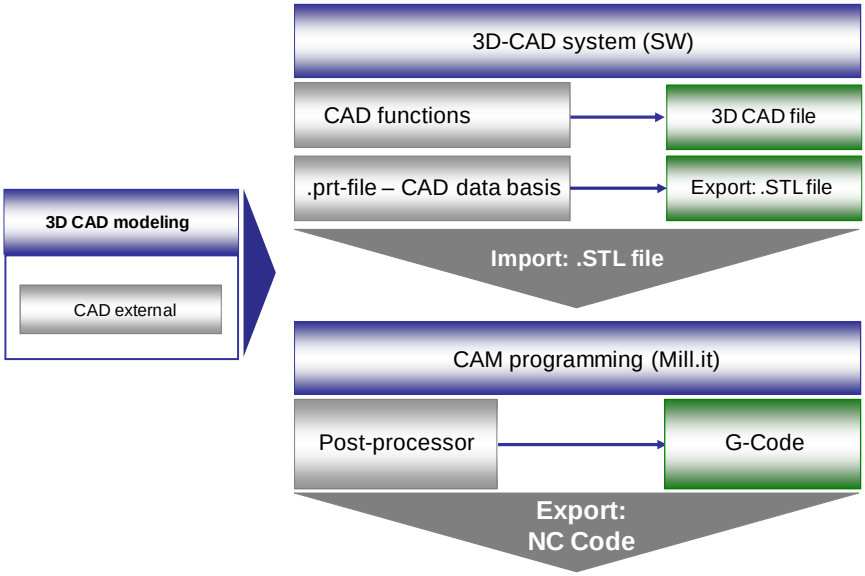

Figure 2-38: CAD External process

For example, the use of the CAM module Mill.it (COSCOM Computer GmbH) in combination with the 3D CAD system SolidWorks, illustrates the typical data processes involved in running NC code programming (Fig. 2-36). The 3D CAD model is converted into a 3D model on .STL file data basis and then imported in the second procedure of CAM programming. Hereby, it is possible to generate the needed NC code with the post-processor directly on the .STL file. An advantage Mill.it offers is the possibility to choose an appropriate supporting frame including bridges for mounting the work piece in the machine. This allows mounting even complex-shaped 3D models, which is normally laborious. The general idea of Mill.it is to support the user in processing .STL file-based 3D models for quasi-additive RP. A disadvantage of this process is that data format conversion has to be performed from the 3D CAD file format (.prt) to the .STL file format. Another disadvantage is that it is not possible to select specific surfaces for different machining operations. This is because the .STL file format that does not offer any features that can be selected separately. If a model features free-form geometries, problems can arise in milling exact geometry. The reason for this is that it is not possible to assign specific milling parameters, including specific tools for defined surface areas to fulfill particular manufacturing demands (e.g., transparent surfaces).

In carrying out RP in medicine, a fundamental problem is that no complete 3D CAD files can be derived from a 3D reconstruction process. The only way to post-process a reconstructed 3D model is to derive a .STL file that is generated by a meshing algorithm, such as MC. Attempts at creating point clouds to create NURBS-generated surfaces that are representational of a model, have not shown sufficient results. The problem is that in most cases medical models contain a lot of data that lead to very large file sizes. Today's 3D CAD systems cannot cope with gray value data files (point clouds) larger than 1 MB (e.g., SolidWorks). Therefore, only processes that can operate with .STL-formatted 3D models are

possible. Medical application features the additional goal of guaranteeing high accuracy in the production of models with specific attributes (e.g., transparency).

2.2.5 Transparency

A suitable material for manufacturing transparent RP models is plastics. Investigations have revealed that the RP procedure of CNC milling is ideally suited for fabricating for transparent surfaces. Hastrich (2006) found that polymethylmethacrylat (PMMA) is suitable for producing transparent models by means of CNC milling. Producing PMMA, methacrylic ester is processed in a radical polymerization to generate crystal clear high-molecular-weight polymer (Schwarz & Ebeling, 2005). PMMA has the following attributes (Schwarz & Ebeling, 2005):

- Hardness, solidness and rigidity
- Scratch resistance and burnishing ability
- Thermal endurance
- Transparency approx. 92%
- Good electrical characteristics and dielectric properties
- Low absorption of water

PMMA is available in two forms: PMMA casted (GS) and PMMA extruded (XT). PMMA (GS) offers a manufacturing advantage in terms of making machining easier (Hastrich, 2006). PMMA (XT) tends to melt in manufacturing and smudges the cutting edges of tools. Although PMMA (XT) is available at a cheaper price, PMMA (GS) is the preferred material for manufacturing transparent RP models.

Transparency of RP models is often in high demand, especially in systems in which interior flow is not well understood, e.g., in the field of human medicine dealing with upper airways and bronchial tree (Gebhardt, et al., 2005). For visualizing and analyzing the interior processes of a system consisting of cavities, contact-free measurements or optical measuring systems have to be used. Therefore, in such situations, transparent models have to be used to produce usable results.

The term transparency encompasses the words light transmission, scattering, and transparentness (Michaeli, 1999). Light transmission describes the relation of light that has passed through a body and incident light. In the case that there is light dispersion, then there is scattering (Michaeli, 1999). Transparentness is not of good quality if defined patterns or

points are blurred. Low transparency can result due to low surface quality arising from surface irregularities (Michaeli, 1999). During the chipping procedure, striae, rills, and corrugations have a negative effect on surfaces that should be transparent (Wimmer, 1989).
Plastics are used frequently in RP applications and biomedical engineering (Bertsche & Bullinger, 2007; Gebhardt, 2007). Transparent plastic models are characterized by various optical appearances. The optical properties of thermoplastics are determined by their chemical constitution of macromolecules, which can be amorphous or semi-crystalline (Domininghaus, 2005). Amorphous and semi-crystalline thermoplastics have different optical appearances: semi-crystalline thermoplastics are opaque or milky and amorphous thermoplastics transparent (Domininghaus, 2005). A typical amorphous thermoplastic is PMMA. Previous analyses carried out by Hastrich (2006) revealed a relation between transparency and surface quality. Transparent surfaces show a lower roughness than opaque-looking surfaces. In evaluating a technical surface, surface roughness can be used as an indicator for transparency. The roughness of a technical surface is described by the average surface finish R_a and is the arithmetic mean of the total profile deviation y within a defined measuring length l (DIN 4762, 2008).
A transparent surface is characterized by high surface quality. However, average surface finish R_a is low and stable. A typical value of R_a for a transparent surface is R_a = 0.03 µm (De Zelicourt et al., 2005).

2.3 Virtual prototyping

VP technologies aim to establish realistic simulations for different process, objects and systems in computer-generated virtual worlds in order to shorten the product development process. Users should be involved in virtual scenery to interact with digitalized processes and objects. VP is a process of using a digital model, rather than a physical model, for testing and evaluating specific product characteristics.
Virtual reality (VR) is a procedure typically carried out in product development processes and can be used in VP (Bergers, 2009a). VR offers continuous development of interactive, 3D simulation and employs specific input and output devices. As such, it provides a tool to perform a number of what-if studies, and hence supports an understanding of a model. The purpose of VR is to reduce the iterations of product development cycles.
The medical field offers various possibilities whereby VR can contribute to research and application (Bullinger and Bauer, 1994; Székely and Satava, 1999).

2.3.1 Medical applications in virtual reality

VR is the term commonly used to describe a human–computer interface that enables users to interact with computers in a radically different way. VR consists of a computer-generated, multidimensional environment, and interface tools that allow users to:

- immerse themselves in the environment,
- navigate within the environment, and
- interact with objects and other inhabitants in the environment (Greenleaf, 2004).

According to Bullinger´s and Bauer´s (1994) findings, VR has the potential for broad application in the field of medical research, including medical training (Berlage, 1997), therapeutic use supporting surgery (Grönemeyer et al., 1996), and studies in the field of neuroscience (Glantz et al., 1997). Moreover, VR is an application that can be used for surgery planning Robb, 2008), enabling medical experts to practice a wide variety of health care tasks ranging from performing triage to emergency first aid to coordinating planning and training (Zajtchuk and Satava, 1997).

In addition, displaying a medical model in a VR environment may enhance comprehension by adding stereovision and interactivity. An example of a VR technique for visualizing 3D models in a VR environment is stereovision.

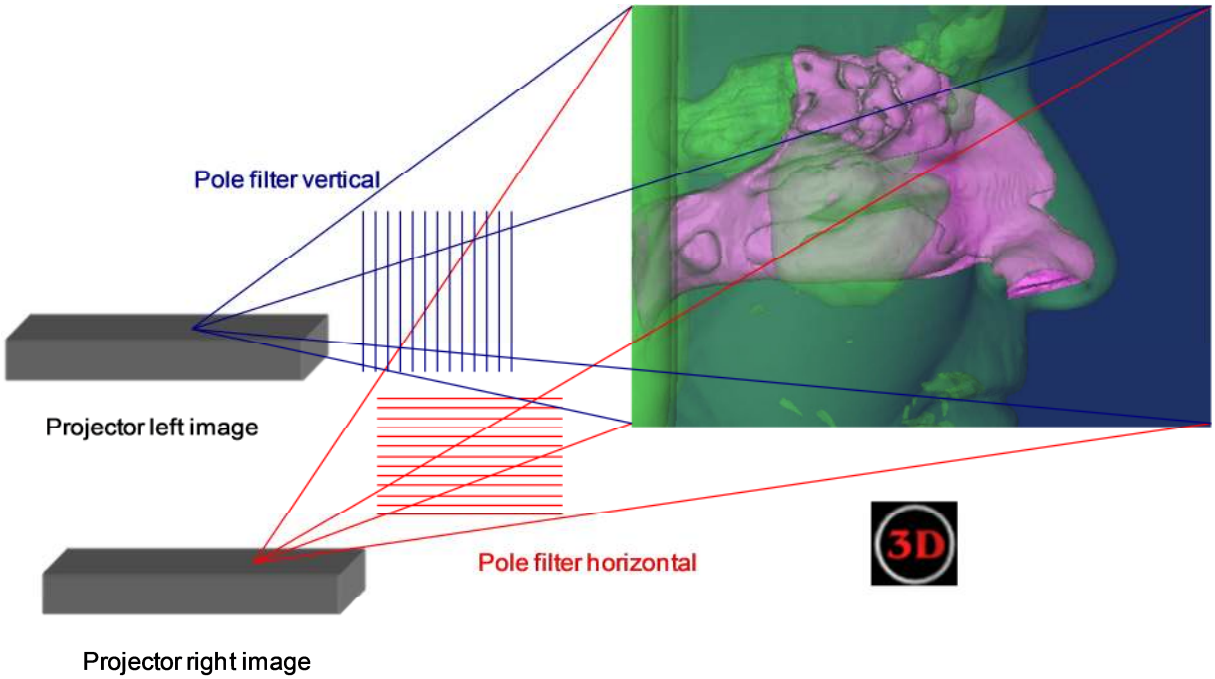

Figure 2-39: Medical VR using passive stereovision system

A frequently used stereovision system is the power wall. It belongs to the category of passive systems in the case that projectors used are positioned behind the visualization wall (Fig. 2-39). VR typically employs the .VRML data format, which is suitable for defining virtual worlds.

An in-depth analysis of the state-of-the-art of medical applications in VR is given in Mallepree et al. (2010).

2.3.2 VRML

The .VRML format is a description language for modeling interactive, virtual 3D worlds and 3D objects. The arrangement of 3D objects and their relation to each other is defined. Moreover, the .VRML format contains an interface to the programming language JAVA.

A .VRML file contains polygon scenery, which is based on objects that are arranged hierarchically. This hierarchal-based data is named scene graph and defines the object's relation. Nodes describe the geometry of a polygon object. Additional nodes are used to describe material attributes such as colors and reflections. A node consists of fields that contain values for describing the condition of a node in parametric representation. In such a parametric representation, the fields of a node contain the points of the polygons as well as the indexes that describe the surfaces of the polygons. By grouping nodes, the nodes of polygon scenery are compiled. A variety of additional nodes can be used for defining a scene. For implementing interaction and animation, events are used to control nodes. Events are edited by the following data types: eventIn, eventOut and exposedField. The transfer of events between nodes is done by using appropriate route commands (Kloss, 1998).

An alternative to event passing via routes is to pass references to .VRML nodes as values for fields in a script node. A script node is used to program motion in a scene. Script nodes typically signify a change or user action, receive events from other nodes, contain a program module that performs computation, and effect change in a scene by sending events. A script encapsulates JAVA code and provides naming conventions for interconnecting JAVA variables with field values in a scene. Interfaced JAVA classes import the .VRML class libraries in order to provide a type conversion between JAVA and .VRML

3. Conclusion and demand for a medical prototyping process

RP and VP are technologies that can have great impact on the medical field. Applications of RP traditionally used as support in product development should interface with medical practices.

As stated by Wohlers (Wohlers, 2007) there is a need for RP in the following range of applications in order to support product development. A survey of 85 international companies interrogated the extent to which applications are needed:

- Functional models – 17.4%
- Visual aids (for engineers, designers, architects, medical professionals) – 15.3%
- Fit and assembly – 12.1%
- Rapid manufacturing (custom and short-run production) – 11.7%
- Patterns for metal castings – 9.9%
- Presentation models – 8.9%
- Tooling components – 4.7%
- Ergonomic studies – 2.7%
- Visual aids (for toolmakers) – 2.4%
- Patterns for prototype tooling – 2.2%
- Fixtures and manufacturing aids – 1.7%
- Other – 3.2%

Considering Wohlers investigations, one can see that there is a great demand for functional models (17.4%) and visual aids (15.3%), including for medicine. The general contribution of RP models in medicine is described by the Phidias validation study of stereolithographic models in Europe in 2001 (database, N=172 questionnaires). Reported reasons why a model may be useful are given by surgeons, in Figure 3-1.

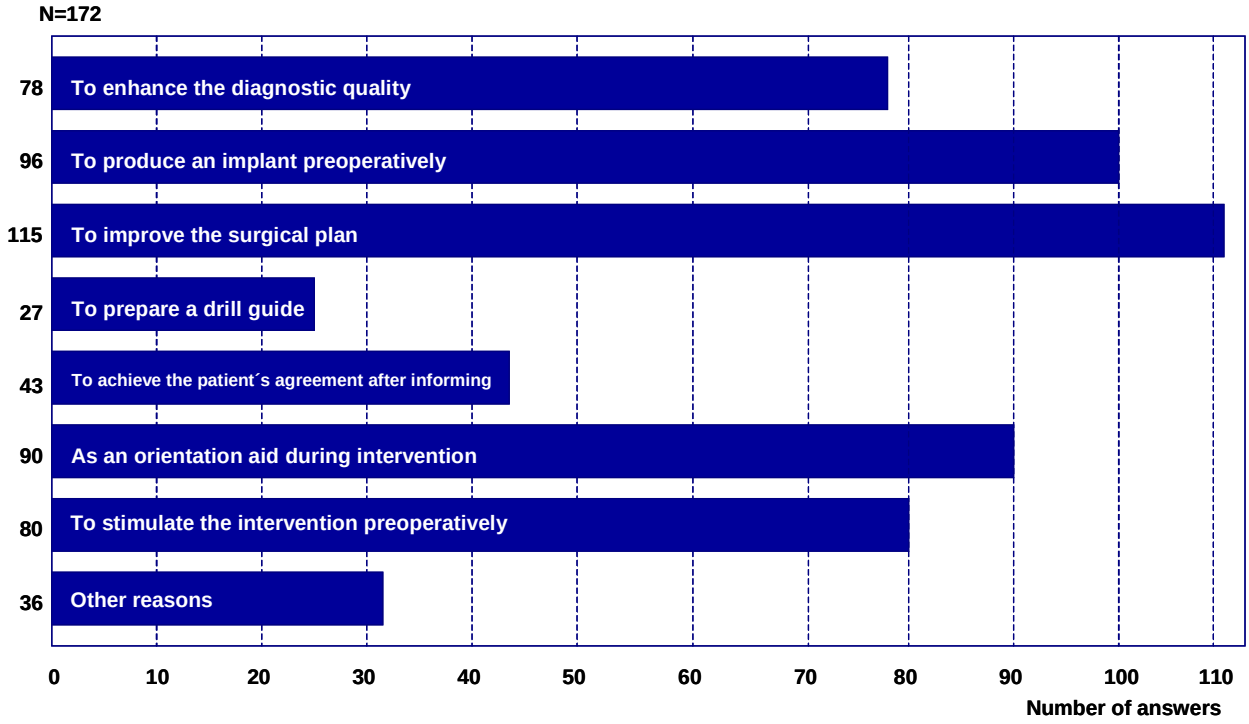

Figure 3-1: Phidias study (adapted from Wulf et al., 2001)

Most surgeons (115) believe that medical models improve surgical planning. They also stated that medical models could be used for producing an implant preoperatively and could support orientation during executed surgery. According to Wulf (2001), these results suggest that the use of medical RP models would help to improve the quality of planning, communication, and procedures in medicine. Regarding use of RP models for presurgery planning, 22.1% of surgeons reported a decrease of saved operation-time of 2 hours or more and 23.8% reported that using RP models can save up to 1 hour execution time (Wulf et al., 2001). But, this time-saving effect depends on a surgeon's experience. Highly experienced surgeons are able to perform faster using planning models than average-experienced users (Wulf et al., 2001).

Computer-assisted, model-based planning procedures like VP and RP are able to cover specific modifications of "virtual anatomy" for surgical intervention planning in order to evaluate a potential therapeutic outcome.

CAS is the field that covers innovative support for surgical treatment by computer assistance. The general objective of CAS is to support surgeons in achieving better clinical results. This is concurrent with the aim of lowering costs, reducing recovery time, and a reducing need for repeated surgery (Taylor et al., 1993). CAS covers the full spectrum of treatment, from diagnosis through preoperative planning and processing to postoperative evaluation and follow-up (Taylor et al., 1993) (Fig. 3-2).

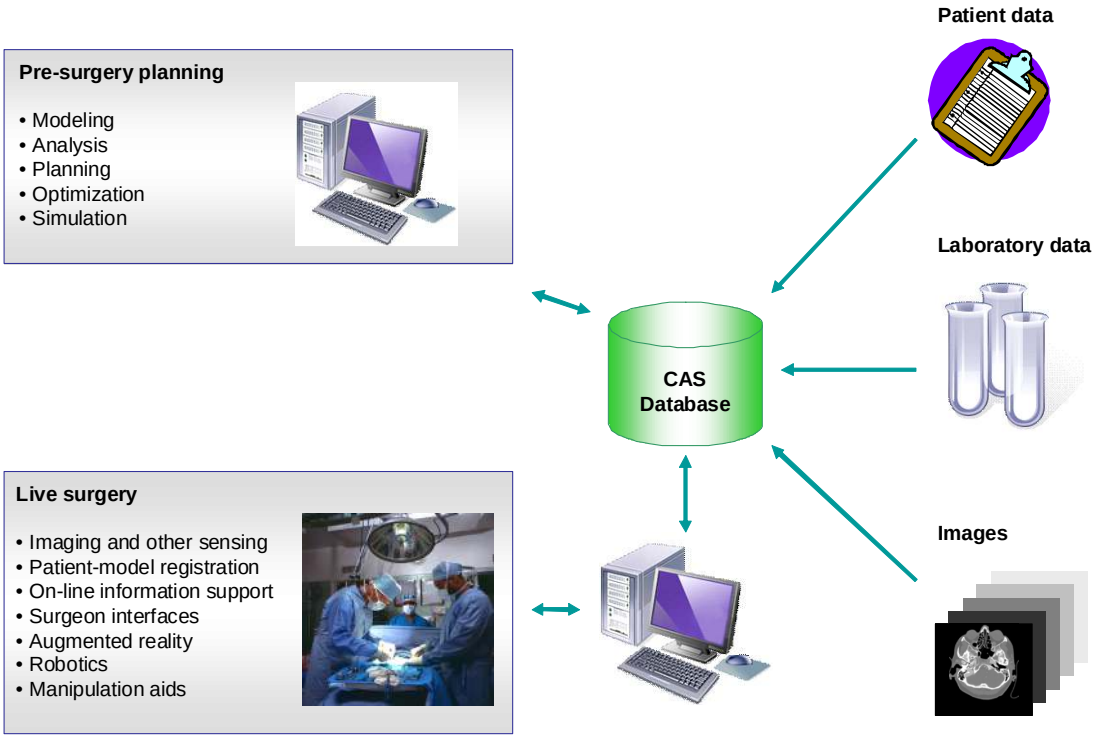

Figure 3-2: CAS (adapted from Taylor et al., 1993)

The CAS principle consists of a database that contains all medical information needed for surgery. The database includes: a patient's medical data, laboratory data, and/or images for presurgery planning and executed live surgery. In presurgery planning, CAS supports the modeling, analysis, planning, optimization, and simulation of a medical case. When carrying out live surgery, a computer is used to assist in imaging, registration or manipulation aids with medical data from the database. As early as 1985, Murphy and colleagues stated that CAS planning has a deep impact on:

- Preoperative planning with computer-generated 3D models
- Optimal preparation in complex interventions
- Selection of optimal implant geometry
- Design of individual implants
- Adjustment of implants using facsimiled model
- Selection of suitable surgery tools
- Improved patient information
- Shortening of anesthetics times
- Reduction of surgery times and patient burden
- Reduction of risk of repeated surgeries
- General cost optimization

Today, the great increase of possibilities for using engineering tools and methods in medicine allows surgeons to offer a wide-range of methods in investigating pathologies and general treatment. Taylor stated in 1993 that systems that combine medical data information with intraoperative (during surgery) sensing, manipulation devices, graphics, and a variety of other human-machine interfaces would have a considerable impact on surgical execution (Taylor et al., 1993).

Following Taylor's vision, individual anatomical models are now available as either virtual or physical models for use as medical aids. Moreover, the possibility to generate facsimiled medical models is possible using VP and RP.

Model accuracy is the principal weakness of medical RP models (Barker et al., 1994; Giannatsis, 2007) as well as of medical VP models. Even though medical model accuracy is the principal weakness this is getting less of a problem as technology improves (Gibson, 2005b; Gibson et al., 2006). Previous work in biomodeling (Chapter 2.1) as a preprocess for VP and RP applications is not predominantly focused on accuracy. In order to systematically enhance accuracy the complete procedure of reproducing medical images into medical models has to be analyzed. The following optimizations must be focused upon when enhancing biomodeling:

- Scanning parameters
- Segmentation
- Surface meshing

An RE and 3D-reconstruction process is required that enables generation of virtual volume models appropriate for RP and VP applications. To prevent failure due to model deviation, scanning parameters need to be selected appropriately. In this way, appropriate segmentation of anatomical structures is enabled. Also, surface meshing should be enhanced to achieve the best possible model accuracy and surface smoothness in combination with file size reduction, if needed.

Summarizing the current status of RP (Chapter 2.2) and augmenting statements of Gibson (Gibson, 2005a, Gibson et al., 2006), Noorani (2005) and Wetzel et al. (2005) about current disadvantages of RP in medicine, the following limitations need to be remediated:

- Connection between RP machine and RE
- Staircase effects on RP model surfaces

- Limited transparency of RP models
- Limited accuracy of scanned data (RE) and final RP model (e.g., shrinkage)
- Limitations of usable materials
- Irreversibility of RP models (e.g., press-fitted assembly)
- Exchange of model morphologies
- Joining accuracy in quasi-additive RP

In order to solve these issues, a valid data process should be established to accommodate all phases, from initial data acquisition to manufacturing. One possibility is to use the .STL format for transferring medical image data generated as triangular volume models (Chapter 2.2.3). In addition, triangulation parameters for deriving a 3D reconstructed .STL model need to be determined to provide accurate machining templates. The majority of systems only allow setting chord error. Therefore, a systematic analysis of meshing parameters has to be made to satisfy the demand in RP to produce models with better accuracy. The accuracy of the generated surface mesh affects the quality of the approximation and fidelity of the final model. The quasi-additive RP procedure is ideally suited for producing medical models. By milling parameters that have to be evaluated for anatomically shaped free-form surfaces, staircase effects can be avoided, better transparency is realized, inaccuracies are reduced, and various materials can be machined. Reversible models can be realized by an appropriate joining principle. Moreover, a logical model configuration is needed to solve the problem of testing variants and different model morphologies, respectively. Normally, a model is generated separately for each situation repeatedly. To date, an appropriate medical RP procedure for generating modular built models does not exist.

Vartanian et al. (2004) used VR to demonstrate the possibility of displaying the human nose as a 3D VR model. However, it remains unknown whether this study assessed the accuracy of the complete procedure of biomodeling and VR processing. Moreover, the use of parameters for performing the complete procedure, from data acquisition to VR stereoscopic display, is rather unclear. Glombitza et al. (1999) outlined different methods and applications in the field of VR. The accurate processing of VR data remains unknown. In summary, current disadvantages of VR data processing in medicine that need to be optimized for a possible use in medicine include:

- Connection between VR application and RE
- Accuracy of generated virtual models

The appropriate data format of VR in medicine is .VRML. Therefore, the 3D reconstruction process should enable the direct derivation of .VRML models out of medical image data. Additionally, parameters have to be determined that allow the accurate derivation of triangulated .VRML models that can accurately display even complex anatomies in detail.
Currently tomographic slice images are used for the presentation of medical image data and standardized static 3D visualizations comprise surgical planning support (Gering et al., 2001; Hu, 2005; Lee et al., 2005; Vartanian et al., 2004). However, there are major limitations: (a) The difficulty to recognize exact spatial relations between two or more objects, and (b) the occlusion of relevant objects or parts thereof. Especially in minimally invasive surgery, the surgeon is confronted with difficult conditions during the surgical procedure. In contrast to common surgery, direct insight into the specific area of interest is missing. Therefore, a concept is needed that extends the use of VR in medicine in order to provide a supportive instrument for medical experts.

Moreover, a concept that integrates a process for generating complex virtual and physical medical models is missing. Although various publications show possible applications of VR and RP in medicine (Cai et al., 2004; Choi et al., 2002; De Zelicourt et al, 2005; D'Urso et al., 1999; Gibson, 2005a; Ma et al., 2001; Szekely & Satava, 1999) a process that combines both the VR and the RP application even for complex medical models is lacking. Also, a medical classification that assigns VP and RP to possible applications in medicine is unavailable. Such a classification would support finding an appropriate application for a given case of use.
To date, there is no prototyping process in biomedical engineering available that is composed of consistent process steps. The findings from the present literature show no congruence in process design. Tomographic image data has made available different model generation processes: 3D reconstruction processes that use .DICOM data and 3D reconstruction processes that use point cloud data. Moreover, there are approaches that reveal the possibility of generating triangulated 3D models and approaches that attempt to generate NURBS-based CAD models. In sum, all approaches lack defined process parameters that would enable generation of medical models with defined repeat accuracy in a defined time span.

In summary, an embedded prototyping process is needed that allows the generation of complex virtual and physical medical models, as rapidly and accurately as possible. In the following a prototyping concept in biomedical engineering is presented that includes a process, which is verified by experimental studies and examples of use.

4. Prototyping process concept

To broaden Taylor's vision introduced in 1993, the present thesis aims to establish computer assistance by means of RP and VP in medicine. This includes the use of RP and VP in teaching and patient information, presurgery planning, implant generation, and medical research (Fig. 4-1).

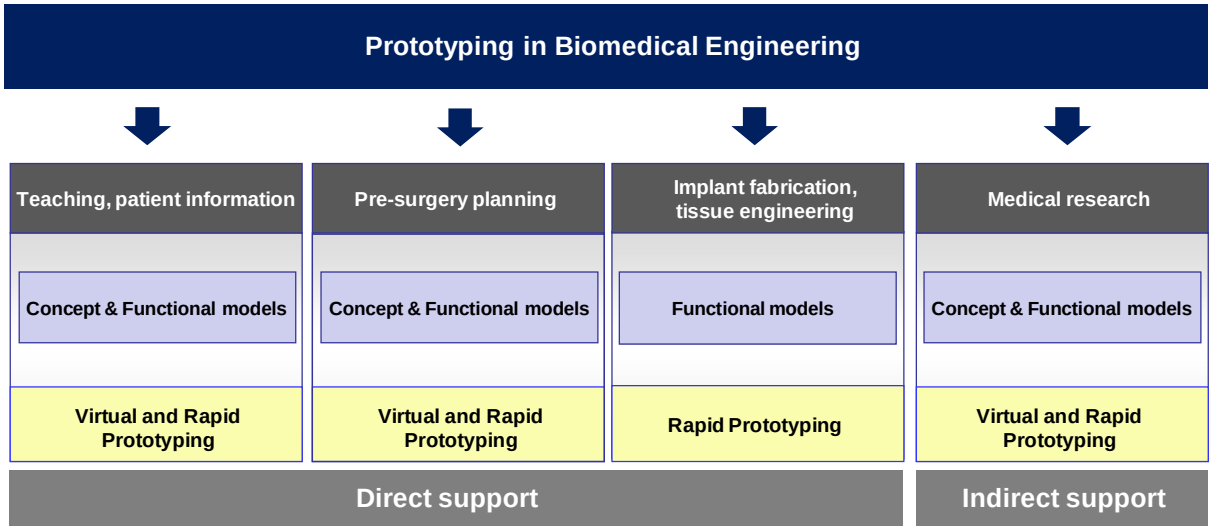

Figure 4-1: VP and RP in biomedical engineering

Prototyping procedures can be used either as direct surgical support or indirect medical support. VP and RP in biomedical engineering fulfill the requirements in teaching and patient information as well as in presurgery planning and implant generation. Especially, in cases of complex surgery, biomedical prototyping procedures may become a necessary tool for surgical intervention.

Presurgery planning has a very important role in medicine and is in the focus of the present thesis. The use of medical models supports surgeons in planning complex surgical procedures. That is to study the object of interest before the surgery. This can help increase surgical precision, reduce time spent on procedures, reduce costs and avoid risks during surgery.

In future, RP procedures can be applied for the generation of implants (Eufinger et al., 1995; Hierl et al., 2006). Recent investigations deal with the fabrication of human tissues using specialized additive printing machines.

Another mode of support for surgical planning is to use functional models generated with either VP or RP, in cases where medical research is needed. For example, an experimental evaluation of a facsimile may be required to analyze results for subsequent application in reality. A specific example is the study of the not completely understood human nasal airflow

(Bergers et al., 2010; Finck et al., 2007) by means of experimental models (see Chapter 6). Taken as indirect surgical support, interventions or manipulations executed before surgery will permit drawing conclusions about a patient later. This means that detailed investigations of a potential case in which symptoms are described by a patient, but where pathologic underpinnings of specific dysfunction are not obvious for medical experts.

Due to the restricted possibilities to examine the pathological underpinnings of medical cases where possible dysfunctions are difficult to detect using noninvasive investigation methods, medical VP and RP models offer cutting-edge aids for finding intricate and hidden details of site of trauma. Although RP has not been developed directly for manufacturing medical models (Gibson, 2006), it is well suited for use in medical applications due to the fast and automated manufacturing of models it offers.

As depicted in Figure 4-2 a basis for using VP and RP models in presurgery planning is proposed.

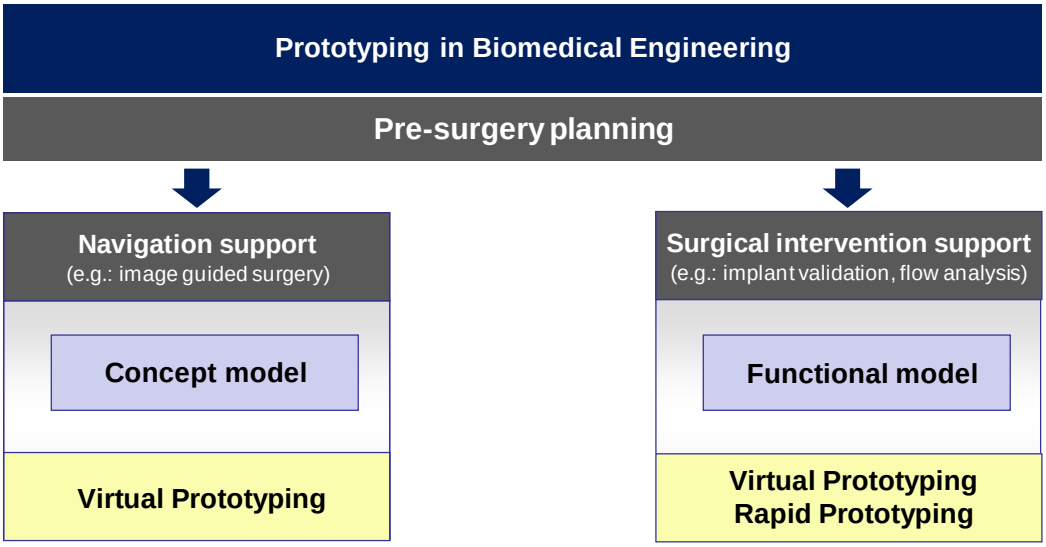

Figure 4-2: Medical prototyping in presurgery planning

VP can be typically used as a support in navigation, for example, image-guided surgery. In such a case, concept models are well suited because they allow a full overview of anatomical geometry to support a surgeon in localizing possible pathologies. Moreover, support of surgical interventions may employ VP for planning the assembly of an implant virtually as well as use RP for planning an implant joining procedure using a physical model in combination with real tools and instruments (e.g., hip surgery). Hence, medical models can allow practicing surgery and enable multiple trial evaluations for optimizing surgery interventions prior to invasive operations. This is in agreement with Lightman's report in which he emphasizes the need for expandable RP models that assist practicing surgery to improve subsequent surgical results (Lightman et al., 1995).

4.1 The medical prototyping process

Standard RP procedures may be viewed as insufficient in providing medical models for functional usage. Medical applications demand that medical models be of highest possible quality, manufactured in the shortest possible time and with reasonable cost (Fig. 4-3).

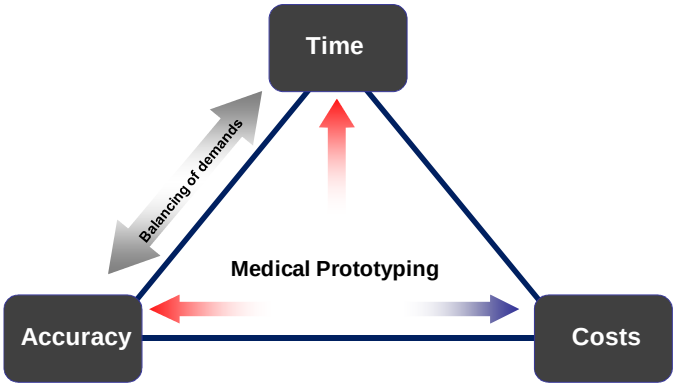

Figure 4-3: Balancing demands in medical prototyping

To date, medical treatments using innovative technologies are becoming more and more expensive in manpower. Accompanying this, possibilities for using new technical developments are increasing exponentially. Thus, medical applications must be designed to meet these requirements and satisfy needs of new developments by lowering the cost of technology so that it can be used for a wider number of cases. One possibility is the use of the VR technology. The interaction with 3D visualizations can accelerate the comprehension of image data of individual patients. Medical visualization in VR environments can support medical experts to understand 3D image information in less time with less elaboration (Mallepree et al., 2010). Another possibility to increase the level of model accuracy and to decrease fabrication time of functional RP models is the quasi-additive RP process; this is a knowledge-based refinement of existing RP procedures. When functional models are needed to explore human anatomy by means of a physical model the quasi-additive RP process enables high accuracy models to be produced in any machinable material (Mallepree & Bergers, 2009c). Fulfilling the demands stated in Chapter 3 implies that a medical prototyping process should be established as a tool in biomedical engineering for presurgery planning. This includes a definition of all process steps needed to generate and manufacture a medical model along with covering demands of accuracy and time (Fig. 4-3, red arrows). It should be possible to use as few process steps as possible in order to produce high-quality medical models in the shortest possible time span. As a consequence, resulting costs should be lowered (blue arrow). The procedure proposed in the present thesis is named medical prototyping process (MPP) and consists of two main process steps. The process steps are:

- Biomodeling (RE, segmentation, mesh editing)
- Application (RP, VR)

By means of the process layout, which is presented in Figure 4-4, an advanced approach of generating models for medical applications is introduced. First, that includes the arrangement of model generation processes and subsequent applications into a two-step procedure (biomodeling, application; blue bars, Fig. 4-4). Secondly, the approach comprises a complete process parameter definition that allows standardizing the entire process. The first step includes the use of imaging technology to generate 2D medical image data by RE of an individual patient's section, followed by a 3D reconstruction process (segmentation and mesh editing) to obtain a triangulated 3D model for medical prototyping (Fig. 4-4).

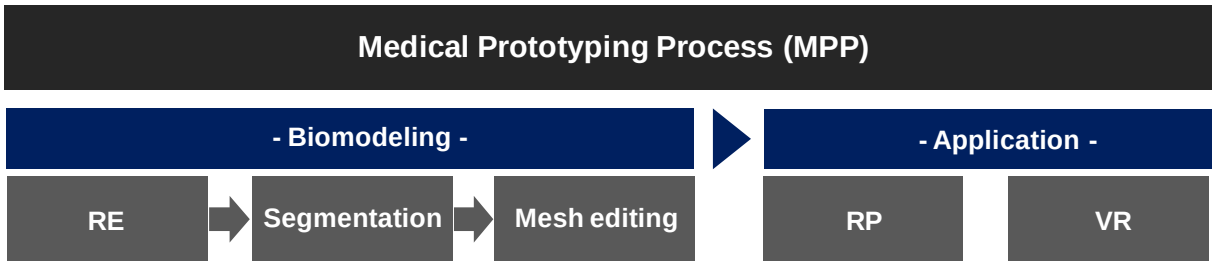

Figure 4-4: MPP Concept

The process of mesh editing includes the preparation of an adequate .VRML file for VR and the derivation of an appropriate .STL file for RP (Chapter 4.2.3). After the biomodeling phase, both a VR and RP application can be initiated. Underlying the realization of the two-step process are various sub-processes. A detailed process analysis and parameter determination is shown in the following.

4.1.1 Process sequence

As shown in the previous chapter, the process for generating medical models for VR and RP applications consists of process steps that have to be integrated. The objective is to avoid too many data formats and process steps in order to establish a shortened process sequence that is as automated as possible, and allows rapid and computerized processing of medical models. The MPP consists of two main processes; the process of biomodeling and the process of application (Fig. 4-5). The first process to start with is RE.

Reverse engineering

The process starts with the selection of an appropriate scanning machine and scanning parameters in order to generate medical images (Fig. 4-5). Those images have to be saved as .DICOM-files. This process of RE is followed by the process of segmentation.

Segmentation

The process of segmentation uses the provided image data from RE to define objects of interest. The step of segmentation consists of three sub-processes: If required a preprocessing is applied to optimize the provided images by means of filtering. An advanced filtering technique enhances final model accuracy by offering – in the second process of thresholding – an optimal basis for interpreting gray value contours. The third process of region growing optimizes the threshold result as previously mentioned in Chapter 2.1.3.

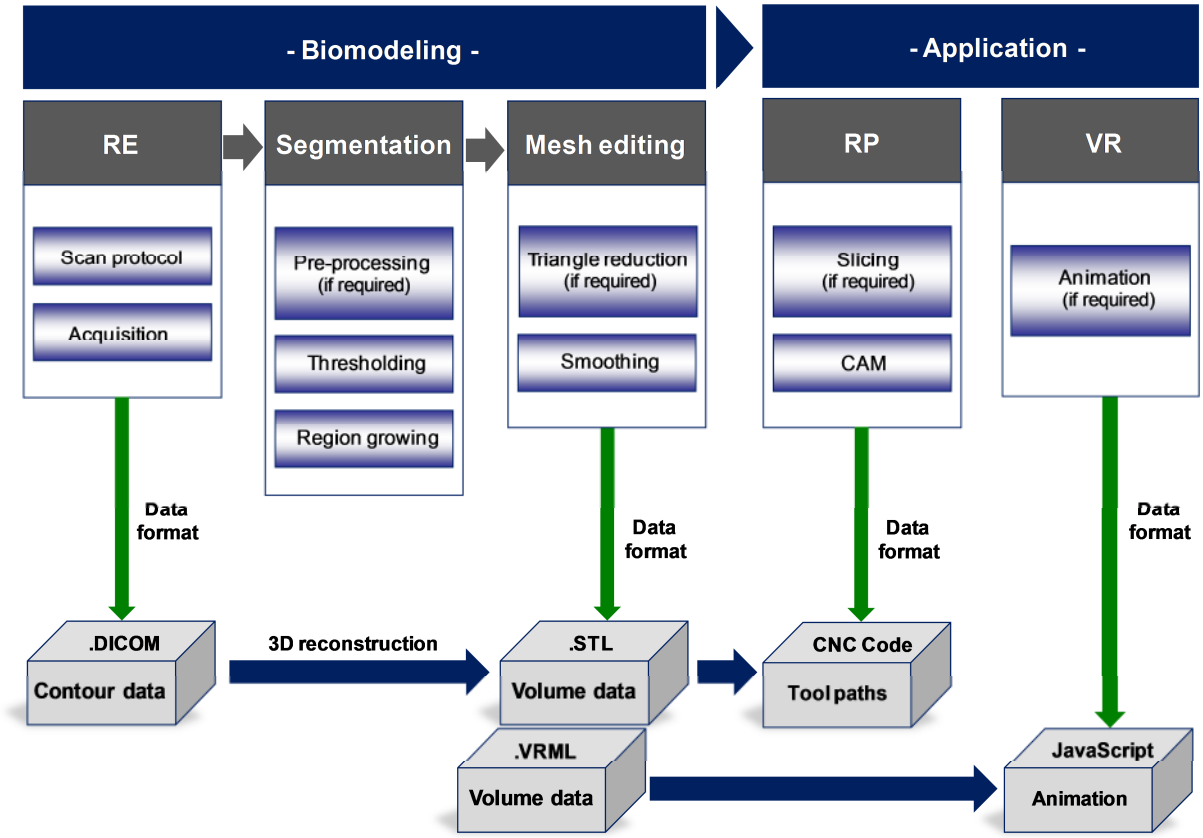

Figure 4-5: MPP Sequence

Mesh editing

An interface is established supporting the transfer of medical image data into technical data formats. This data transfer is realized using the .DICOM-format compatible 3D reconstruction software Mimics. The imported 2D image data sets (.DICOM-format) are either converted into the .STL format, which provides the basis for the following RP process steps, or, into the .VRML-format for carrying out the VR process.

.VRML mesh editing is referred to as .STL mesh editing because both the .VRML and.STL files are built by means of the same triangulation procedure and both use the same Descartes coordinate system. The difference is that .VRML stores all of its vertices together in an array structure whereas.STL stores all three vertices in each facet (Zhang et al., 2001)

The process of .STL mesh editing (Fig. 4-5) is needed to obtain accurate surface meshes. The description of complex, anatomical shaped surfaces by triangulation is often related to meshing irregularities. Such triangulation errors can be holes, overlapping triangles, or false-orientated triangles and normal vectors, respectively. The software-tool 3-Matic (Materialise N.V., Leuven) is capable of failure compensation operations and is thus used if such error compensations are necessary.
In sum, the objectives of .STL editing include:

- Smoothing of the relevant anatomical surfaces to optimize 3D reconstruction (e.g., staircases)
- Reduction of files size by triangle reduction, if needed
- Preservation of geometry details (undercuts, thin-build regions, etc.)
- Validated accuracy

Application

The VR presentation is a subsequent application process for displaying a model in 3D (Chapter 2.3). The software tool used in this thesis for creating VR scenery is Cosmo Worlds (SGI). When generating animation sequences, Cosmo Worlds is ideally suited. Setting up a VR presentation encompasses the following objectives:

- Grouping, arranging, and coloring of model elements
- Improvement of visualization quality
- Generation of animation

The drawbacks of static visualizations (Chapter 3) can be compensated for by interactive 3D VR visualizations (Mallepree & Bergers, 2009b). Nevertheless, navigating in 3D environments is time consuming and the viewer can lose sight of important objects or lose orientation (Bade et al., 2005). Some of the disadvantages of both static visualizations and interactive environments can be avoided by using animation, which effectively provide information in a limited and predefined time span.
This thesis presents a process for generating animation in VR of complex anatomies for surgical intervention planning. A novel procedure is applied to support surgeons, especially in minimally invasive surgery, in gaining insight in a particular surgical situation. Finally, the process of surgical intervention planning can be accelerated in terms of diagnosis and treatment planning.

3D stereoscopic vision is realized using the software tool VRED (Silicon Graphics). With regard to the display of 3D .VRML models VRED enables a precise adjustment of stereoscopic parameters (eye separation, parallax distance) and is therefore ideally suited (Lubnau, 2009). The principle of visualizing medical image content is described in Chapter 2.3.

For executing the RP procedure of CNC milling, tool paths have to be programmed. A software tool that is able to process .STL files is Mill.it (Chapter 2.2.4). In order to avoid data format conversions that reduce accuracy a .STL internal process is set up (Fig. 4-5). Using the CAM-module Mill.it allows running CNC code programming (Fig. 4-5). This .STL-based process is characterized by not using a 3D CAD system as data basis. An STL model is reconstructed in Mimics and directly imported into Mill.it. If further CAD operations have to be carried out, 3-Matic is used additionally (e.g., slicing). It allows running all main operations known from CAD systems carrying out triangular operations. If a 3D model is defined it can be uploaded into any CAM module which is capable of operating .STL-formatted 3D models. The advantage of this procedure is that it is possible to run the whole data process without making any data format conversions that may cause accuracy problems.

The requirements for programming CNC code to support milling machine operations include:

- Generation of tool paths for milling .STL slices
- Selection of appropriate tools, feed, cutting parameter, etc.
- Selection of suitable milling strategy (z-plane, zick, etc.)
- Optimization of operation time

The processing of manufacturing data is realized by the MPP concept introduced in Figure 4-5.

In the present investigation the generated manufacturing data are operated by a Heidenhein controlling unit. The milling machine used is a three-axis CNC machining center (Alzmetall BAZ 15). The objective in CNC milling is to provide a high level of accuracy by selection of an appropriate positioning and clamping procedure in combination with given programmed machining parameters.

5. Process analysis

An unsolved problem in generating medical models using prototyping technologies lie in the nonspecified process parameters of reverse-engineered and applied models. To verify the MPP, influential process parameters are analyzed.

5.1 Segmentation filter analysis

To determine the most appropriate segmentation filter with respect to accuracy of the complete process, arbitrary segmentation filters need to be evaluated. These may be analyzed via visual inspection of resultant segmentation images in reference to accuracy of the final 3D model. The following segmentation filters are tested:

- Mean
- Median
- Discrete Gaussian
- Curvature flow

Each filter is applied to two datasets by selecting filter parameters through a process of trial and error until similar noise reduction is observed. Exemplary anatomically shaped models are processed as reference. The models represent a segmented part from the nasal conchae inferior with a constant set threshold range. The reference models are based on high-resolution CT scans as shown in Table 5-1.

Table 5-1: Parameters: reference models segmentation filter

Parameters	Model 1	Model 2
Scan parameters		
Scanner	SIEMENS-Sensation Open	SIEMENS-Sensation Open
Resolution	512x512 Pixel	512x512 Pixel
Pixel size	0.342 mm	0.342 mm
Field of view	17.5 cm²	17.5 cm²
Slice thickness	0.60 mm	0.60 mm
Slice increment	0.60 mm	0.60 mm
Reconstruction filter	H60s	H50s
Model parameters		
File size	2,237 kB	1,224 kB
Number of triangles	45,352	25,060
Number of vertices	22,652	12,532
Gray-value range	-1024 → -255	-1024 → -255

The scan parameters (Table 5-1) result from predefined clinical data sets provided from the Alfried Krupp von Bohlen und Halbach Hospital (Radiology, Dr. M. Montag). After applying

the filters, both models are reconstructed as .STL models. They are used for conducting a part comparison (3-Matic) for measuring the model accuracy. As it can be seen in Figure 5-1, the original 2D images of model 1 contain more noise than model 2. More washy images can be seen in reference to model 2. This allows finding the optimal filter independent from the level of noise. How the CT internal reconstruction filters influence accuracy is measured additionally. Model 1 is acquired using a typical H60s filter for scanning the head region and model 2 is measured using the less sharp H50s filter that leads to the more washy images of model 2.

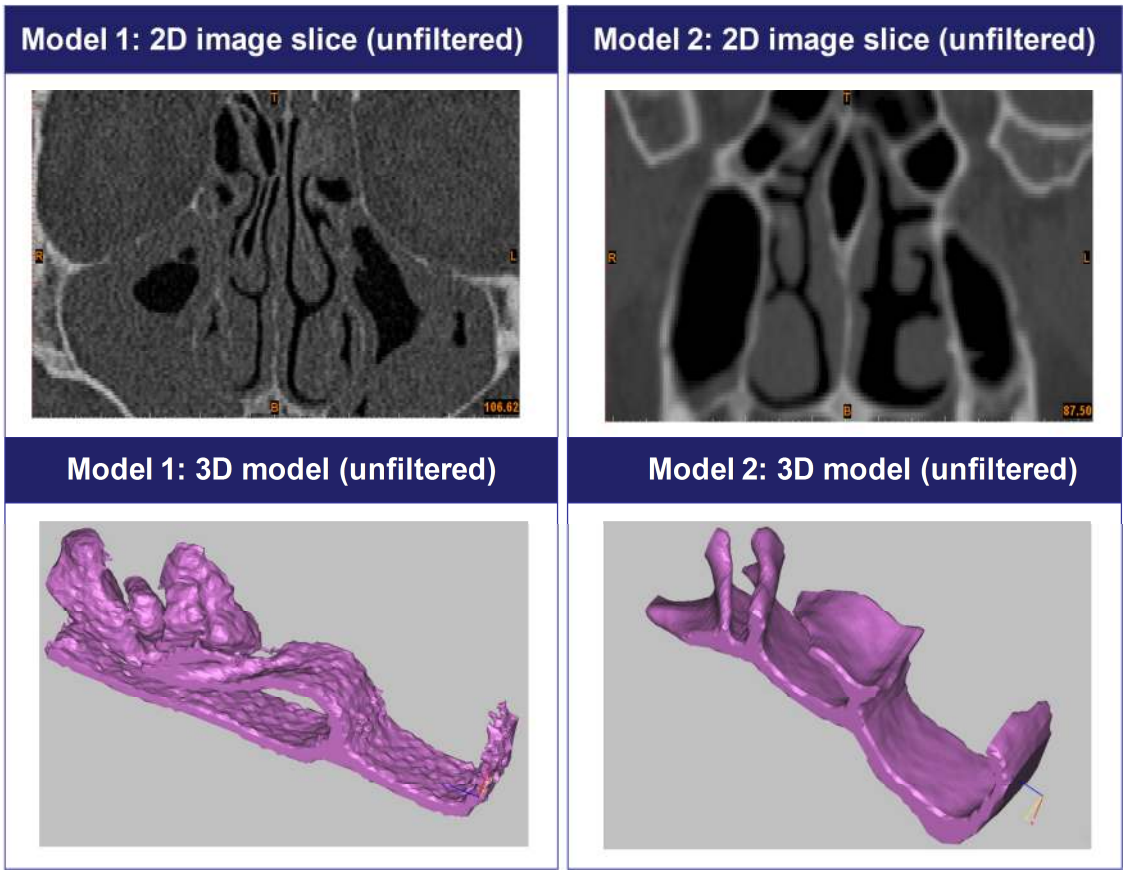

Figure 5-1: Process sequence segmentation filtering

As shown in Figure 5-1, the reconstructed 3D model surface is rough and full of fissures. Figure 5-2 shows the results for model 1 after applying the arbitrary noise reduction filters.

As demonstrated by Figure 5-2, both the mean and Gaussian filters tend to indiscriminately smooth the image, which leads to washy image representations due to the lack of edge preservation. In contrast, the median and curvature flow methods support edge preservation, and lead to the enhancement of boundaries. In consequence, the mean model deviations are smaller after applying the median or curvature flow filter. Nevertheless, the curvature flow filter leads to best model accuracy with a mean deviation of the final .STL model of 0.801 mm.

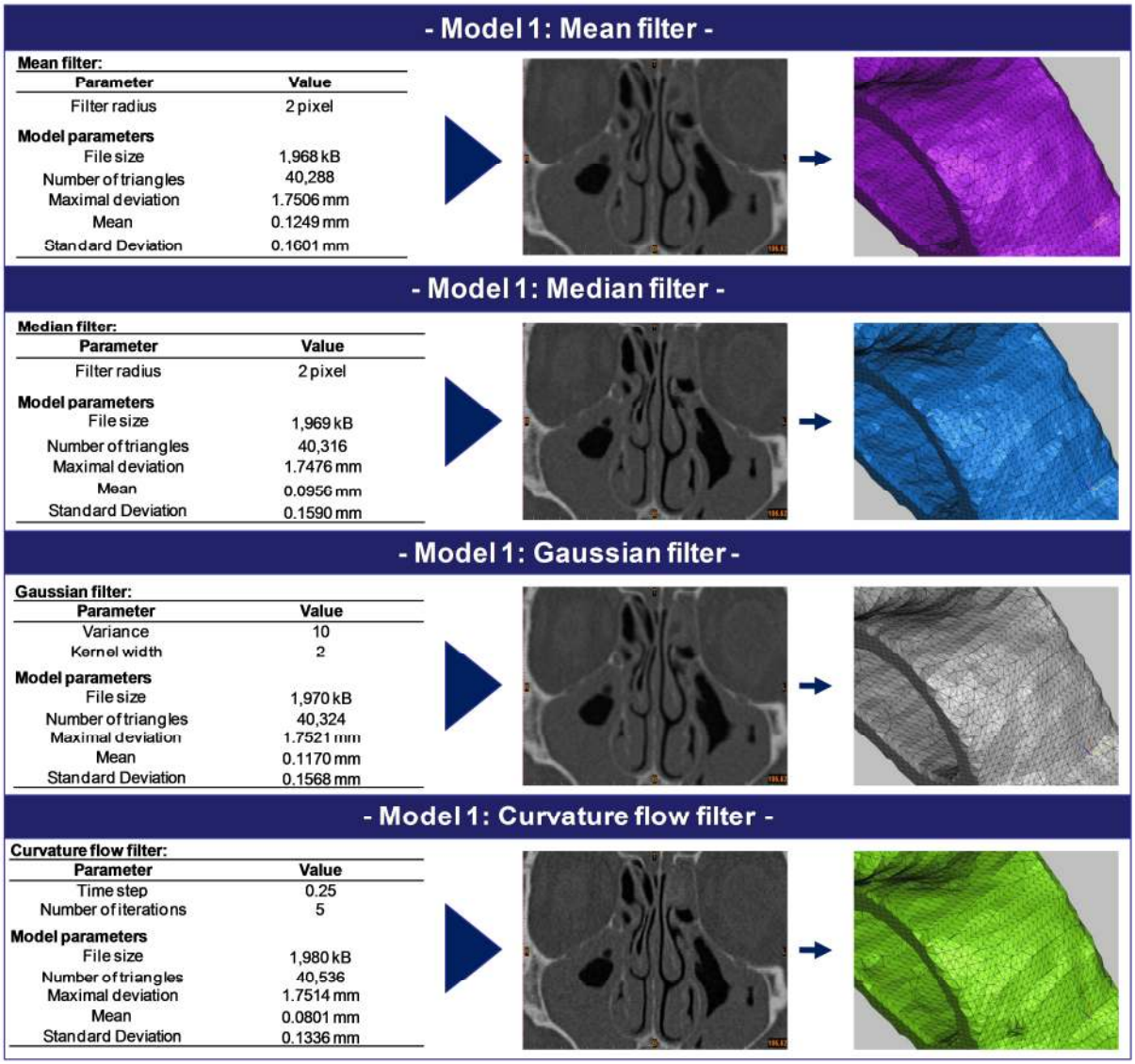

Figure 5-2: Filter results model 1

None of the filters is able to avoid a maximum model deviation of 1.75 mm. Observing the variance of the number of triangles in final models reveals that the number of triangles is reduced in all cases (e.g., from 45,352 to approx. 40,536 triangles using curvature flow). The implication is that fewer triangles are generated in the final mesh after applying the noise reduction filters. The curvature flow filter leads to the highest number of triangles (40,536). This might be a consequence of the filter's superior ability to preserve complex features, in that more triangles can be used for building the triangulated model.

The filtering results of model 2 show similar effects as depicted in Figure 5-3. The noise reduction results of model 2 show again that the curvature flow filter offers the best final model accuracy. Even narrowed regions with boundaries that tend to blur are preserved. The results of both measurement series suggest that the CT internal reconstruction filter has an impact on accuracy.

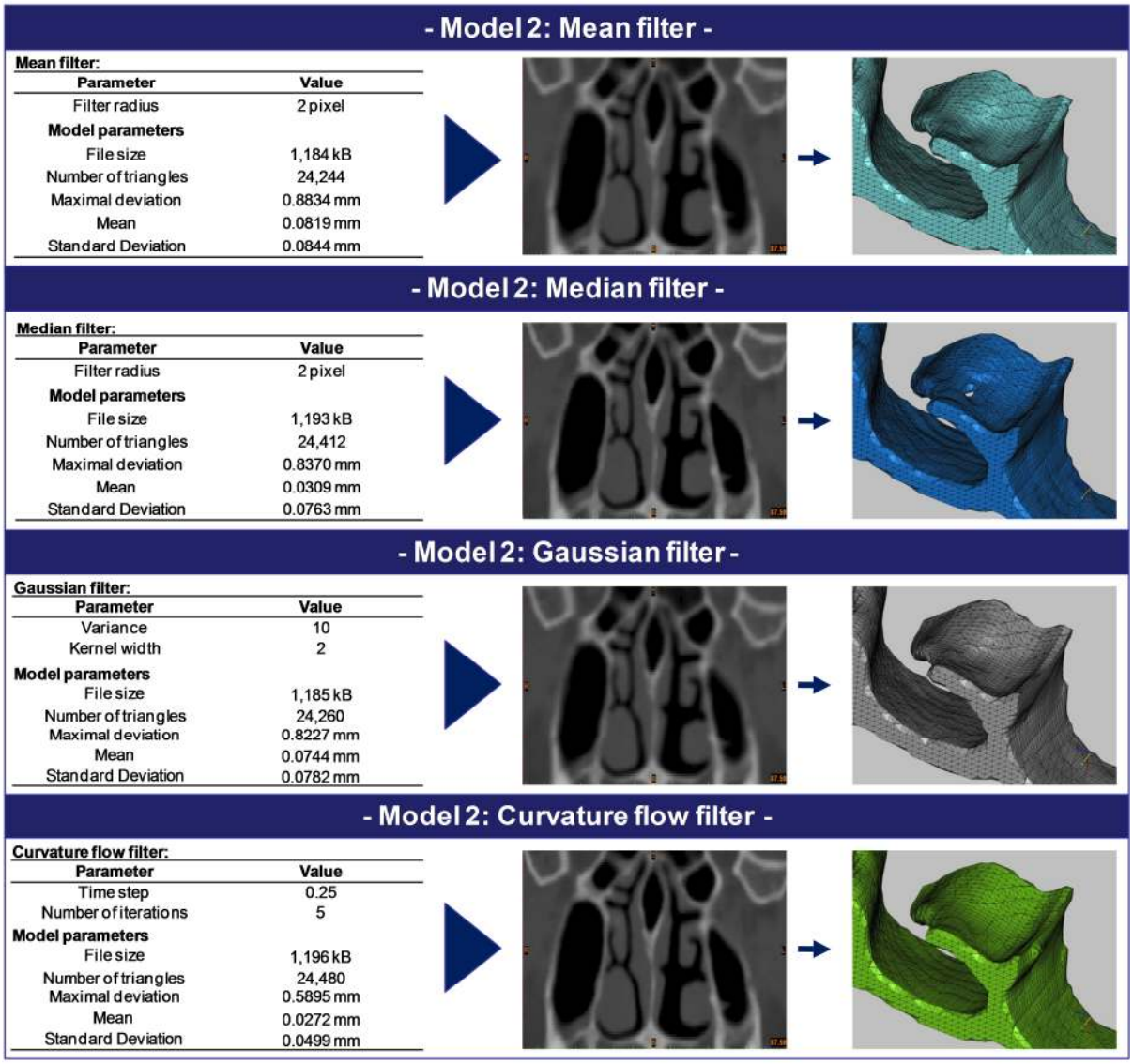

Figure 5-3: Filter results model 2

Comparing the model deviations of models 1 and 2, the curvature flow results show that model 1 has a mean deviation of 0.0801 mm and model 2 of 0.0272 mm. This yields a difference in mean deviation of 0.0529 mm. This difference reveals that the H50s filter is the more appropriate internal CT reconstruction filter.

A disadvantage of the curvature flow filter is that larger stair-step artifacts cannot be smoothed. This may be based on the curvature flow principle: regions with an equal radius of curvature should not be manipulated (Chapter 2.1.3). Compared to the mean, median, and Gaussian filter, the curvature flow filter leads to less-deviated models. The reason for this might be based on the fact that the level of smoothing is not related to a nearby region, but rather to the amount of curvature. Visual examination supports the measurement results that the final .STL mesh of model 2 is smoother and more evenly generated than that of model 1. Therefore, the curvature flow filter is used for the following analysis of medical model accuracy.

5.2 Model accuracy

The task of generating accurate medical RP models can be assisted by analyses that reveal potential inaccuracies, which may arise during medical model generation (Fig. 4-5). Specifically, measurement studies verify the demands on CT scans made by prototyping, by using a physical test model. The virtual test model is an .STL model generated from a 3D CAD model. The physical RP model is made of PMMA, which is material typically used for medical RP models (Hieu et al., 2005; Azmi et al., 2004). As shown in Figure 5-4 the test model has a defined geometry: a square block with a free-form contour.

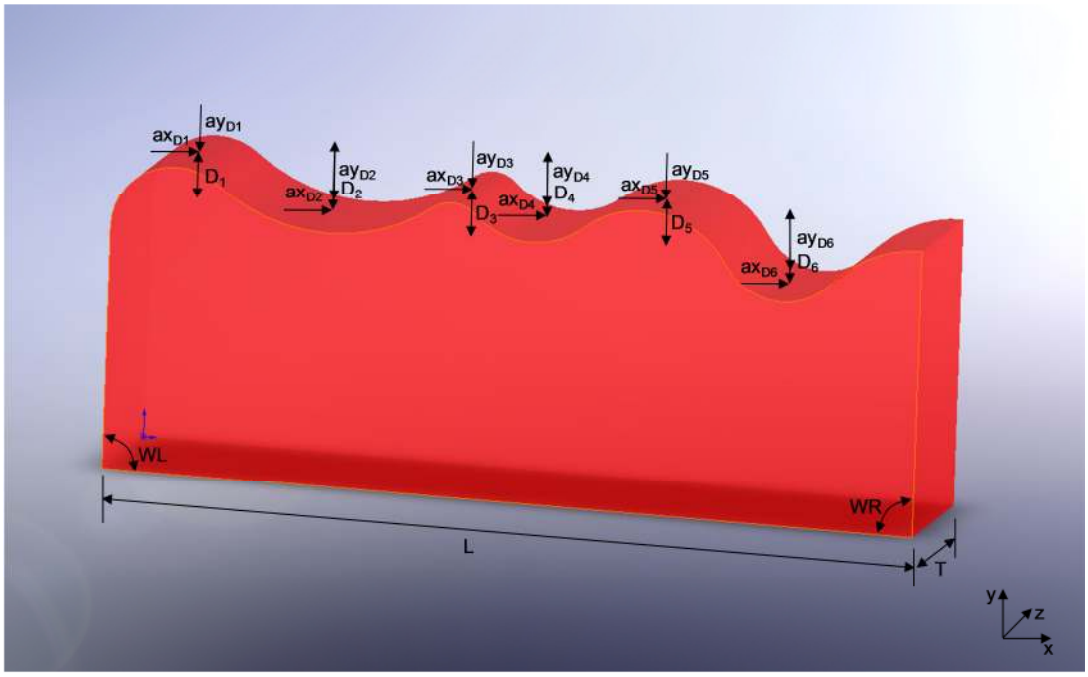

Figure 5-4: Test model

The test model has the advantage of having an evenly distributed density of 1.18 g/cm^3 (PMMA), which then provides a more exact threshold setting in the segmentation process. The design of the test model is depicted in Figure 5-4. The test model also has the advantage that the geometry features an exactly defined 2D contour, which can be sufficiently segmented, milled, and measured using a coordinate measurement machine (CMM). In addition, the geometry represents an exemplary contour that is typically processed in medical radiology. The accuracy analysis is processed two times in order to compare the influence of different CT scanners, and is based on the following test sequence (Fig. 5-5): First, the test model is defined using the 3D CAD software SolidWorks Version 2007. Here, the original measures are set and verified. Then, after the .STL reference test model has been milled using the CAM software, CamWorks Version 2007 (Teksoft) and the milling machine BAZ 15 (Alzmetall, Heidenhain control system), the reference test model is put in the CT imaging machine, Somatom Definition (Siemens; 1 slice per rotation) (Single-slice

scanner study). In the second multislice scanner study, the test model is scanned in the multislice technology CT scanner, Sensation Open (Siemens) (40 slices per rotation).

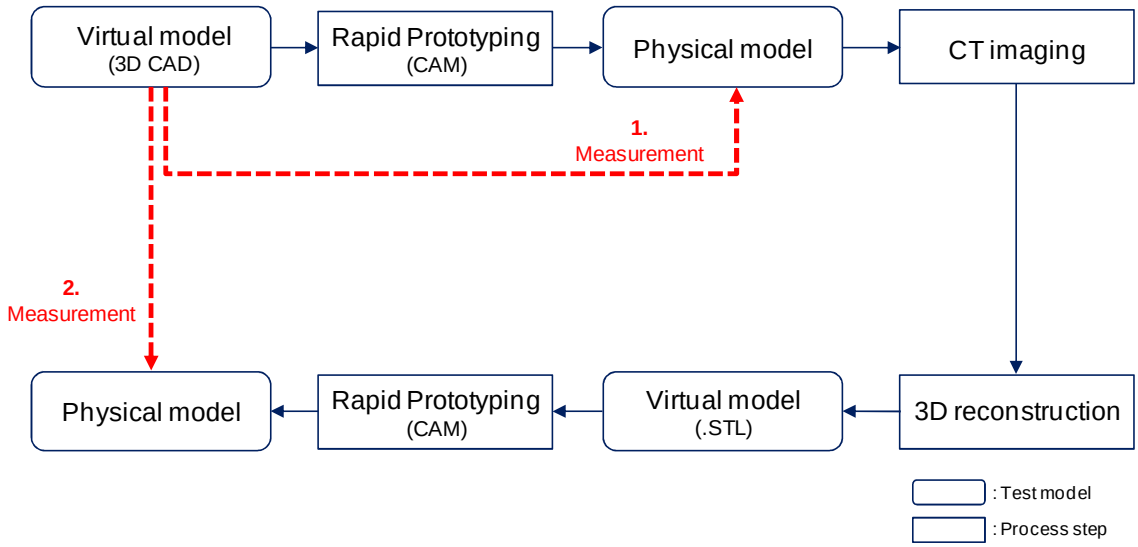

Figure 5-5: Test sequence accuracy analysis

In both studies, different settings of the scan parameters are evaluated to identify possible effects on accuracy. In some cases in the second multislice scanner study, the scanning direction is varied from longitudinal to transverse in order to analyze the possible impact of the initial scanning direction. The scan protocol used is presented in Table 5-2:

Table 5-2: Scan prototocol accuracy analyis

Scan parameters: Single-slice scanner study		**Scan parameters: Multislice scanner study**	
Scanner	Siemens SOMATOM PLUS 4	Scanner	Siemens SENSATION OPEN
Reconstruction-Algorithm	H50s	Reconstruction-Algorithm	H50s
Slice increment slice thickness	→ *Table 5-4, Table 5-5*	Slice increment slice thickness	→ *Table 5-6, Table 5-7*
Hounsfield unit spectrum	-724 → +574	Hounsfield unit spectrum	-530 → +1024

The selection of scan parameters (Table 5-2) depends on predefined clinical data calibrations provided from the used CT scanners (Alfried Krupp von Bohlen und Halbach Hospital (Radiology, Dr. M. Montag)). As stated in Table 5-2, the Hounsfield unit spectrum used for the subsequent segmentation process is fixed to reduce the user's influence on segmentation accuracy. The output is a set of .DICOM files that have been imported into the 3D reconstruction software, Mimics Version 10, to generate .STL models. All .STL models are exported in full resolution without any intervention in the triangulated mesh to avoid any additional influence on accuracy. The reconstructed models are imported again into CamWorks to program machine code for milling. Finally, a set of physical test models is milled and measured to state the final deviation of reconstructed medical RP models.

As depicted in Figure 5-5, the test model is measured during the presented sequence in two measurements. The first measurement states the deviation that occurs during the milling process and uses a coordinate measurement machine (CMM) that takes into account the measuring points (see Fig. 5-4). In terms ensuring final accuracy, the CMM measures 23 points and makes six iterations per measurement (Table 5-3), to increase accuracy with a reasonable expenditure for measuring. The six measurement values for every point are used to calculate the arithmetic mean value (μ). Mean deviations of the 23 measuring points are then compared with the reference values of the original CAD model. The maximum outer dimensions of the test model are 100 mm in length, 18 mm in depth, and 38 mm in height. The wave contour is built on six different half-circles ($D_1 \ldots D_6$) positioned from $ax_{D1}/ay_{D1}, \ldots, ax_{D6}/ay_{D6}$, as shown in Table 5-3:

Table 5-3: Reference measures: test model accuracy analysis

Aggregated measurement points	Marking (Figure 5-4)	Reference measures [mm]
Centre of circles in x-direction (ax_{Di})	axD1	8
	axD2	26.65
	axD3	41.98
	axD4	51.78
	axD5	65.74
	axD6	82.86
Centre of circles in y-direction (ay_{Di})	ayD1	29.5
	ayD2	53
	ayD3	32
	ayD4	42
	ayD5	25
	ayD6	35.34
Length (L)	L	100
Radiuses (D_i)	D1	16
	D2	44
	D3	8
	D4	20
	D5	24
	D6	16
	D7	30
Angles (W_i)	WL	90
	WR	90
Thickness (T)	T	18

The second measurement records the deviation of the reconstructed RP model using the CMM to guarantee a valid result. Additionally, final mean deviations (μ) are aggregated with reference to the geometrical characteristics of the test model in order to detect which geometrical characteristic deviates more and which less (Table 5-3). The standard deviation (σ) is calculated to show the distribution of the six-times-measured mean values with a two-sided 95 % confidence interval (DIN 1319-3).

5.2.1 Single-slice scanner study

The measurement series shows a mean deviation of the original RP process of 0.063 mm. Results of the study shows a lowest mean deviation of 0.553 mm for case number 2, for which a slice increment of 1 mm and a slice thickness of 2.5 mm have been used for scanning. Considering the accuracy after 3D reconstruction at measurement two, it can be seen that slice increment has the most impact on accuracy (Table 5-4). In case 7, a deviation of 7.049 mm results, although typical clinical scan parameters have been used.

Table 5-4: Measurement results single-slice scanner study

Number	Test model (Model_"slice increment"/"slice thickness")	1. Measurement (Milled reference model) mean [mm]	2. Measurement (Milled reconstructed model) mean [mm]
1	Model_Ref	0.063	
2	Model_1/2.5		0.553
3	Model_1/3		0.728
4	Model_2/2		1.025
5	Model_2/4		0.545
6	Model_3/3		1.041
7	Model_5/5		7.049

Highest deviation
Lowest deviation

The source of deviations is given in Table 5-5. It can be seen that the radiuses are more deviated when a the higher slice increment and slice thickness are selected. Spread also increases when a higher slice increment and slice thickness are selected.

Table 5-5: Results single-slice scanner study: aggregated measurement points

	Test models	Centre of circle x-direction (ax_{Di}) [mm]	Centre of circle y-direction (ay_{Di}) [mm]	Length (L) [mm]	Radius (D_i) [mm]	Angle (W_i) [°]
1	**Mean (μ) reference model**	**0.021**	**0.061**	**0.125**	**0.039**	**0.064**
	Standard deviation (σ 95,00 ±)	0.009	0.036	0.000	0.05	0.007
2	**Mean (μ) model_1/2.5**	**0.861**	**0.256**	**1.035**	**0.506**	**0.107**
	Standard deviation (σ 95,00 ±)	0.064	0.326	0.005	0.603	0.033
3	**Mean (μ) model_1/3**	**0.163**	**0.814**	**0.379**	**1.928**	**0.355**
	Standard deviation (σ 95,00 ±)	0.156	0.571	0.104	1.012	0.093
4	**Mean (μ) model_2/2**	**1.773**	**0.312**	**1.975**	**0.951**	**0.113**
	Standard deviation (σ 95,00 ±)	0.126	0.381	0.050	0.710	0.088
5	**Mean (μ) model_2/4**	**0.857**	**0.491**	**0.022**	**1.270**	**0.086**
	Standard deviation (σ 95,00 ±)	0.106	0.231	0.102	1.188	0.106
6	**Mean (μ) model_3/3**	**0.239**	**0.811**	**0.920**	**3.151**	**0.086**
	Standard deviation (σ 95,00 ±)	0.222	1.323	0.045	1.768	0.062
7	**Mean (μ) model_5/5**	**3.139**	**9.602**	**4.809**	**17.597**	**0.098**
	Standard deviation (σ 95,00 ±)	1.716	9.602	0.019	23.472	0.049

Highest deviation
Lowest deviation

In case 7, a standard deviation of 23.472 mm is given for the radius measurement.

A visual comparison (Fig. 5-6) of the best case (Test model 2, see Table 5-5) and worst case (Test model 7, see Table 5-5) supports the results of Table 5-5.

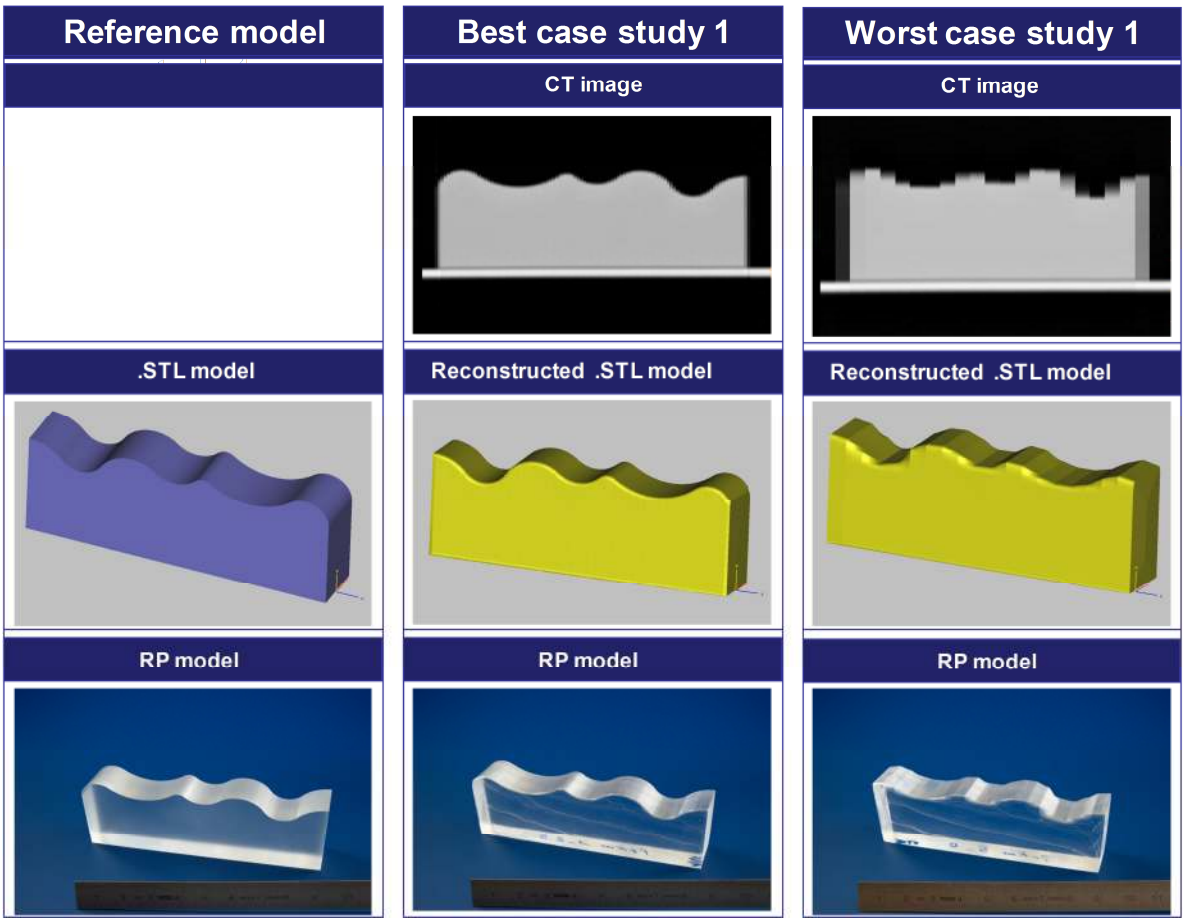

Figure 5-6: Models single-slice scanner study

The CT image of the worst case scenario show unclear boundaries. In contrast, the radii in particular are much better represented in the best case (2).

5.2.2 Multi-slice scanner study

The result of measurement case two shows a lowest mean deviation of 0.380 mm for case number 2, for which a slice increment of 0.6 mm and a slice thickness of 0.1 mm have been used for scanning. Considering the accuracy after 3D reconstruction at measurement two, it can be seen that slice increment has the most impact on accuracy (Table 5-6). In case 7, scanning direction has been changed to transverse. As a consequence, accuracy is much better than for the same parameters, whereby scanning direction is normally orientated in the longitudinal direction (6). A comparison of cases 6 and 7 shows an improvement of 0.27 mm, which is created simply by a change in scanning direction. The analysis of cases 10 and 11

shows the same effect with an improvement of 2.36 mm. In case 12, the highest mean deviation of 3.251 mm is found.

Table 5-6: Measurement results multislice scanner study

Number	Test model (Model_"slice increment"/"slice thickness")	1. Measurement (Milled reference model) mean [mm]	2. Measurement (Milled reconstructed model) mean [mm]
1	Reference model	0.063	
2	Model_0.6/0.1		0.380
3	Model_0.6/0.4		0.426
4	Model_0.6/0.6		0.440
5	Model_0.6/1		0.553
6	Model_1/1		0.544
7	Model_1/1 (transverse)		0.274
8	Model_2/2 (transverse)		0.393
9	Model_3/1		0.527
10	Model_3/3		2.656
11	Model_3/3 (transverse)		0.293
12	Model_3/5		3.251
13	Model_4/2		2.460
14	Model_4/4		2.431
15	Model_5/5		1.873
			Highest deviation
			Lowest deviation

The reasons why the deviations occurred are shown in Table 5-7 can be seen that a higher slice increment causes a higher level of contour approximation. The larger the distance that is selected between each slice, the less information the MC algorithm has for producing an accurate meshing. The radii are most influenced by larger slice increments, as demonstrated, for example, by case 12, in which standard deviation amounts to 18.294 mm. Again, accuracy is much better if the model is scanned in the transverse direction. A comparison of cases 10 and 11 shows an improvement of 4.29 mm if the model is scanned in the transverse direction. But, one must note that model thickness deviates concurrently when the model is scanned in the transverse direction. Measurement results of case 11 demonstrate this observation. Although values of centre points in the x-direction, lengths, and radii show the best results, thickness is worst with a value of 2.521 mm.

Table 5-7: Measurement results multislice scanner study: aggregated measurement points

	Test models	Centre of circle x-direction (ax_{Di}) [mm]	Centre of circle y-direction (ay_{Di}) [mm]	Length (L) [mm]	Radius (D_i) [mm]	Angle (W_i) [°]	Thickness (T) [mm]
1	**Mean (μ) reference model**	**0.021**	**0.061**	**0.125**	**0.039**	**0.064**	**0.046**
	Standard deviation (σ 95,00 ±)	0.009	0.036	0.000	0.050	0.007	0.018
2	**Mean (μ) model_0.6/0.1**	**0.142**	**0.254**	**0.199**	**0.736**	**0.567**	**0.515**
	Standard deviation (σ 95,00 ±)	0.063	0.231	0.008	0.471	0.042	0.151
3	**Mean (μ) model_0.6/0.4**	**0.443**	**0.280**	**0.715**	**0.639**	**0.051**	**0.471**
	Standard deviation (σ 95,00 ±)	0.12	0.228	0.062	0.638	0.085	0.164
4	**Mean (μ) model_0.6/0.6**	**0.466**	**0.244**	**0.942**	**0.518**	**0.032**	**0.42**
	Standard deviation (σ 95,00 ±)	0.086	0.327	0.010	0.715	0.008	0.107
5	**Mean (μ) model_0.6/1**	**0.861**	**0.256**	**1.035**	**0.506**	**0.107**	**0.429**
	Standard deviation (σ 95,00 ±)	0.139	0.230	0.104	0.492	0.119	0.166
6	**Mean (μ) model_1/1**	**0.634**	**0.322**	**0.904**	**0.817**	**0.044**	**0.572**
	Standard deviation (σ 95,00 ±)	0.083	0.282	0.004	0.683	0.051	0.109
7	**Mean (μ) model_1/1 (transvers**	**0.105**	**0.467**	**0.024**	**0.537**	**0.238**	**0.562**
	Standard deviation (σ 95,00 ±)	0.081	0.251	0.053	0.534	0.068	0.066
8	**Mean (μ) model_2/2 (transvers**	**0.101**	**0.639**	**0.082**	**0.808**	**0.333**	**1.405**
	Standard deviation (σ 95,00 ±)	0.100	0.277	0.005	0.542	0.031	0.092
9	**Mean (μ) model_3/1**	**0.629**	**0.285**	**0.874**	**0.795**	**0.053**	**0.481**
	Standard deviation (σ 95,00 ±)	0.072	0.353	0.034	0.603	0.04	0.138
10	**Mean (μ) model_3/3**	**1.632**	**3.065**	**3.790**	**4.744**	**0.047**	**0.422**
	Standard deviation (σ 95,00 ±)	1.081	5.153	0.018	11.917	0.063	0.089
11	**Mean (μ) model_3/3 (transvers**	**0.052**	**0.614**	**0.059**	**0.447**	**0.291**	**2.521**
	Standard deviation (σ 95,00 ±)	0.083	0.520	0.012	0.854	0.044	0.274
12	**Mean (μ) model_3/5**	**2.070**	**1.239**	**4.670**	**8.159**	**0.118**	**0.364**
	Standard deviation (σ 95,00 ±)	4.462	13.679	0.058	18.294	0.213	0.103
13	**Mean (μ) model_4/2**	**1.705**	**5.445**	**1.818**	**3.247**	**0.087**	**0.336**
	Standard deviation (σ 95,00 ±)	0.136	1.108	0.039	2.829	0.058	0.074
14	**Mean (μ) model_4/4**	**2.561**	**1.540**	**3.760**	**4.223**	**0.069**	**0.431**
	Standard deviation (σ 95,00 ±)	2.222	6.005	0.091	11.542	0.096	0.109
15	**Mean (μ) model_5/5**	**0.519**	**1.515**	**4.863**	**2.43**	**0.036**	**0.615**
	Standard deviation (σ 95,00 ±)	1.084	2.531	0.013	5.925	0.032	0.186

Highest deviation

Lowest deviation

A visual comparison (Fig. 5-7) of best (2) and worst case (12) scenarios substantiates the results of Table 5-7. The CT images of the worst case (12) present washy boundaries. In particular, the radii are much better represented in the best case (2).

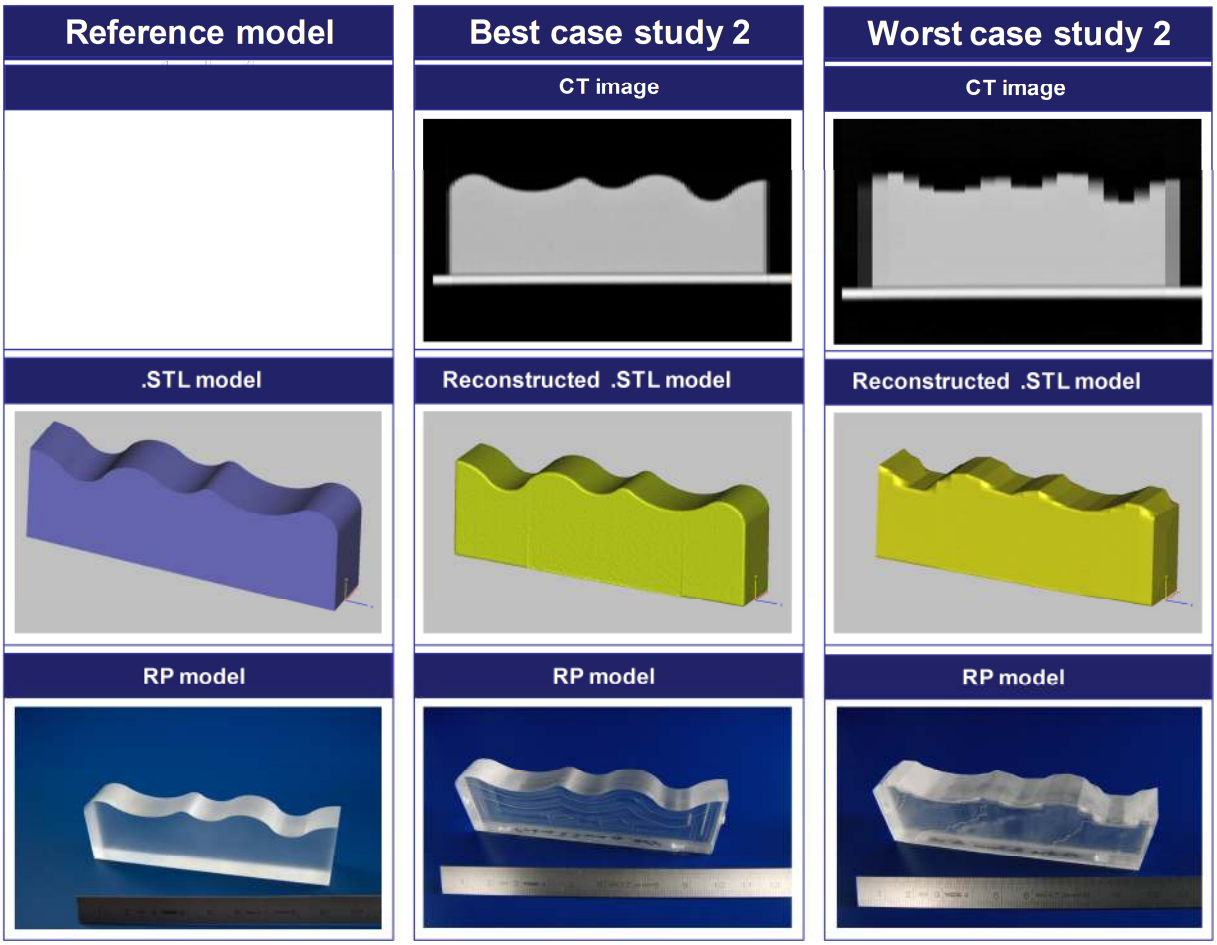

Figure 5-7: Models multislice scanner study

When comparing both measurement studies, it is obvious that the multislice scanner study uncovered more detailed findings about the influence of scanning parameters on accuracy.

5.2.3 Conclusion

The success of the 3D reconstruction process depends on how easy it is to eliminate inaccuracies caused by nonoptimally chosen scan parameters. The measurement studies have shown how a higher slice increment causes a larger distance between each slice. The consequence is that possible deviations are great, and results are thus distant from original measurements. Slice images converted to a 3D model cannot represent exact geometry in the case of nonoptimal resolution in the z-direction. This can be overcome and optimized by taking small slice increments.

CNC milling fulfills needs of manufacturing medical models by allowing inaccuracies of ± 1 mm (Klein and Broeckel, 2005) with a resulting mean deviation of 0.380 mm. This is accomplished by using scan parameters of 0.1 mm for slice increment and 0.6 mm for slice thickness for scanning the test model in the longitudinal direction. The RP process has a

mean deviation of 0.063 mm, largely due to the 3D reconstruction process. The smallest selected scan parameters of a slice thickness of 0.6 mm and a slice increment of 0.1 mm lead to a reconstruction error of 0.31 mm. This failure cannot be eliminated by a more suitable manufacturing method but can be by a better scanning procedure. The transverse-scanned test model in the multislice scanner study (case 7) shows a lowest mean deviation of 0.274 mm. This measured deviation represents an increase of 0.72 mm when compared to the optimum demanded by Klein and Broeckel (2005). Compared to the study of Choi et al. (2002) in which they produced a thus far unachieved result by generating a skull RP model with only 0.62 mm mean deviation, the present result is an improvement of 0.34 mm (54 %). A comparison of both measurement studies shows an optimization in the multislice scanner study series of 0.17 mm using a slice increment of 0.6 mm and slice thickness of 0.1 mm instead the a slice increment of 1 mm and slice thickness of 2.5 mm.

In case 2 of the second multislice scanner study, the angle measurement shows the highest mean deviation of 0.567 mm compared to other cases of the second measurement study although a slice increment of 0.6 mm and a slice thickness of 0.1 mm is selected. The reason for this is demonstrated by false color images shown in Figure 5-8.

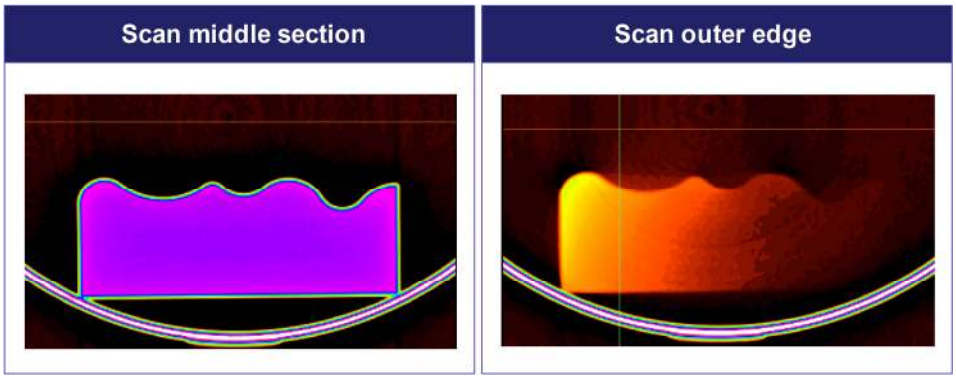

Figure 5-8: False color image measurement study 2, case 2

As demonstrated by Figure 5-8, the outer edge of the side surface is not captured in full. The reason for this is the form of the thin slice profile (Chapter 2.1.2.2). Although the position of the test model is calibrated using the laser positioning system of the CT scanner, the side surface deviates by a fraction of a degree. In case 2, the slice thickness is only 0.1 mm so that one reason might be that a small deviation of the test model's longitudinal position cannot capture the complete outer slice. A second reason can be attributed to the fact that in the other cases shown, higher slice thickness might lead to the situation where the profile slice error is less influencing (Chapter 2.1.2.2); thus, the rounding of the slice profile influences the longitudinal side surface deviation to an extent. This is based on the unavoidable spiral movement of the tomographic scanning unit. In consequence, the slice thickness should be set ≤0.4 mm (Table 5-7). Finally, there is evidence that the shape of the

slice profile is relevant to accurate model generation. It is noteworthy that no previous study found the influence of the slice profile form on RP model accuracy.

Nevertheless, slice spacing is critical for 3D model reconstruction and determines spatial accuracy. Accuracy in the third dimension (z-axis) is determined by the slice increment and should be set at a minimum, i.e., less than the size of the smallest feature intended for reconstruction. In general, slice increment should be as small as possible, from a technical point of view, to provide the MC algorithm with as much information as possible for generating the surface mesh. The more information that is scanned, the more vertices the MC algorithm can set. A high number of vertices lead to small distances between the vertices. Short distances between the vertices permit shorter edges to be generated and the original contour can be reconstructed much better. Taking into account the present results, it can be stated that the RP process alone does not lead to inaccuracy, but that scanning parameters are the basic cause. In a study by Mallepree & Bergers (2008), it was shown that the accuracy of medical RP models is determined by the medical imaging system.

However, the results of the RP process shown cannot be applied to every medical case. Still, it can be stated that the 3D reconstruction parameters of slice thickness and slice increment should be considered carefully when generating medical models with sufficient accuracy. As demonstrated by the medical prototyping accuracy matrix (Fig. 5-9), accuracy, the ratio of slice thickness and slice increment (pitch), and the selected medical prototyping application, are all interdependent.

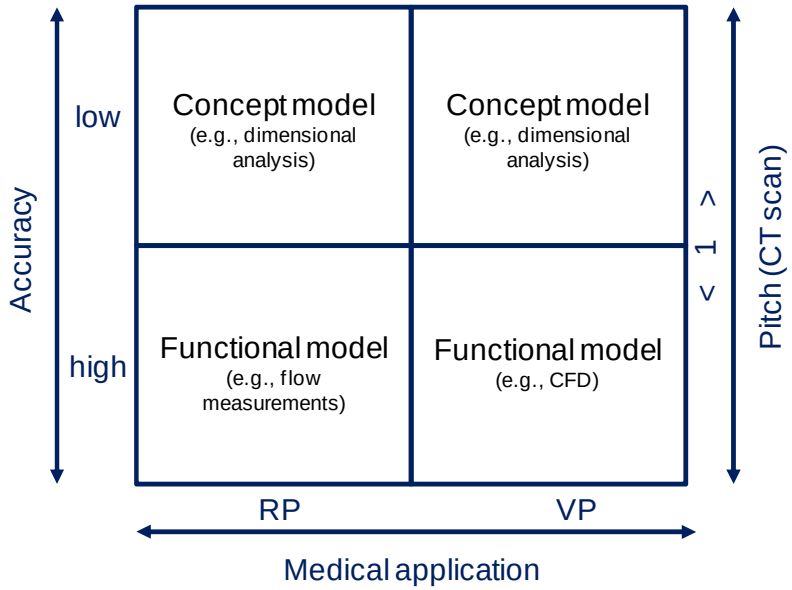

Figure 5-9: Medical prototyping accuracy matrix

A pitch >1 should be selected if the medical application necessitates concept models only, both for VP and RP. If however, there is a need for functional models, accuracy is optimized with a pitch <1, both for VP and RP.

The present findings are followed by an investigation of mesh enhancement during 3D reconstruction. This is done to improve virtual (.STL) model accuracy even though the basic source of error is the scan process.

5.3 Surface mesh analysis

A generated surface mesh is a necessary precondition when transferring scanned image data from 3D reconstruction to post-processing applications such as VP and RP. The 3D reconstruction process allows defining the final surface mesh quality, which relates to model accuracy.

When generating a triangulated surface mesh (the following investigations on surface mesh quality refer to the .STL data format (Chapter 2.2.3), the objective is to balance accuracy and computing time, which is dependent on file size. This is realized by setting a permissible deviation between the original model's surface and the approximated triangular mesh, when generating the mesh with the MC algorithm (Chapter 2.1.4.1). When processing medical models, the original model surface is the surface that is built on all available gray values. Therefore, all available gray values should be used to obtain an .STL model with highest resolution to avoid an unnecessary loss of information. A generated surface mesh can contain defects that can influence a model's final accuracy. Typical errors are incorrect normal vectors or gaps between triangles. Software tools are available that can efficiently repair possible defects in automatic operation mode (e.g., 3-Matic). Therefore, possible defects are not focused upon in the present thesis but rather actual mesh building; this refers to applied mesh-editing parameters of triangle reduction and smoothing discussed in Chapter 2.1.6 (Table 2-2). The objective herein, is to determine decisive parameters for generating a surface mesh representative of a medical model that is most similar to an original model, whereby the original model is built of gray values only. Thus, all available gray values must be processed and an optimum range of surface smoothing found, due to the reconstructed angular structures caused by the MC algorithm. Otherwise, the degree of model accuracy decreases.

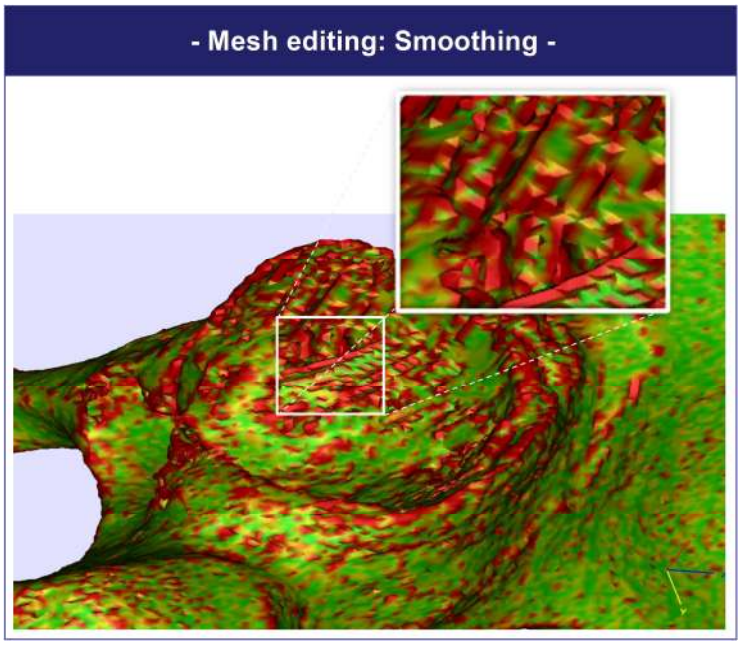

Figure 5-10: Smoothing of angular mesh structures

As depicted in Figure 5-10, angular and brick-shaped mesh structures often appear after 3D reconstruction. These specific structures have a technical and not a native origin. Therefore, smoothing is required to optimize the mesh. Only in cases where file sizes are larger than 35 MB (2Ghz Dual-core, 4GB RAM, 32 bit Windows PC), does file size need to be reduced. Especially, in running post-processing applications (e.g., model slicing), models larger than 35 MB overload a computer's processing system. In this case, smoothing combined with triangle reduction need to be conducted.

A primitive model measurement begins with an evaluation of the influential mesh editing parameters of triangle reduction and smoothing, respectively (Fig. 5-13). The primitive models (cube, tetrahedron, cylinder, sphere) are generated in the 3D CAD system SolidWorks 2009 and derived as reference .STL files. Possible deviations between the reference primitive models and edited (triangle reduction, smoothing) primitive models are investigated. Then, an analysis of aggregated mesh editing parameters is conducted, based on the results from the individual parameter analysis.
A medical model measurement uses three reference medical models (i.e., femur, hip, nose) to verify the extracted aggregated parameters from the first measurement of the primitive models (Fig. 5-11).

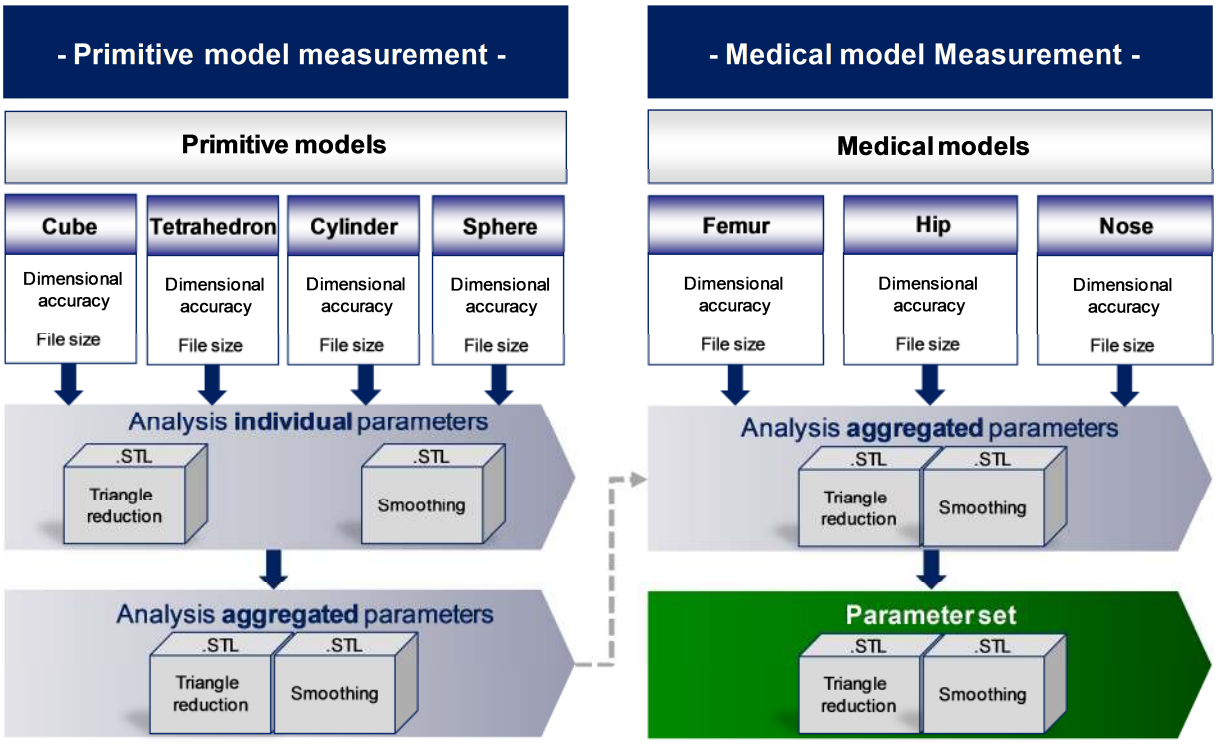

Figure 5-11: STL Editing test sequence

Possible differences between the reference medical models, which are generated by means of the MC algorithm and the edited medical models, are again analyzed. The medical models used are reconstructed from CT images, which result from predefined clinical data sets provided from the Alfried Krupp von Bohlen und Halbach Hospital (Radiology, Dr. M. Montag) (Table 5-9).

Table 5-9: Scan parameters: medical models meshing analysis

Parameter	Femur	Hip	Nose
Scanner	Siemens SENSATION 16	Philips Brilliance 16	Siemens SENSATION OPEN
Reconstruction filter	B30f	D	H50s
Slice increment	1 [mm]	2 [mm]	0.5 [mm]
Slice thickness	2 mm [mm]	2 mm [mm]	0.5 mm [mm]
Resolution	512×512 [pixel]	512×512 [pixel]	512×512 [pixel]
Pixel size	0.576 [mm]	0.729 [mm]	0.342 [mm]
Field of view	29.5 [cm²]	37.3 [cm²]	17.5 [cm²]

Three different types of CT scanners, different slice increments, and slice thicknesses have been used to create three typical scenarios found daily in clinical routine.

Differences between reference models that are generated in full resolution and those that are edited .STL models are analytically measured (3-Matic) two-fold.
First, dimensional accuracy and file size is compared between edited primitive models and their original reference models (Fig. 5-12). The four primitive reference models are generated analytically by means of a 3D CAD system (SolidWorks 2009).

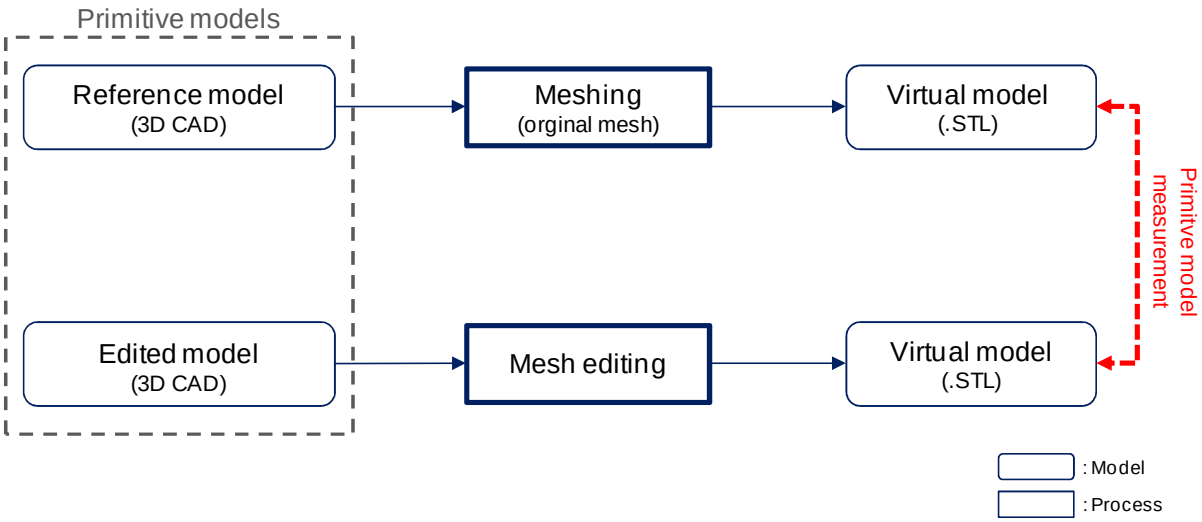

Figure 5-12: Primitive model measurement

The primitive model measurement aims to compare the deviation of the edited mesh of the manipulated virtual .STL model to the original mesh of the appropriate reference model (Fig. 5-12).

Secondly, the dimensional accuracy and file size between three reconstructed and edited medical models is compared to their original reference in full resolution.

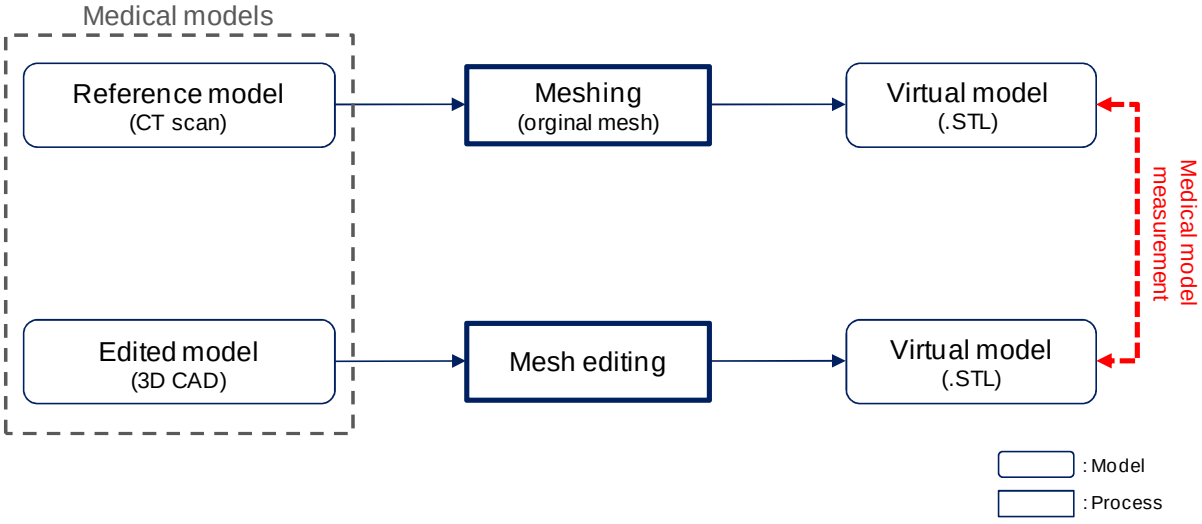

Figure 5-13: Medical model measurement

The medical model measurement states the deviation of the edited surface of the medical models to the original mesh, from the reference medical models. As demonstrated in Figures 5-12 and 5-13, both primitive reference models and medical reference models are reconstructed without manipulating the surface mesh (original mesh). The resulting mesh is the original mesh generated by means of the MC algorithm (Chapter 2.1.4.1). A modification is not applied on this resulting mesh. The measurement result reveals the influence of how different mesh editing parameters contribute to 3D model reconstruction. In order to compare

possible deviations between the original and edited meshes, the four primitive reference models are transferred into a 3D reconstruction environment (Mimics) first. The analytically built primitive models consist of surface meshes generated by means of the 3D CAD system SolidWorks 2009. To obtain models with surface meshes that are generated by means of the MC algorithm, the primitive models need to be processed in the 3D reconstruction system Mimics. The reconstruction settings are given in Table 5-8.

Table 5-8: Parameter settings reconstruction environment

Parameter	Value
Scanner	Siemens SENSATION OPEN
Reconstruction filter	H50s
Slice increment	0.5 [mm]
Slice thickness	0.5 mm [mm]
Resolution	512×512 [pixel]
Pixel size	0.342 [mm]
Field of view	17.5 [cm²]

In the following, a set of parameters for meshing in prototyping will be determined as settings for typical 3D reconstruction cases of medical models

5.3.1 Primitive model measurement

The primitive model measurement shows that both tolerance and edge angle can be selected as minimum values (Table 5-10). A tolerance of 0.1 mm and an edge angle of 1° allows a reduction in file size while maintaining an acceptable mean error rate. For instance, the mean error of the cylinder is 0.0002 mm with a tolerance of 0.1 mm, edge angle of 1° and 10 iterations. If an edge angle of 15° is selected, the tolerance value of 0.1 mm leads to sufficient results as depicted by Figure 5-14.

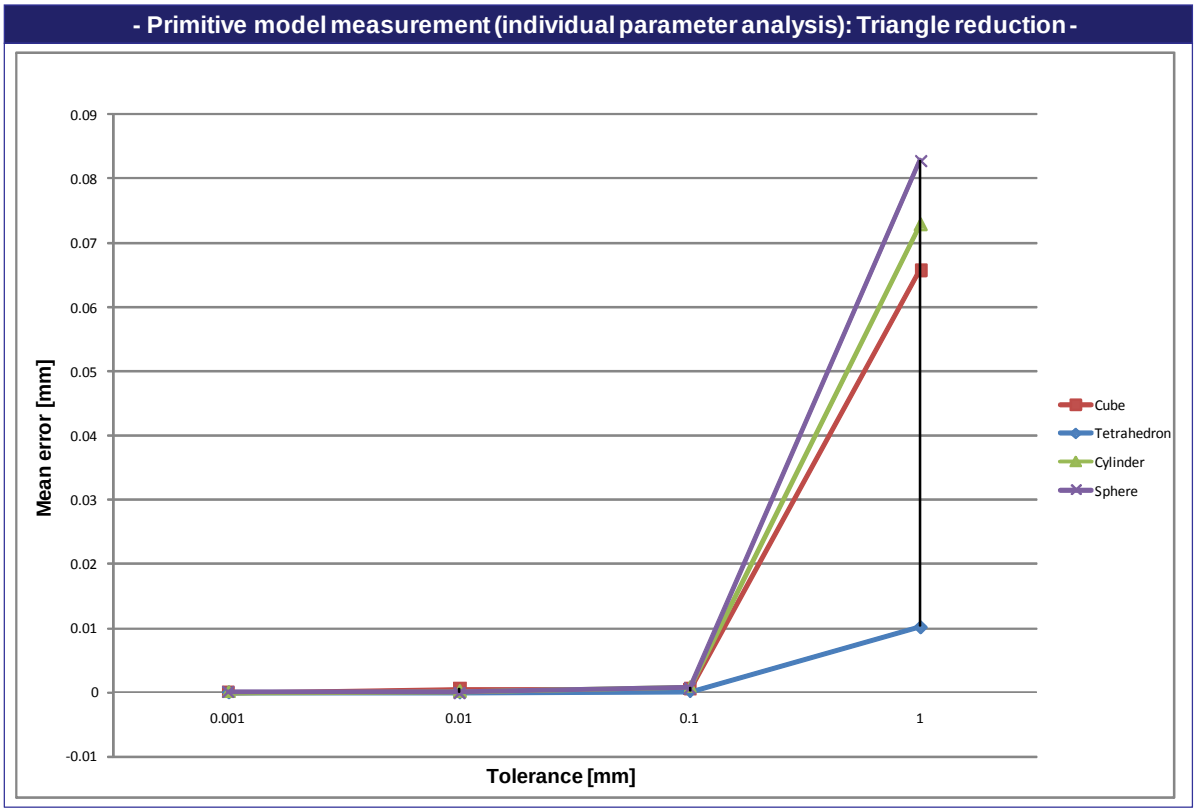

Figure 5-14: Primitive model measurement (individual parameter analysis): tolerance

The effects of edge angle manipulation are linked to tolerance. When varying the edge angle with a tolerance < 0.1 mm, no dimensional deviations can be detected. If a tolerance factor of >0.1 mm is selected, edge angle does influence model accuracy.

Table 5-10: Primitive model measurement: individual parameters

Parameter	Range of values	Result
Triangle reduction		
Tolerance	0.01 - 0.2 [mm]	0.1 mm is ideally suited → Higher values increase mean error
Edge Angle	1 - 30 [°]	1° is ideally suited → Higher values increase mean error
Iterations	1 – 20	5 iterations are ideally suited → Higher values increase mean error; file size is not reduced further
Mode	Point, Edge, Advanced Edge	Advance Edge is ideally suited → Other modes increase mean error and reduce file size less
Smoothing		
Iterations	1 – 20	5 - 10 are ideally suited → Lower values than 5 reduce noise not enough even though high factors are used; values higher than 10 increase mean error
Factor	0.01 – 1	0.5 is ideally suited → Lower values reduce noise not enough; higher values increase mean error

When conducting tolerance and edge angle editing, the variation of possible iterations reveals that five iterations are ideally suited. Higher values increase the mean error and do not reduce file size.

Smoothing influences model accuracy as well. The comparative test of use of the different smoothing factors with five iterations reveals that the higher the smoothing factor is selected, the more the models are influenced by smoothing (Fig. 5-15). A factor of 0.5 is ideally suited for smoothing. Factors higher than 0.5 lead to an increase of mean error. Lower values do not reduce noise sufficiently.

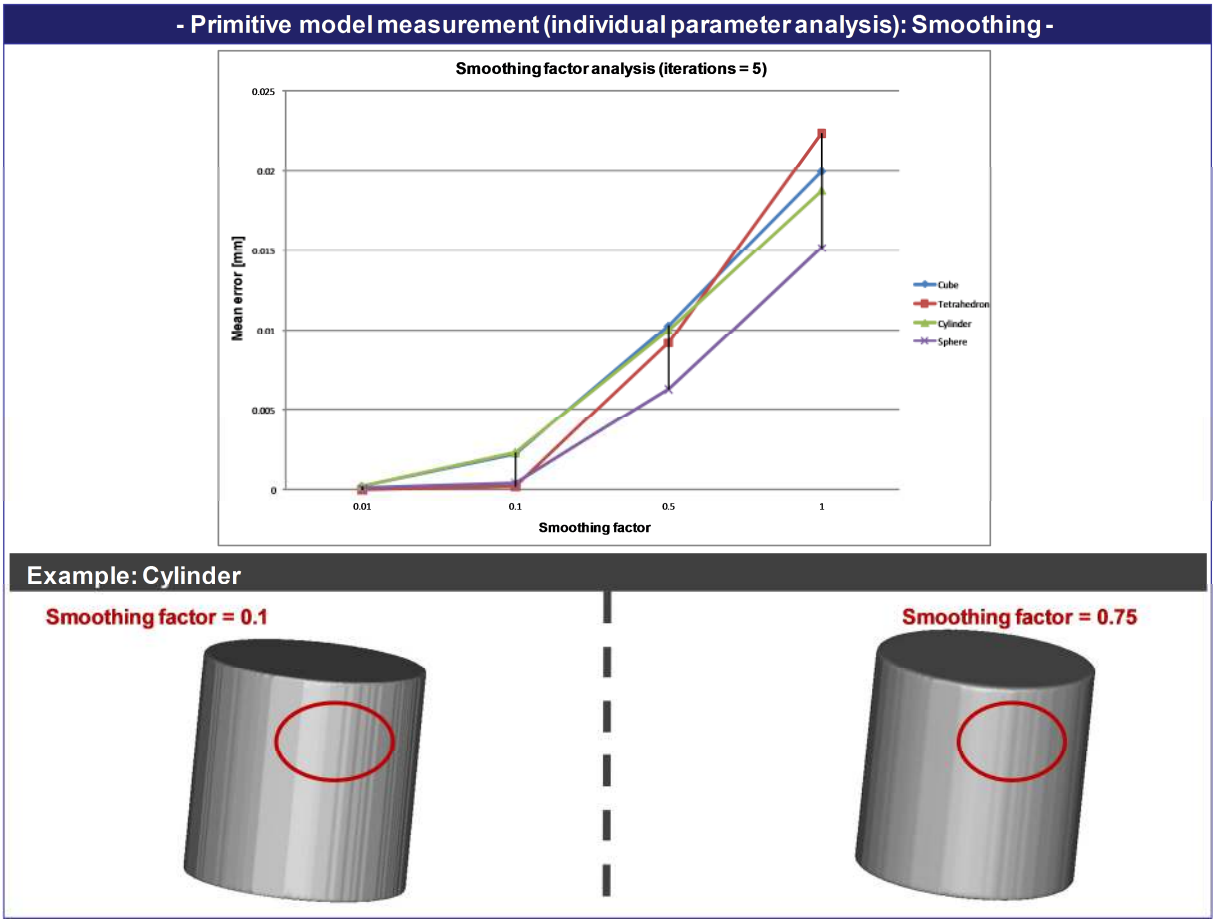

Figure 5-15: Primitive model measurement (individual parameter analysis): smoothing

As Figure 5-15 depicts, higher smoothing factors (e.g., 0.75) improve the optical impression. However, higher deviations result.

The combined use of triangle reduction and smoothing reveals that the standard reconstruction algorithm (advanced edge) used within Mimics leads to improvable results. The most appropriate mode is the point algorithm. The point algorithm eliminates points (vertices) and not edges, whereas the edge algorithm eliminates edges in order to simplify the resulting surface mesh.

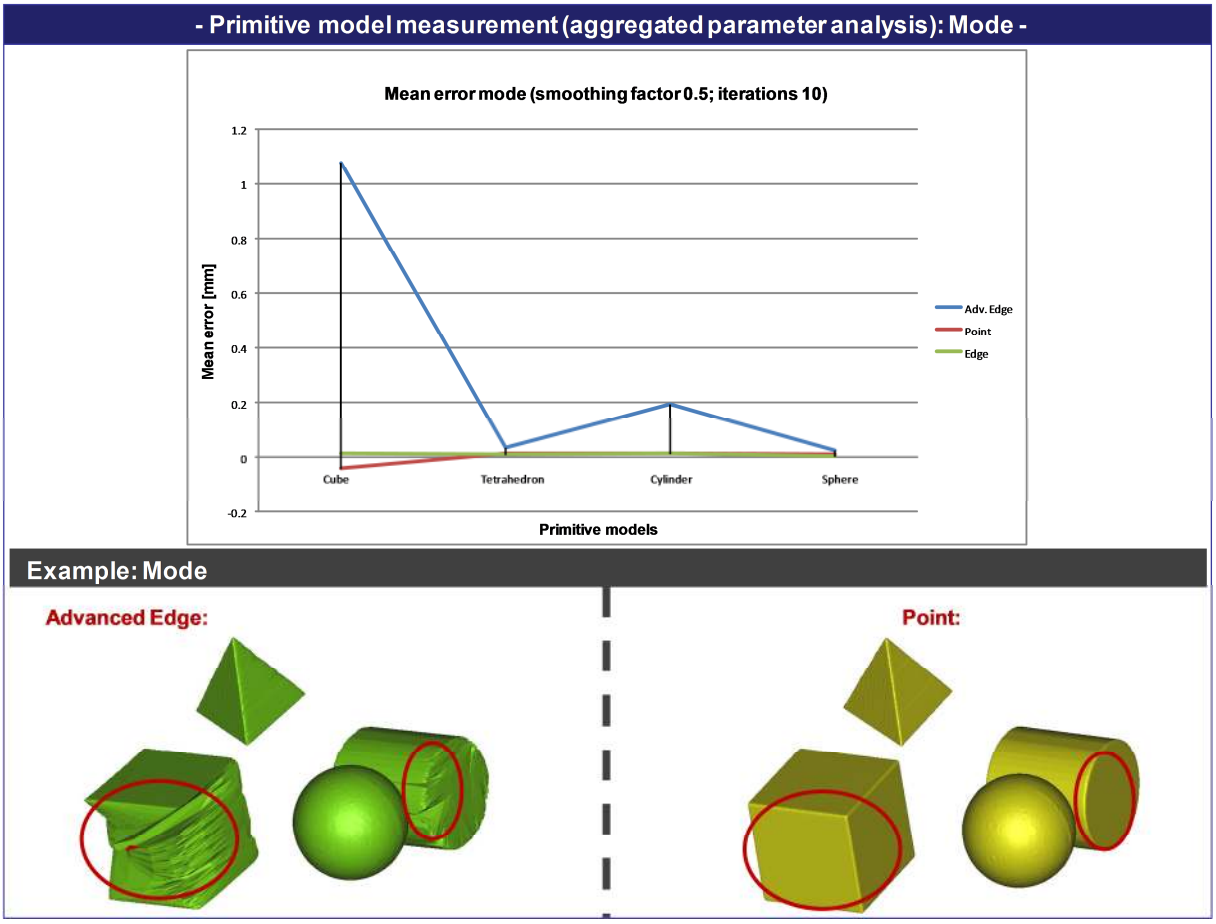

Figure 5-16: Primitive model measurement (aggregated parameter analysis): mode

As shown in Figure 5-16, the advanced edge mode can lead to mean errors of >1 mm. Although, for the cube the point mode shows a small negative deviation, and is most appropriate because surface noise is a slightly reduced compared to the edge algorithm, which is even better than advanced edge.

The triangle reduction parameter tolerance shows the lowest mean error when a value of 0.01 mm is selected.

Table 5-11: Primitive model measurement: aggregated parameters

Parameter	Range of values	Result
Triangle reduction		
Tolerance	0.01 - 0.2 [mm]	0.01 mm is ideally suited → Higher values increase mean error
Edge Angle	1 - 30 [°]	1° is ideally suited →Higher values increase mean error
Iterations	1 – 20	5 iterations are ideally suited → no difference to individual parameter analysis
Mode	Point, Edge, Advanced Edge	Point is ideally suited → Other modes increase mean error and reduce less noise
Smoothing		
Iterations	1 – 20	10 are ideally suited → Lower values reduce less noise; values higher than 10 increase mean error

Factor	0.01 – 1	0.5 is ideally suited → Lower values reduce noise not enough; higher values increase mean error

The remaining triangle reduction and smoothing parameters show results similar to those when they are used separately (Table 5-11).

5.3.2 Medical model measurement

The second measurement shows that both triangle reduction and smoothing parameters produce similar results even if medical models are used (Table 4-12). One again, it can be seen that small values for tolerance and edge angle lead to sufficient results.

Table 5-12: Medical model measurement: aggregated parameters

Parameter	Range of values	Result
Triangle reduction		
Tolerance	0.01 - 0.2 [mm]	0,01 mm is ideally suited → no difference to measurement 1
Edge Angle	1 - 30 [°]	1° is ideally suited → no difference to measurement 1
Iterations	1 – 20	5 iterations are ideally suited → no difference to measurement 1
Mode	Point, Edge, Advanced Edge	Point is ideally suited → Other modes increase mean error and reduce less noise
Smoothing		
Iterations	1 – 20	10 are ideally suited → Lower values reduce less noise; values higher than 10 increase mean error
Factor	0.01 – 1	0.2–0.5 is ideally suited → Lower values reduce noise not enough; higher values increase mean error

When setting small factors for tolerance and edge angle in combination with a smoothing factor of 0.5 with 10 iterations, the deviation of vertices in the nose model can be reduced (Fig. 5-17). For instance, a tolerance of 0.01 mm and edge angle of 1° results in a 45 % deviation of nose model vertices (>0.05 mm). A higher tolerance of 0.1 mm and edge angle of 5° leads to 59 % deviated vertices (>0.05 mm). A deviation of 3 % of all vertices (>0.3 mm) occurs when a tolerance of 0.7 mm and an edge angle of 5° are selected.

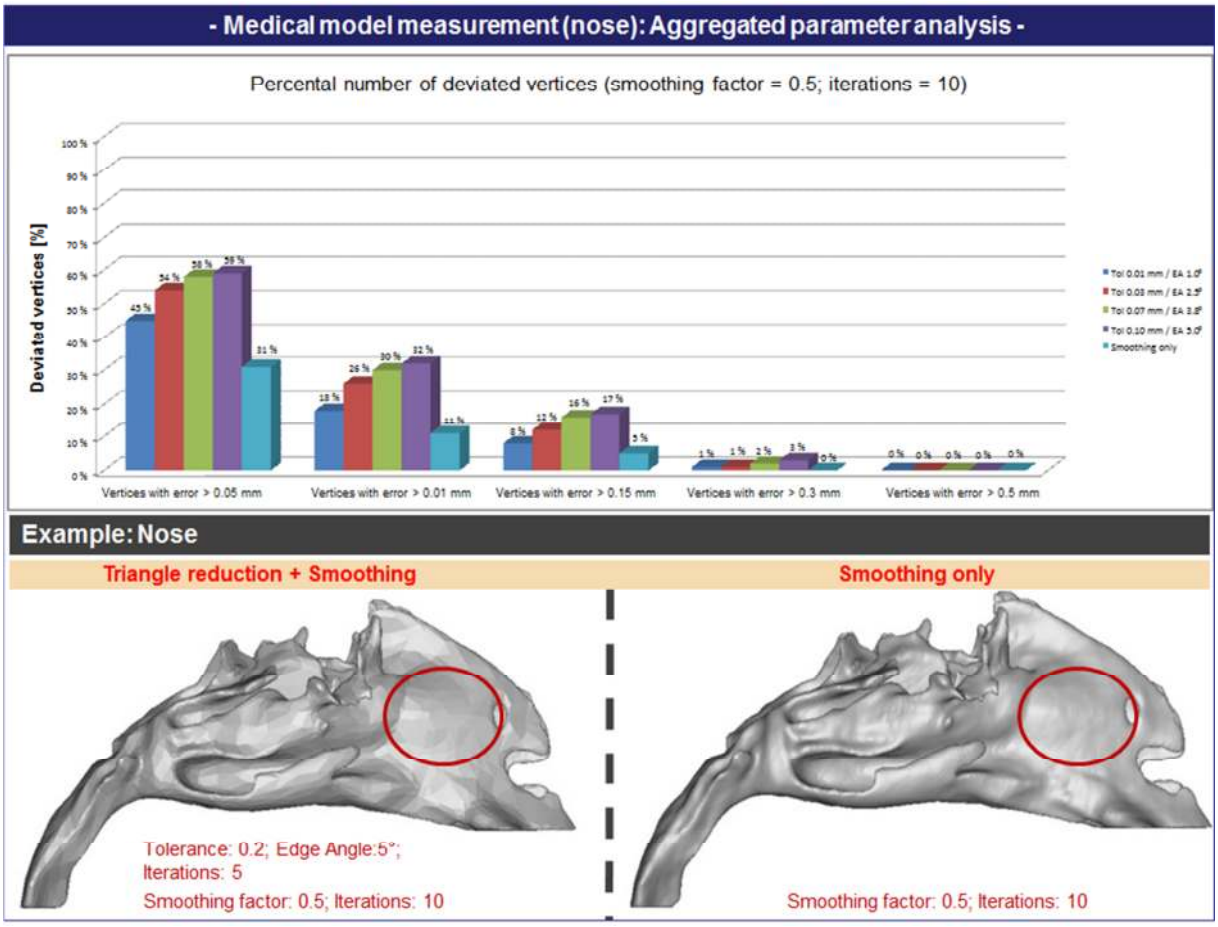

Figure 5-17: Medical model measurement: aggregated parameter analysis

If only smoothing is selected, 5 % of all vertices deviate with an error >0.15 mm, 11 % deviate for >0.01 mm, and 21 % deviate for >0.05 mm. As shown by the red circles in Figure 5-17, smoothing without triangle reduction smoothes the surface mesh in a way that unwanted facets appear to have vanished. The same effects are seen when processing femur and the hip models.

The smoothing factors show the most impact on the meshing behavior (Mallepree & Bergers, 2009a). In comparison to measurement 1, the second measurement reveals that a factor range between 0.2 and 0.5 is ideally suited to improve the edges from 3D reconstruction (Fig. 5-18). The benefit of selecting the appropriate factor of 0.2 for smoothing the surface is shown in Figure 5-18. Here, a factor of up to 0.5 is best suited for the femur and nose model. For the nose model, a smoothing factor of 0.5 yields a 0.0122 mm difference relative to the reference model. The best generation of the hip model occurs with a smoothing factor of 0.2, and produces a mean error of 0.0186 mm.

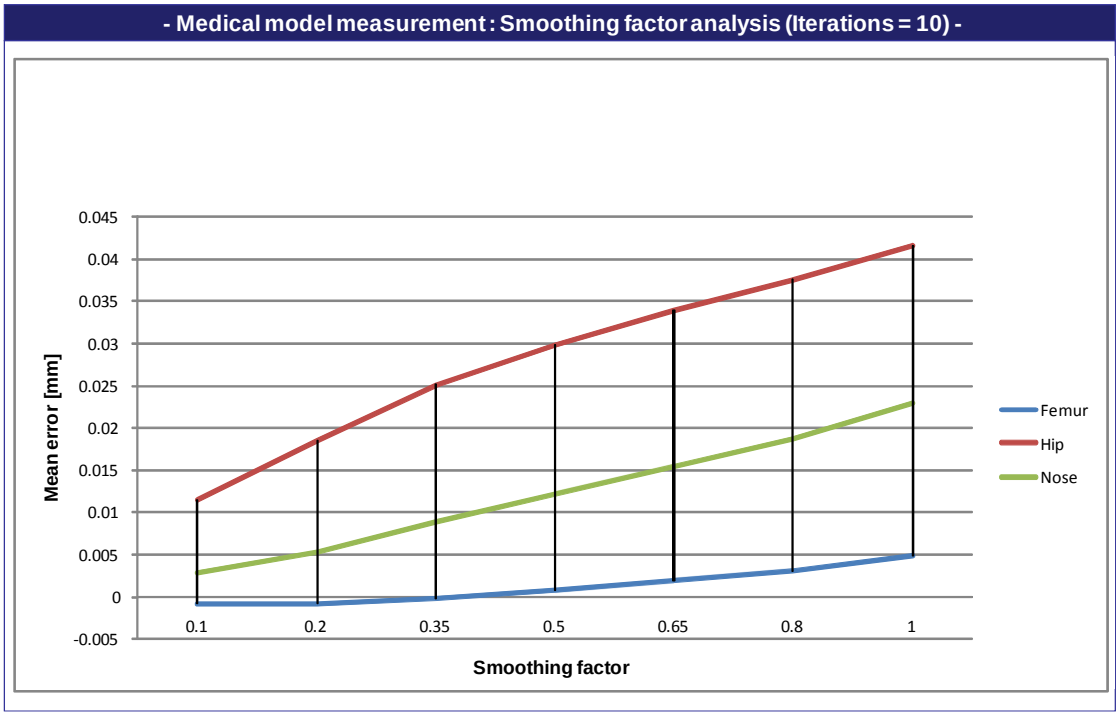

Figure 5-18: Medical model measurement: smoothing analysis without triangle reduction

Therefore, a smoothing factor of 0.2 for the hip and 0.5 for the femur and nose model, are suggested. A comparison of all three medical models studied reveals that a smoothing factor of ≤0.5 with a maximal mean deviation of 0.3 mm.

5.3.3 Conclusion

In conclusion, it has been shown that smoothing should not be used in combination with triangle reduction parameters as long as the .STL model incurs a file size limit of 35 MB, when standard computers are used in post applications. Otherwise, an avoidable loss of accuracy is the consequence. When smoothing alone is used, the MC algorithm's disadvantage of brick-shaped mesh structures can be balanced. A smoothing factor between 0.2 and 0.5 seems to be most appropriate for eliminating the brick-shaped mesh structures. The use of triangle reduction operations should be avoided. If triangle reduction is used, the density of the vertices will be reduced, which leads to a higher degree of approximation. The original model surface, which is built on all available gray values, is forced to deviate. Gray values that already exist are no longer used as information for building the model surface. Thus, actual available accuracy is reduced.

In summary, medical prototyping mesh editing cannot be performed similar to other prototyping applications in which models are generated by means of a 3D CAD system and not by a tomographic scanning machine.

5.4 Surface quality of physical model

The first step of manufacturing an RP model is defining required quality. The quality of an RP model used for medical applications can be directly referred to its geometric accuracy. An additional quality demand frequently called for is the transparency of a manufactured model. A field of research is the use of medical models for flow analysis. Such functional models have to be transparent in order to enable experimental flow analysis (e.g., PIV-method). One possibility to manufacture accurate transparent models for medical applications is the quasi-additive RP procedure of CNC milling. Additive RP procedures (e.g., Stereolithography) are not able to generate transparent anatomical models that are acceptable for accurate flow analysis. Appropriate milling parameters for milling transparent anatomical RP models are determined using test models for finding standardized CAM parameters (Chapter 2.2.2).

In terms of extrapolating results to complex free-form shaped anatomical models, the study design for obtaining appropriate parameters for milling anatomical formed models is based on three test models. The morphology should represent increasing complexity from model to model as depicted in Figure 5-19.

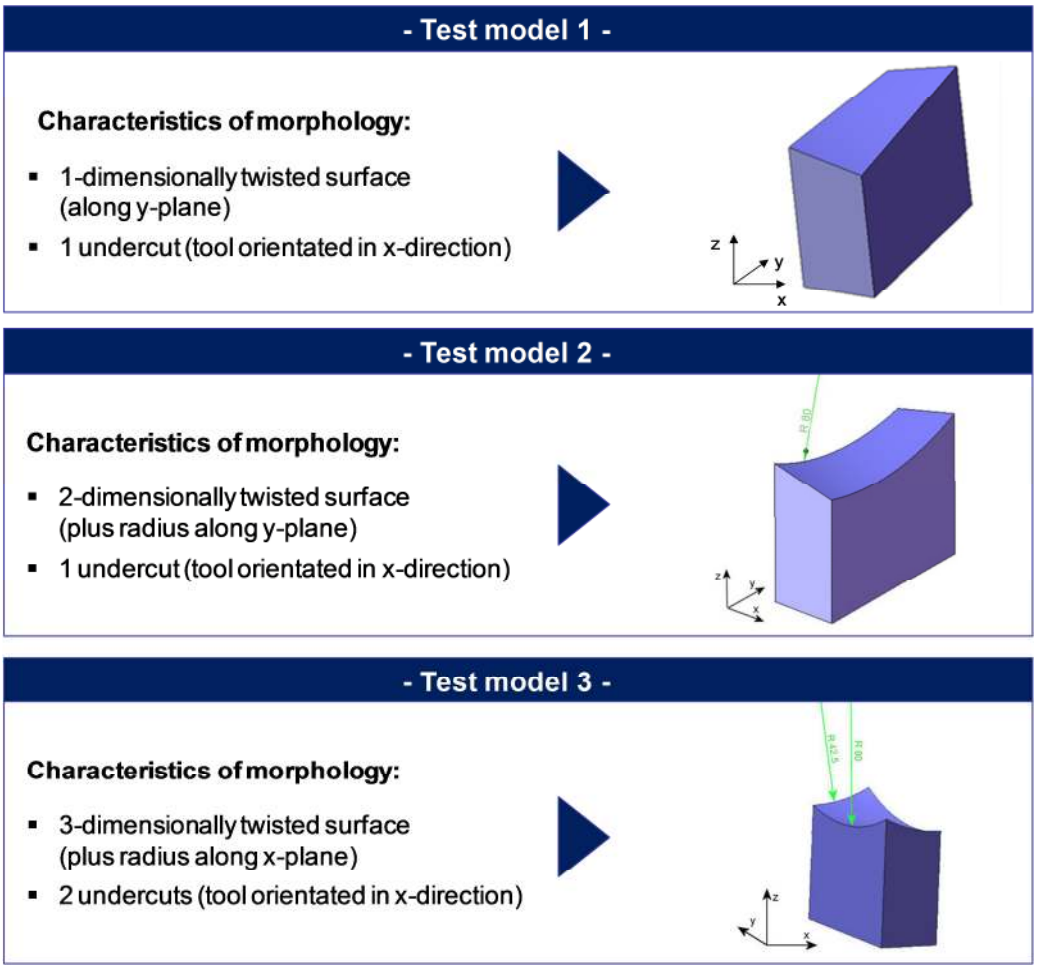

Figure 5-19: Test models 1–3: milling

The raw model is 53-mm long in the y-direction, 43-mm high in the z-direction and 20-mm thick in the x-direction, and is composed of PMMA.

Test model 1 consists of a 1-dimensionally twisted surface. This form permits milling a plane surface with one undercut created by twisting the surface (Fig. 5-19). The second test model consists additionally of a radius along the model's y-plane. The final test model demonstrates the typical scenario, which is often found with anatomical-shaped surfaces. Anatomical surfaces are twisted in all directions, creating morphology without rules. Thus, the third test model is designed in this context and has two undercuts. The situation of undercuts is overcome in milling by turning the test model's milling to the opposite side.
The quality of milled surfaces is measured using a roughness measuring device to obtain statistical data about possible deviations related to the original measure.

5.4.1 Test series 1

Test model 1 tests parameter combinations to determine those parameters influencing milling of anatomical-shaped free-form surfaces (Fig. 5-19). The first parameter test (1) tests the influence of different angles between tool and workpiece, to evaluate the impact of different strategies, and to determine the difference of tool radius of shank cutter and radius cutter (Table 5-13). This evaluation is based on the use of fixed parameters for tool diameter, feed for roughing and smoothing, z-infeed for smoothing, lateral off-set for smoothing, surface tolerance, and chord error.

Table 5-13: Parameters test series 1

Test series 1	1.1	1.2	1.3	1.4	1.5	1.6	1.7
tool diameter	6 mm						
tool	shank cutter					radius cutter	
tool radius	0 mm					3 mm	
feed roughing	500						
feed smoothing	900						
r.p.m.	9000						
infeed roughing	1 mm						
infeed smoothing	0.1 mm						
lateral off-set smoothing	0.1 mm						
surface tolerance	0.005						
chord error	0.0075						
strategy	linear 0° columns/forward & backward	linear 90°rows / forward& backward	linear 0° columns/forward & backward	linear 90°rows / forward& backward	linear 0°columns / forward		linear 90°rows / forward& backward
angle between tool & workpiece	10°		20°				
Test series 1	**1.1**	**1.2**	**1.3**	**1.4**	**1.5**	**1.6**	**1.7**

The use of a radius cutter and a strategy of linear 0° (row) in test series 1.6, influences the surface quality more than other proposed parameters. The geometry is milled without surface damage and translucency is superior to other tested models.

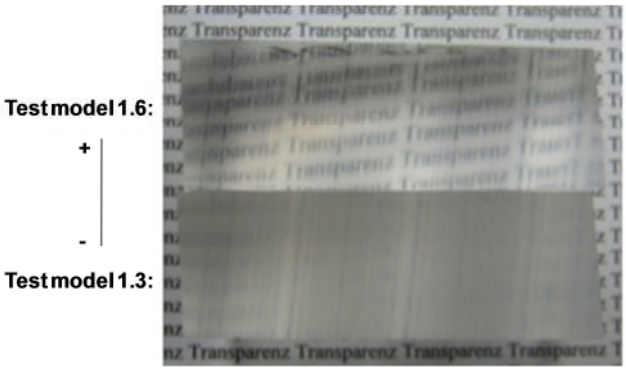

Figure 5-20: Milling result: test series 1

As Figure 5-20 shows, test series model 1.6 consists of much higher qualitative surfaces than the test series model from 1.3, although tool radius and the cutting direction are the only different parameters.

Comparing the results of the conducted survey with roughness measurements reveals that choosing milling parameters of test series 1.6 are best for producing accurate and transparent surfaces (Fig. 5-21).

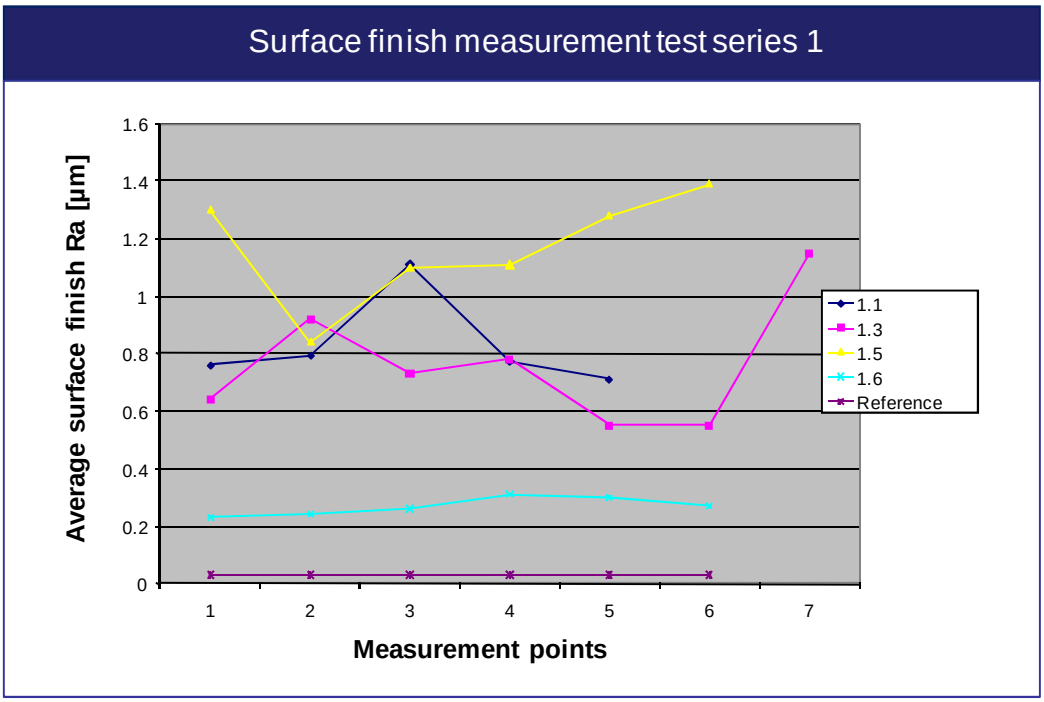

Figure 5-21: Evaluated results: test series 1

Moreover, the evaluation reveals that a smoothing strategy < 90° is suboptimal. A column-by-column strategy <0° seems to create a better surfac e that the use of a row strategy in milling a twisted surface. Test series 1 shows that a radius cutter with an edge radius that meets half of the tool radius shows a better result than using a shank cutter with an identical diameter. The measurement results (Fig. 5-21) testify that test model 1.6 (Fig. 5-20), which is milled with a radius cutter, features the best transparency. An additional result of these tests is that a variation of cutting direction leads to different levels of transparency. Test models

1.3 and 1.6 feature different surface qualities (Fig. 5-20) although only the parameter cutting direction is varied. Thus, different cutting directions should be tested again in test series 2 using a double-twisted model (Fig. 5-19).

5.4.2 Test series 2

The second test model is a modification of test model 1: it uses a double-twisted surface. First, the model is roughed and then finished in order to mill the contour. For test series 2.1–2.4, the parameters found in test case 1.6 will be applied, varying only the cutting direction. Test series 1 shows that various cutting directions lead to differing surface quality. Here, the objective is to determine the optimal cutting direction.

Table 5-14: Parameters: test series 2

Test series 2	2.1	2.2	2.3	2.4	2.5	2.6	2.7	2.8
tool diameter	6 mm							
tool	radius cutter							
tool radius	3 mm							
feed roughing	500							
feed smoothing	900						1800	250
r.p.m.	9000							
infeed roughing	1 mm							
infeed smoothing	0.1 mm							
lateral off-set smoothing	0.1 mm							
surface tolerance	0.005							
chord error	0.0075							
admeasure roughing	0.5 mm				0.7 mm	0.5		
positioning of tool	inside				outside			
strategy	linear 0° columns/forward & backward	linear 0° columns / forward	linear 0° columns / backward		linear 0° columns / forward	linear 0° columns/forward& backward		
angle between tool & workpiece	20°							
Test series 2	**2.1**	**2.2**	**2.3**	**2.4**	**2.5**	**2.6**	**2.7**	**2.8**

As Table 5-14 shows, the feed for smoothing is varied as an admeasure for roughing and positioning of the tool.

The resultant models 2.1–2.4 show no differences and feature the same partial damages of identical position and size, as demonstrated by Figure 5-22.

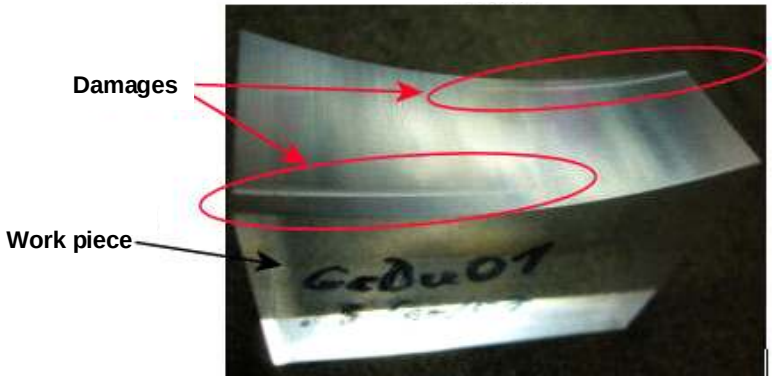

Figure 5-22: Damages test series 2

A variation of the cutting direction along smoothing has impact on surface transparency. Test series 2 shows that a variation of cutting direction mainly influences manufacturing time. It can be seen that transparency is best in cases 2.1 and 2.4, but the manufacturing times are very different. The manufacturing time of test model 2.1 is 72 minutes while test model 2.4 is 127 minutes (56 % more). Visible tool paths cannot be avoided by an adjustment of parameters along roughing. That leads to the suggestion that visible tool paths are caused along smoothing. An additional finding is that damages in the border area of the surface can be reduced by a change of the tool end position without influencing surface transparency. To improve the transparency found in test series 1, feed is also varied. Test models 2.7 and 2.8 are manufactured using the same parameters as model 2.6 but feed is varied (Fig. 5-23).

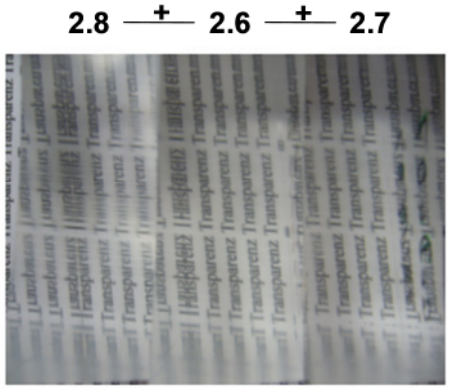

Figure 5-23: Models: test series 2

Test models 2.6, 2.7 and 2.8 have the best surface transparency as shown by Figure 5-24. The metrological analysis shows only very low deviations of resultant surface roughness.

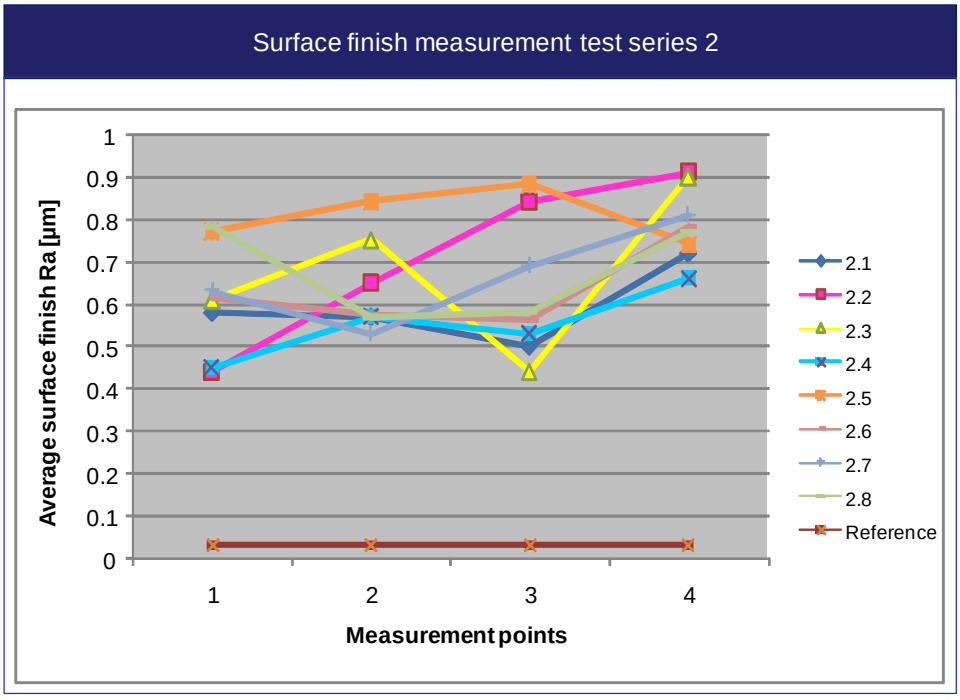

Figure 5-24: Evaluated results: test series 2

All measurement results are between 0.44 µm and 0.91 µm. Analyzing resulting surfaces, it can be stated that transparency is best if a feed >900 mm/min is used.
As analyzed in test series 1, feed can influence transparency of plane surfaces. A transfer to twisted surfaces cannot be made so far. An additional analysis is carried out in the following chapter to find the optimal parameters for milling multi-twisted surfaces.

5.4.3 Test series 3

Test model 3 has a 3D-twisted surface, a free-form-shaped curvature that is additionally twisted in two more directions. As demonstrated the parameters of test series 2.6 are useable for milling surfaces with good transparency. However, the final parameters in transparent surfaces of more complex morphologies remain unclear. Moreover, the optimal feed for smoothing has to be determined. In test series 3, various feed rates are analyzed (Table 5-15). An additional point to analyze is the blade angle: the angle between tool and workpiece, in order to determine optimal blade angle.

Table 5-15: Parameters: test series 3

Test series 3	3.1	3.2	3.3	3.4	3.5	3.6
tool diameter	6 mm					
tool	radius cutter					
tool radius	3 mm					
feed roughing	500					
feed smoothing	900				1800	250
r.p.m.	9000					
infeed roughing	1 mm					
infeed smoothing	0.1 mm					
lateral off-set smoothing	0.1 mm					
surface tolerance	0.005					
chord error	0.0075					
admeasure roughing	0.5 mm					
positioning of tool	outside					
strategy	linear 0° columns/forward& backward					
angle between tool & workpiece	20°			28.5°		
cutting area	plane	frame	frame	plane		
Test series 3	**3.1**	**3.2**	**3.3**	**3.4**	**3.5**	**3.6**

The analysis demonstrates that the optimal blade angle in the present case is 28.5 °. Other angles lead to surface damage.
The metrological analysis reveals that for measurement series 3 that test models 3.4, 3.5, and 3.6 have the best surface quality.

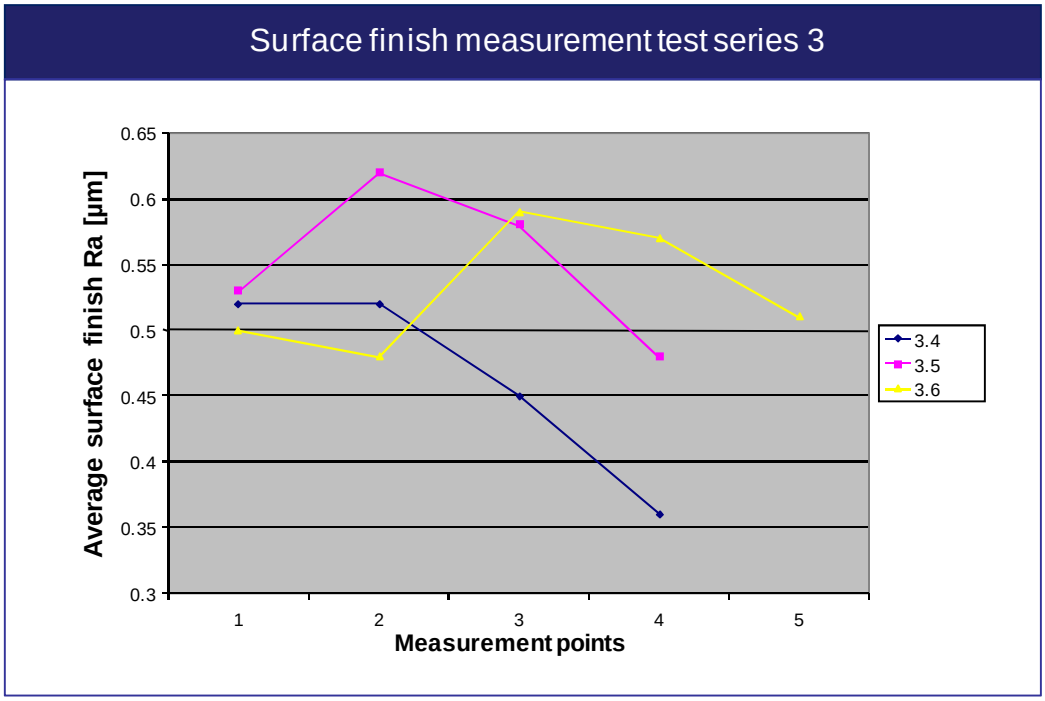

Figure 5-25: Evaluated results: test series 3

The roughness of models 3.4–3.6 is between 0.36 µm und 0.62 µm (Fig. 5-25). Moreover, Figure 5-26 shows that model 3.6 has the best transparency.

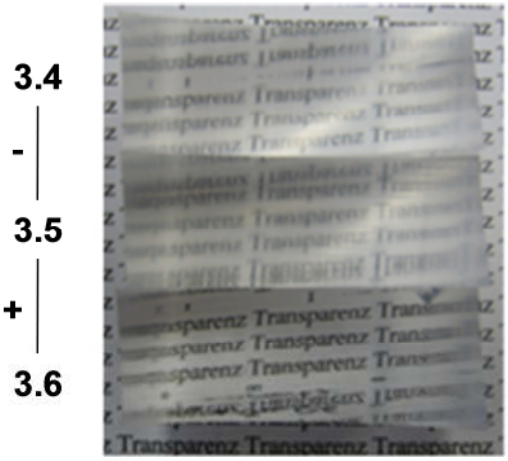

Figure 5-26: Models: test series 3

Both of models 3.4 and 3.5 have smooth surfaces but are not as transparent as the surface of model 3.6.

5.4.4 Conclusion

The test series determining optimal parameters for generating transparent, anatomical-shaped free-form surfaces by CNC milling, revealed that parameters exist that permit the

generation of complex-shaped and transparent surfaces. One possible limitation however is that final parameters have to be adjusted, mainly in the case of using a different material, machine, and operator. In summary, the following constraints should be taken into account: Selection of an appropriate tool has to be made; if possible, as short as possible. Tool diameter should be as large as possible in relation to the work piece morphology (pockets, etc.). If there are bevels and undercuts to mill, the blade angle has to be adjusted to the operated surface. In cases in which the surface cannot be milled by the front face of the tool, a radius cutter should be used. The radius cutter's diameter should not be set <3 mm. Otherwise, revolution speed has to be increased to >9000 r.p.m. to generate transparent surfaces. If the use of a radius cutter is unavoidable, a very small increment has to be chosen in combination with highest possible revolution speed and adjusted smoothing feed. If triangulated volume models are used, fault tolerance should always be 150 % of the value of chord error in combination with data models of highest mesh quality.

The present investigation reveals that a cutting speed (V_c) of 84.8 m/min is optimal (formula II-5, Chapter 2.2.2) in relation to a feed rate for smoothing of 250 mm/min. This result is contrary to results of Dominghaus (2007) and Michaeli (1999), who both recommend a cutting speed of up to 1000 m/min or more for thermoplastics and PMMA, respectively. In this respect a loss of transparency is the consequence. In particular, when milling medical models, complex geometries have to be machined and this necessitate radius cutters of small diameters to operate small bevels and gaps. The present result reveals that the generation of transparent surfaces depends not on high revolution speeds, which lead to high cutting speeds, only. The optimal interplay of cutting speed and feed rate enables machining transparent surfaces of medical models under the conditions presented in Table 5-15. Thus far absent in the literature, the process of milling has to be developed more into a process of polishing than of chipping. By operating with these presettings, the tools cut the material slower and surface roughness (R_a) is reduced.

Finally, it was found that manufacturing time increases rapidly if high transparent surfaces are demanded. For example, if values for smoothing infeed and lateral off-set are increased from 0.1 mm to 0.2 mm, then manufacturing time become only one quarter of the normal time required. Thus, if manufacturing time has to be reduced, revolution speed should be increased (high-speed cutting).

When conducting the quasi-additive RP process, contouring is followed by the step of joining (Chapter 2.2). In order to guarantee sufficient accuracy in joining a number of slices (e.g., 20 slices) of a quasi-additive RP model containing an inner geometry, an appropriate clamping and joining principle is necessary as well as even model slices, highly accurate drill holes, and minimized contour deviations.

5.5 Slice joining accuracy

Standard clamping procedures do not allow clamping and re-clamping a workpiece repeatedly. This possibility would ensure that all positions were identical to the previous clamping. A sufficient repeat accuracy is difficult to achieve. One solution is to combine positioning and joining in one process (Assmann, 2003) and is similar to the stratoconception process (Barlier and Gasser, 1995). In order to assure accuracy in joining a high number of slices, an optimized joining procedure is necessary. In the case of various model slices ($X_1 \ldots X_n$), an additional model slice (X_{n+1}) is used as reference slice for positioning and clamping. First, this reference slice, as well as the remaining slices, needs through-holes. These through-holes are then drilled in a one-step sequence. Next, the reference slice is positioned and clamped by a screw on the machine table. In the following, the model slices ($X_1 \ldots X_n$) are clamped on the reference slice by aligning pins. If necessary, a model slice can be machined from two sides by retaining the original position. The aligning pins allow an exact positioning of all slices that have to be machined. Figure 5-27 also shows that the aligning pins are used as fixture elements.

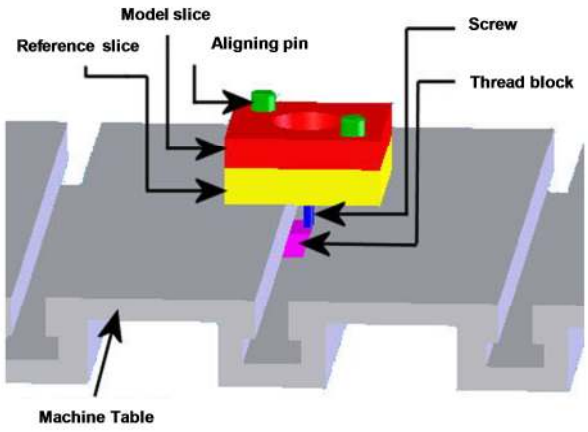

Figure 5-27: Positioning and clamping (PC) principle

As Figure 5-27 demonstrates, a successive model slice can be positioned on the machine in exactly the same position as the previous slice. This principle allows adjusting the work piece coordinate system in one step so that additional model slices can be processed in exactly the same position, every time. In order to validate the PC principle (PCP) and to guarantee an exact joining of model slices, measurement series were carried out to evaluate evenness of model slices, drilling deviation, and contour deviations.

5.5.1 Measurement of evenness

Model slices should be absolutely even to guarantee that no gaps exist after joining. Figure 5-28 shows that a square block is used as a test model, which has a thickness of 16.666 mm as check size. The test model is composed of PMMA. An inserted-tooth face milling cutter is used for milling the surface and a CMM is used for taking 100 measurement points on the surface as demonstrated by Figure 5-28.

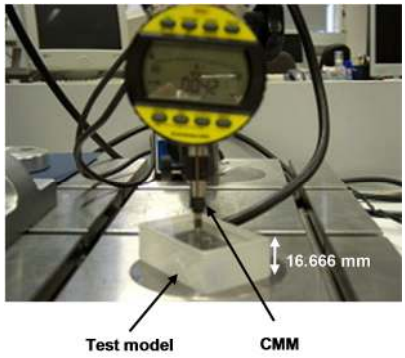

Figure 5-28: CMM

The lowest measure is 16.649 mm with a deviation of 0.0176 mm and the highest measure is 16.670 mm with a lower deviation of 0.01234 mm. A mean deviation of 0.00176 mm is considered acceptable. In particular, a mean deviation of 0.0026 mm confirms the applicability of the procedure.

5.5.2 Measurement of drilling deviation

To verify accurate joining, the slices have to be brought exactly into position. For evaluating possible deviations, a measurement study is carried out by using six model slices of PMMA together forming a model thickness of 100 mm. The objective is to evaluate whether aligning pins of 10-mm diameter and 100-mm length can be used for joining the slices. A distance of 17.5 mm between each through-hole is given (Fig. 5-29).

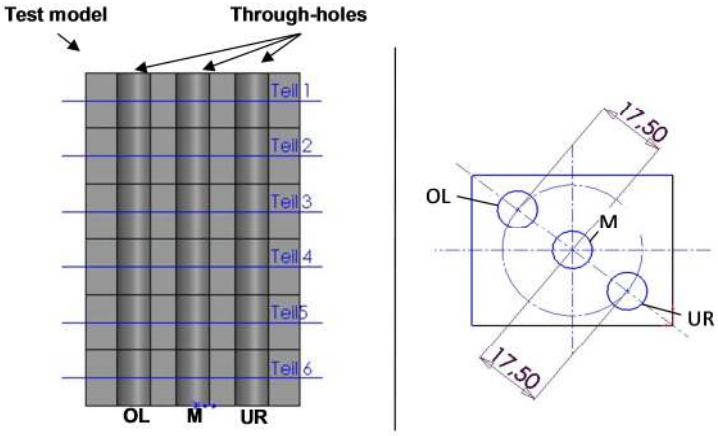

Figure 5-29: Drilling deviation

The maximum deviation of hole position, from the top slice to the bottom slice, is 0.056 mm. The maximum deviation of the diameters measured is 0.032 mm. The mean deviation of OL is 10.0218 mm, of M 10.0083 mm, and of UR 10.0131 mm, by taking six measurements in each case.

5.5.3 Measurement of contour deviation

To determine possible deviation of the joined contours, the test model slices are brought into operation one after another. The medial diameter is milled out to 18.000 mm. The six slices (Fig. 5-30) are clamped using the introduced PCP (Chapter 4.2.5) by using the outer drill-holes for clamping.

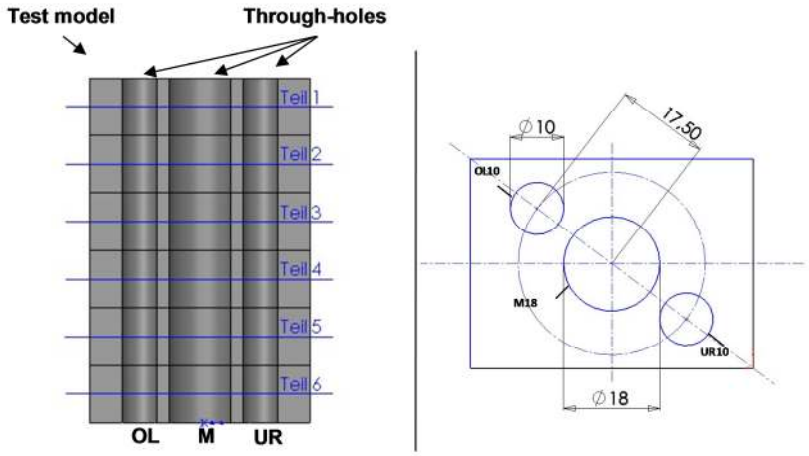

Figure 5-30: Contour deviation

First, the diameter of the drilled-out contours is measured six times. The mean diameter of M18 is 17.945 mm, of OL10 10.008 mm, and of UR10 10.011 mm. Secondly, the space between each contour drill-out is measured six times. The mean diameter for M_OL is 17.482 mm, and for M_UR 17.577 mm.

In conclusion, a quasi-additive fabricated RP model can be produced very accurately, although the final model is composed of joined slices. To guarantee high accuracy, the presented procedure is based on accuracy settings taken from state-of-the-art CNC controlling (e.g., Heidenhain).

Thus, medical model composed of various model slices is of high accuracy and transparency if proposed principles and parameters for RP fabrication are taken into account.

6. Example of use: The human nose

Preparing a (3D) geometry of the human nose for digital processing allows the derivation of virtual and physical medical models for presurgery planning, including surgery intervention planning and fluid dynamic analyses. Such model-based planning procedures support the analysis of final surgery outcomes with respect to patient-specific CAS planning. To date, specific flow characteristics of the human nose are difficult to analyze experimentally because due to difficulties inherent in providing an accurate facsimiled model of the complex geometry of the human nose, for VP and RP. Here, the goal is to obtain knowledge about the physiology and pathophysiology of normal nasal breathing (Masing, 1966; Hess et al., 1992; Chung et al., 2006; Hörschler et al., 2005; Kelly et al., 2000; Kim et al., 2006). Nose surgery is among the most often performed surgical treatments in the western world because impaired nasal respiration is a common and widespread disease. To obtain knowledge about the flow characteristics of the human nose, models are needed that represent the human nose as accurately as possible. In the following, a discussion of medical background outlines the need for appropriate engineering tools in the given medical context. Finally, prototyping solutions are realized in order to demonstrate the appropriateness of MPP as a biomedical engineering application.

6.1 Medical background

The human nose is a sense organ and is a part of the vocal and respiratory system. Considering anatomy, the human nose consists of two parts: The outer part is skin-covered cartilaginous, osseous tissue. The inner part consists of two nasal cavities that are separated by the septum nasi. The nasal conchae ambilaterally divide the nasal cavities in canals (meatus). Behind the anterior part of the nasal cavity is the vestibulum nasi that ranges to the nasal valve (limen nasi). The limen nasi represents the tightest lateral cut (isthmus nasi, or ostium internum). After the isthmus nasi one finds the main nasal cavity (cavum), which extends to the choana and nasopharynx. The top is built by the nasal bone, the lamina cribrosa, and the body of sphenoid bone. The bottom is built of the hard palate (palatum durum). The lateral nasal septum is connected to the upper jaw, os lacrimale, palate bone, sphenoid bone, and nasal conchae. The concha nasalis superior and concha nasalis medius are connected with ethmoid bone, whereas the concha nasalis inferior is composed of its own bone. The nasopharynx is a part of the pharynx and can be viewed as the exit of the inner nose (Fig. 6-1). The inner nose is mostly lined with erectile soft tissues, and mucosa distributed with sensory cells.

The function of the human nose is diverse, ranging from respiration; warming, precleaning, and moistening of air; olfaction; to voice formation.

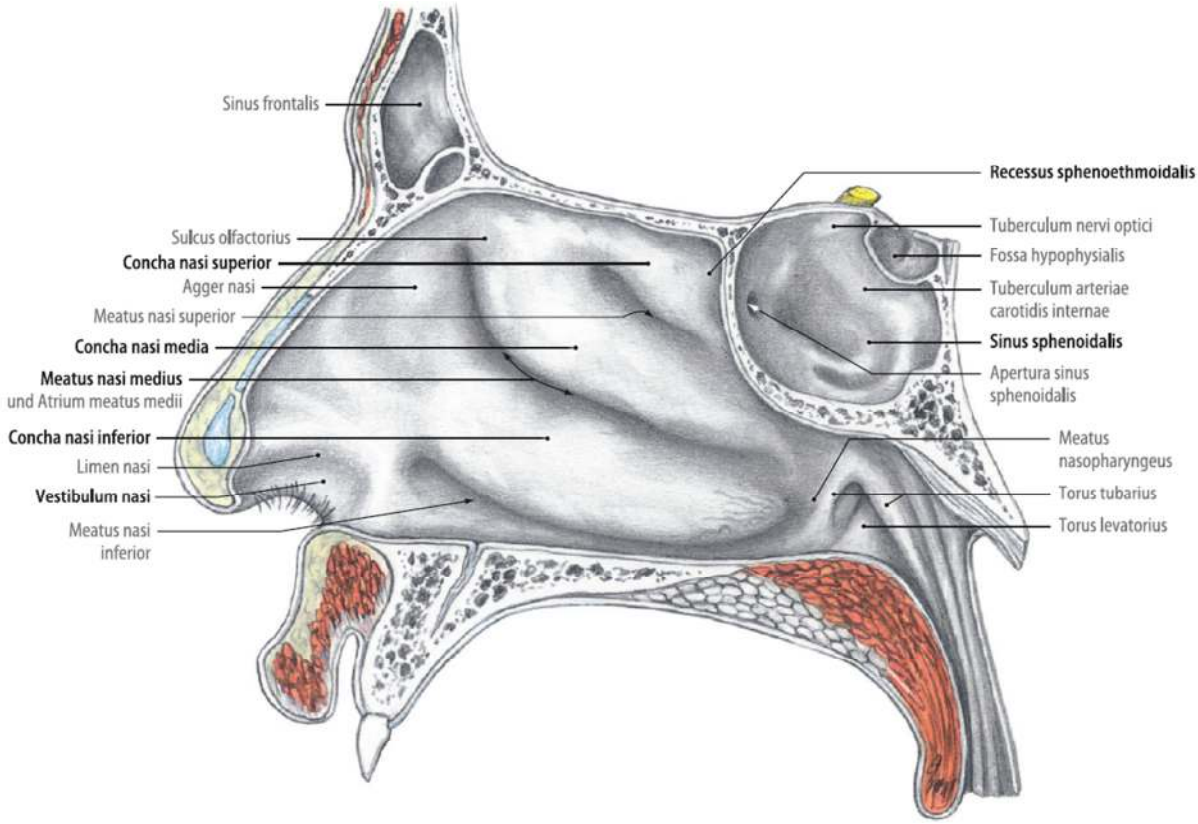

Figure 6-1: Human nose anatomy, sagittal view (Tillmann, 2009)

The vegetative control of respiratory functions of the nose are the regulation of respiratory flow, the heating of breathable air to 32–34° C, hu midification, and cleaning of inhaled air. The control and heating of breathable air is realized by differential swelling of the mucosa of the septum and nasal conchae.

The general functioning of the human nose is strongly related to respiratory flow behavior. Reasons for dysfunctional respiratory flow can be differentiated into congenital and accident-related changes in nose anatomy, and problems based on soft-tissue swelling caused by, for example, chronic or allergic rhinitis.

As stated by Kayser (Kayser, 1895) and Tonndorf (Tonndorf, 1938), detailed nasal flow analysis is needed to assist the restoration of defects. However, such investigations are rarely seen because of resources that are often missing (Eccles, 2001). Thus, due to the absence of both virtual and physical individual nose models, which allow representative flow analysis (Chapter 3), a need is identified. Although methods exist, such as rhinomanometry

for air resistance measurements, a detailed understanding of the interface between flow behavior and patient sensation is missing (Naito et al., 1988; Jones et al. 1989).

First, to support this research, an installation process is needed for deriving geometric information for virtual models to carry out a surgery planning virtually and to provide models for numerical flow analysis. Second, physical RP models are needed for experimental investigation. In sum, there is established clinical value for the development of a procedure for processing medical models of the human nose.

The main challenge in reconstructing the human nose is that the fine structures of the nose are visible only by conducting specific tomographic scans with specific scan parameters. Additionally, scanned medical images need a conversion step, in the successive case that a 3D model is prepared for VP and RP processing. The designed MPP (Chapter 4) addresses the demands of feasibly processing complex anatomical models.

6.2 Modeling the human nose

The anatomical components needed for 3D reconstruction of the nasal anatomy include the following anatomical landmarks (Table 6-1).

Table 6-1: Landmarks of the human nose

An	Agger nasi
Ci	Concha inferior
Cm	Concha media
Cs	Concha superior
Hsl	Hiatus semilunaris
Ie	Infundibulum ethmoidale
Mni	Meatus nasi inferior
Mnm	Meatus nasi medius
Mns	Meatus nasi superior
Pu	Processus uncinatus
Sn	Septum nasi

The landmarks depicted in Table 6-1 are determined in CT images for segmentation (Fig. 6-2).

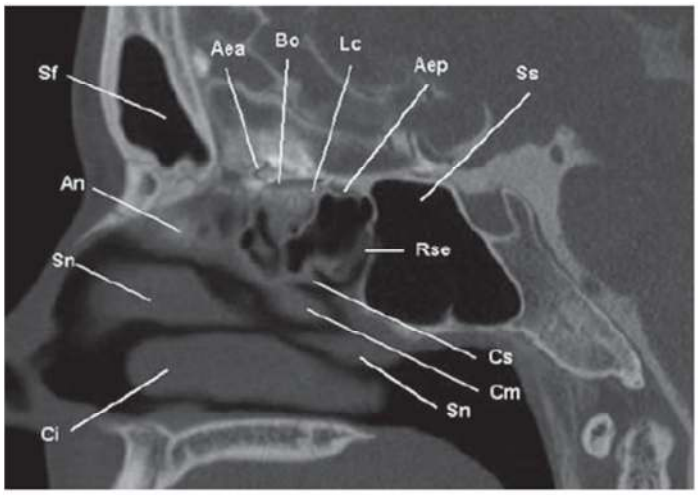

Sagittal view in height of Infundibulum ethmoidale

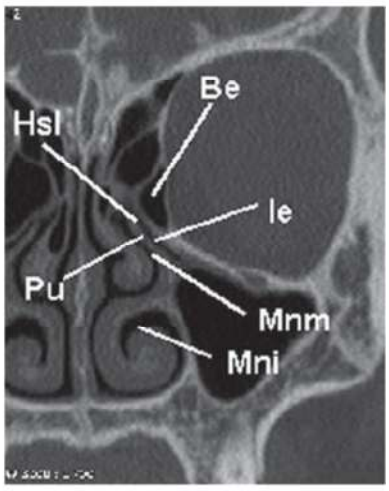

Coronal view in height of Infundibulum ethmoidale

Figure 6-2: Views in height of Infundibulum ethmoidale (adapted from Hofmann, 2005)

Understanding the process of 3D reconstruction to derive 3D models implies that parameters are needed for scanning and data editing. This process of biomodeling consists of RE, segmentation, and mesh editing, as well as its subtasks (Chapter 4.1).

6.2.1 Data acquisition

The acquisition of medical image data by medical imaging scanners depends on defined scan protocol. Raw data are generated in the scanning machine for deriving .DICOM data that contain the scanned medical image slices. Here, the objective is to process .DICOM data by specific segmentation methods during a 3D modeling process. In finding the appropriate parameters for deriving 3D geometry data, the acquisition of useful data in the scan protocol must be ensured. The following parameters are set before the execution of scans:

a) Determination of scanner
b) Scan direction and position
c) FOV
d) X-ray dose (CT)
e) Slice thickness
f) Slice increment
g) Filter algorithm
h) Resolution
i) Artifacts

The present examples employ the CT scanner Somatom Definition Open (Siemens), a state-of-the-art multi-slice scanner capable of taking 40 slices per rotation (a). The direction for scanning the nose is axial (b) and the field of view is set by a boundary box as close as possible around the object of interest (c). The slice thickness (e) and the slice increment (f) are selected as small as possible in order to attain isotropic voxels along with overlapping slices. The slice thickness and slice increment are the most important parameters to set for 3D reconstruction (Chapter 5.2.3). Nevertheless, two points of conflict must be attended to: First, X-ray dose (d) and second, image noise. The choice of too small parameters for slice thickness and slice increment, results in high X-ray doses, which should be avoided for the sake of patient health, and in noisy images. Noisy images lead to rough and sprinkled surfaces that are not acceptable (Chapter 4.2.1).

In reconstructing the human nose, smooth surfaces are especially important to represent fine structures. Therefore, an optimal adjustment of scan parameters, X-ray dose, and appropriate filtering (g) are the principle objectives in reconstructing the nose in 3D. Image resolution is defined by a 512×512-image matrix (h) and sources of artifacts should be avoided, e.g., scanned dental fillings.

Three cases are analyzed by using different scan protocols and shown in Figure 6-3. Three different scans were conducted to verify the best possible model quality. The quality of images in the image plane (x-y) is determined by the appropriate filter algorithm, which is given here as H50s (Siemens, München), a bone filter algorithm for scanning the head; hereby amelioration of the problems of sharp images with too much noise or images with low noise but smudged edges is achieved. Parameters are varied from 5-mm slice thickness and 5-mm slice increment in case 1 to 1-mm slice thickness and 0.5-mm slice increment in case 3. In case 3 a fine resolution is chosen to attain 0.5 mm-overlapped images. This selection depends on the fact that quality of 3D-reconstructed medical models depends not on setting high local resolution in the image plane but rather on the isotropy of voxels.

1

Scan parameters	Values
Scanner	Siemens Somatom Definition
Scan direction and position	axial
Field of view (FOV)	17.5 cm²
X-ray dose	120 kV
Slice thickness	5 mm
Slice increment	5 mm
Filter algorithm	H50s
Resolution	512x512
Artifacts	none

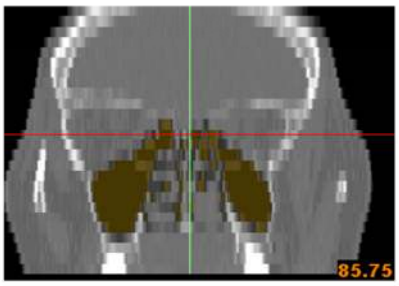

2D nose coronal view

2

Scan parameters	Values
Scanner	Siemens Somatom Open
Scan direction and position	axial
Field of view (FOV)	17.5 cm²
X-ray dose	120 kV
Slice thickness	3 mm
Slice increment	3 mm
Filter algorithm	H50s
Resolution	512x512
Artifacts	none

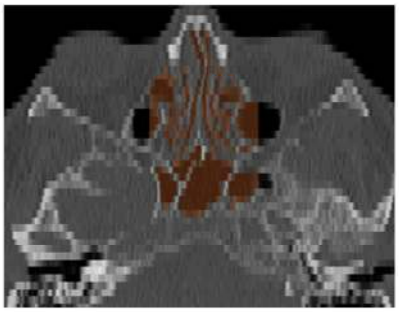
2D nose axial view

3

Scan parameters	Values
Scanner	Siemens SomatomOpen
Scan direction and position	axial
Field of view (FOV)	17.5 cm²
X-ray dose	120 kV
Slice thickness	1 mm
Slice increment	0.5 mm
Filter algorithm	H50s
Resolution	512x512
Artifacts	none

2D nose coronal view

Figure 6-3: Acquisition parameters nose models

The ideal situation is to derive isotropic (cubic)-shaped voxels and not volume elements that are more similar in shape to a stick than to a cube. To achieve the goal of obtaining cubic voxels, overlapping reconstruction processing generates 3D models with a minimum of artifacts, such as partial volume effects, staircase effects, etc.

6.2.2 Segmentation and 3D reconstruction

In CT image data, air appears with a mean intensity of approximately –1024 Hounsfield units (HU). Most tissue of the nasal cavity ranges from 20–130 HU, while cartilage and bone structures are much denser (well above 800 HU). Three exemplary regions of interest are presented in Figure 6-4 in order to demonstrate the selected threshold for each region,

based on the defined gray values. The combined processes of the curvature flow filter (Chapter 4.2.1) and threshold-based segmentation decrease unnecessary noise and intensify geometrical boundaries.

The software Mimics (Chapter 2.1.6) is used for segmentation and 3D reconstruction. The segmentation of the human nose is based on manual thresholding, which is based on accurate gray value determination. For instance, gray value determination for segmenting the conchae nasalis inferior is carried out by setting a number of gray value markers from which an average gray value may be determined. This average value determines the boundary between mucosa and air.

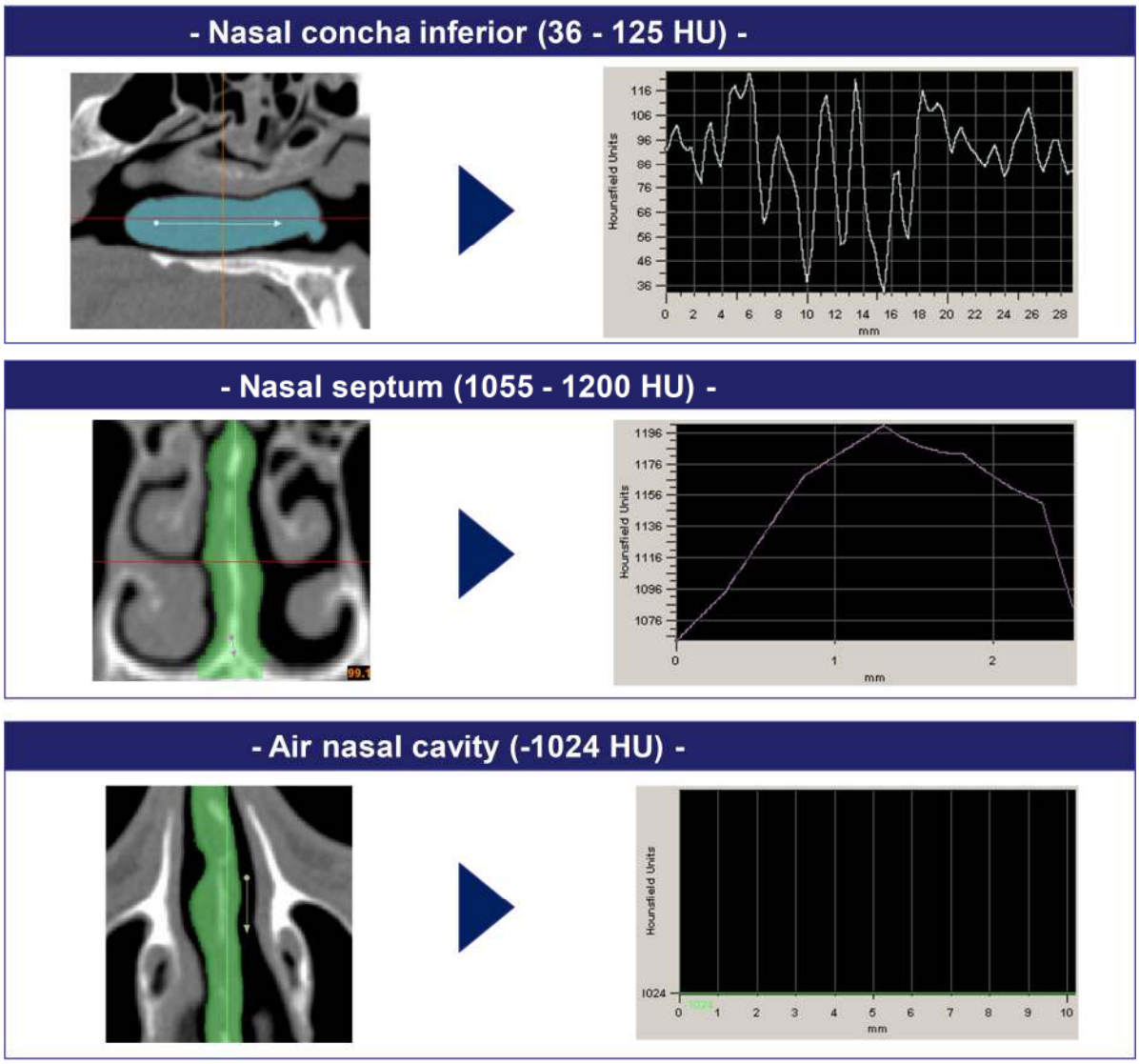

Figure 6-4: Threshold values human nose

After the appropriate gray value is found, the threshold is set (e.g., for segmenting the nasal conchae inferior the threshold is –240 HU to –1024 HU (Fig. 6-4). As a result, the segmented region is obtained and this is used for 3D reconstruction.

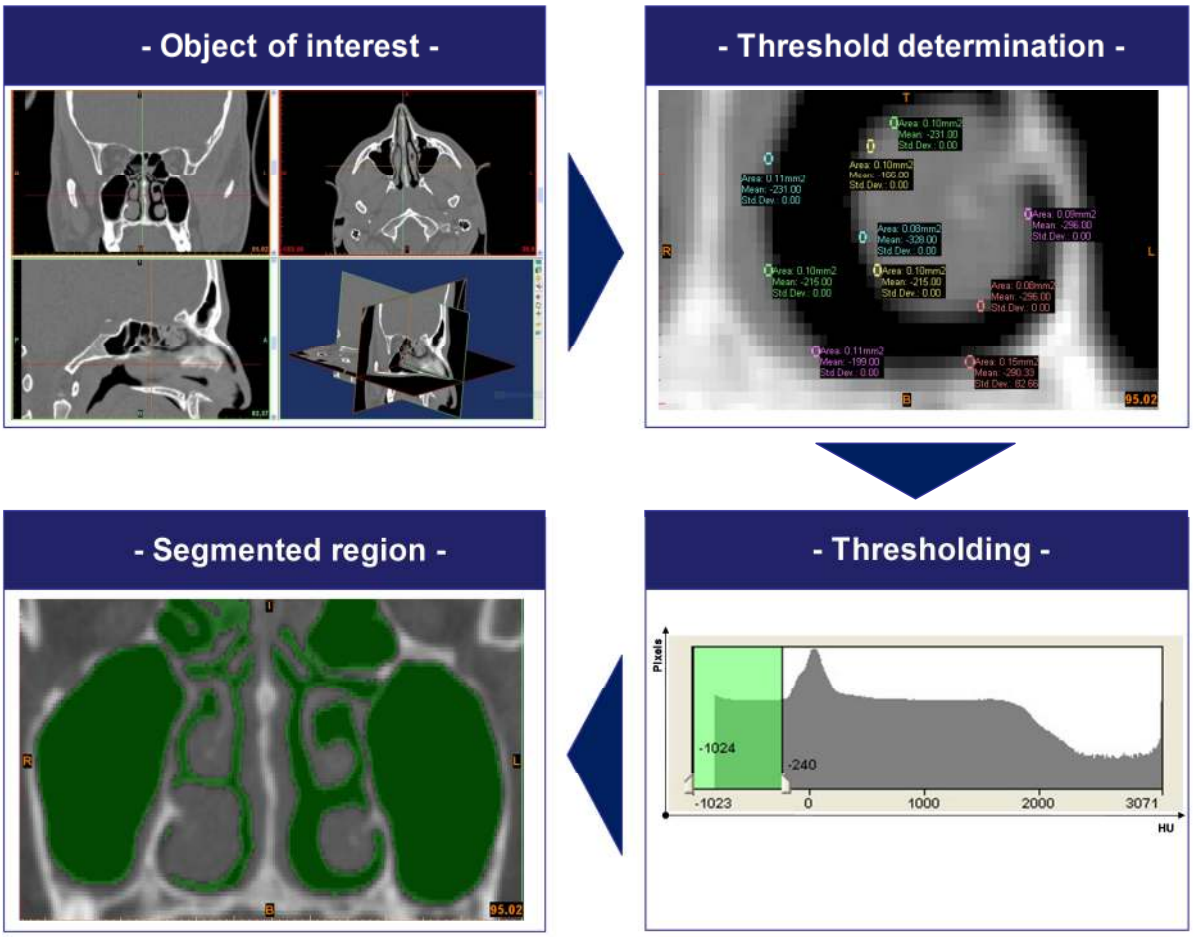

Figure 6-5: Segmentation human nose

To eliminate remaining errors in the segmented result the region-growing algorithm is applied. The region growing method is used additionally to separate regions of interests.
For segmentation, case 3 (1-mm slice thickness and 0.5-mm slice increment; see Fig. 6-6) is the most suitable for determining the contours of the human nose. The defined contour for segmentation is a boundary that differentiates between mucosa and air.

Figure 6-6 depicts the generated 3D models (cases 1–3), which are presented in 3D voxel view. It is obvious to see that the image segmentation and processing process directly influences modeling and design accuracy.

1

Scan parameters	Values
Scanner	Siemens Somatom Definition
Scan direction and position	axial
Field of view (FOV)	17.5 cm²
X-ray dose	120 kV
Slice thickness	5 mm
Slice increment	5 mm
Filter algorithm	H50s
Resolution	512x512
Artifacts	none

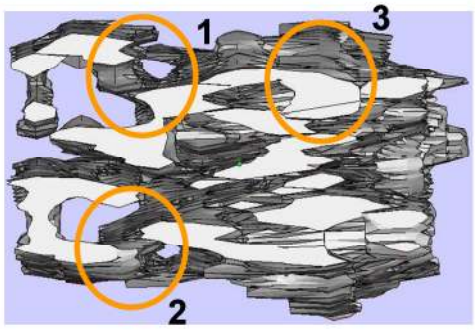

3D nose coronal view

2

Scan parameters	Values
Scanner	Siemens Somatom Open
Scan direction and position	axial
Field of view (FOV)	17.5 cm²
X-ray dose	120 kV
Slice thickness	3 mm
Slice increment	3 mm
Filter algorithm	H50s
Resolution	512x512
Artifacts	none

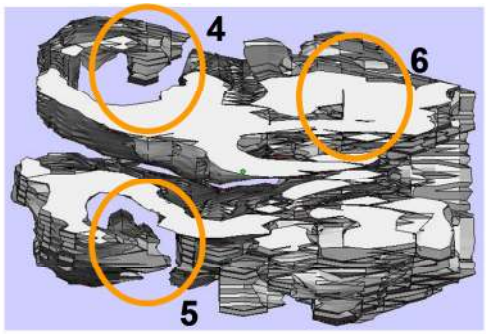

3D nose coronal view

3

Scan parameters	Values
Scanner	Siemens SomatomOpen
Scan direction and position	axial
Field of view(FOV)	17.5 cm²
X-ray dose	120 kV
Slice thickness	1 mm
Slice increment	0.5 mm
Filter algorithm	H50s
Resolution	512x512
Artifacts	none

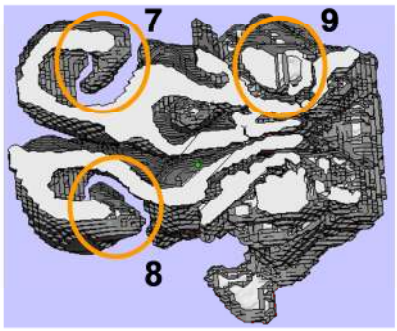

3D nose coronal view

Figure 6-6: 3D reconstruction results

It can be discerned that the 3D model in case 3 shows details that are not visible in cases 1 and 2. Analyzing the results of case 1, it is possible to see that there are bridges connecting unrelated regions, here the concha inferior (circles 1-3), and geometry is thus distorted. In case 2, circles 4 and 5 show well-separated concha inferiors. Circle 6 depicts poorly reconstructed tissues. The reconstruction result in case 3 demonstrates that it is indeed possible to visualize all structures. Here, the concha nasalis and even finer structures are well-reconstructed (circle 7-9).

The insufficient results of case 1 and 2 are influenced mainly by high interpolation failures caused by large slice thickness, large slice increment, and partial volume effects (Chapter 2.1.4.2). The segmentation result of case 3 is an appropriate visualization of the human nose.

The 3D reconstruction quality of applied cases suggests that 1-mm slice thickness and 0.5-mm slice increment are well suited parameters for reconstructing the human nose using 2D tomographic image slices for transference into a 3D volume model. After 3D reconstruction, it is obvious that models in cases 1 and 2 have larger slice increments and should not be selected for further processing. Otherwise, unacceptably shaped 3D models will result, due in part to geometry failures arising from too large contour distances. Therefore, parameters of the reconstructed model in case 3 are selected for further processing.

6.2.3 Mesh editing

To process an accurate 3D model, surface meshes are generated with the software Mimics to obtain a volume model. The MC algorithm is used for building a triangulated 3D model (Chapter 2.1.4.1). Triangle reduction and smoothing (STL editing) to reduce file size and improve the mesh of segmented elements are applied as formulated in Chapter 4.2.3.2.

Applying the triangulation parameters determined in Chapter 4.2.3 to case 3, the triangles are reduced from 1,332,808 triangles to 536,328 triangles, which results in a file of 20.096 MB. The result is an appropriate model of the human nose ready for post-processing.

6.3 Medical VR application

The success of a surgical treatment may depend on a reliable presurgical plan. To create a surgical plan for each individual patient, surgeons have to have image information available. In particular, complex anatomy is difficult to understand using 2D gray value images (Chapter 4.1.1). The procedure of separating the nose in its component parts begins with setting up a segmentation mask to highlight all components to be segmented by thresholding and region growing. The reconstructed model of case 3 is edited using the suggested parameters for mesh editing (Table 5-12).

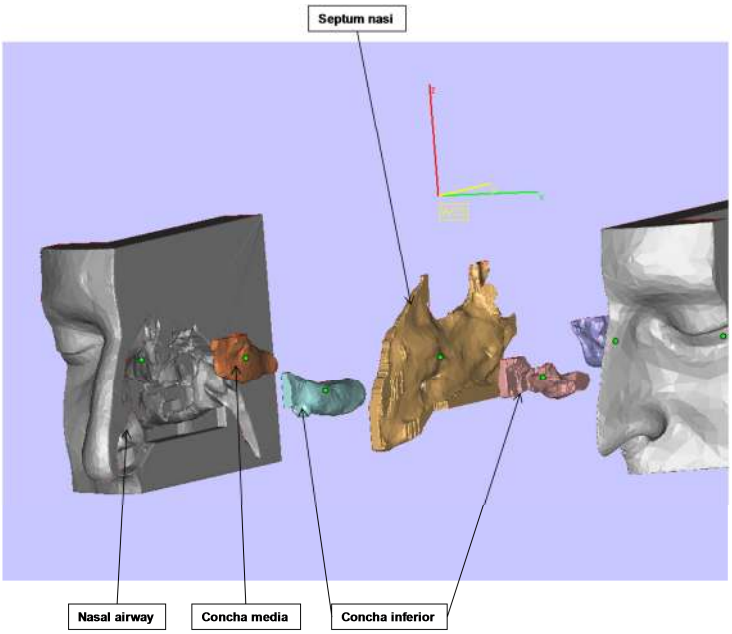

Figure 6-7: Components of 3D nose model

The components, nasal conchae and nasal septum, are separated in a sagittal and coronal direction to realize a component-based animation.

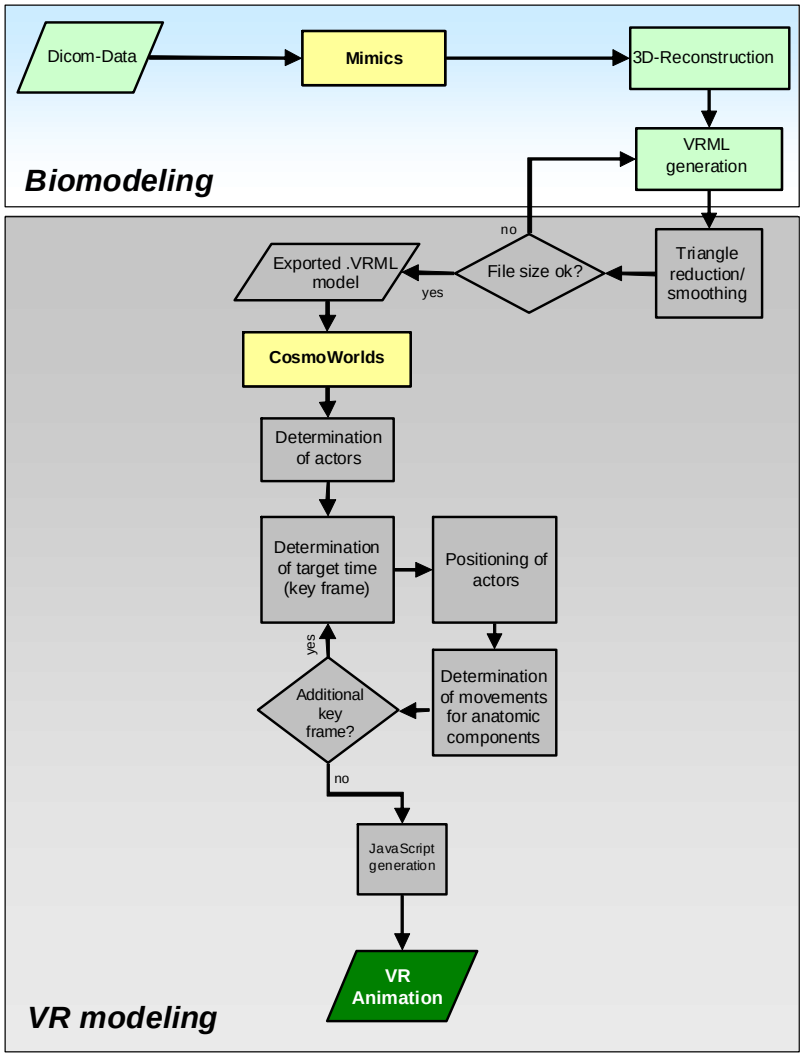

Figure 6-8: VR animation process (Mallepree & Bergers, 2009b)

The optimized model is imported as a .VRML file to CosmoWorlds (Silicon Graphics Inc.). After the setting of actors and frames, the software interpolates the frames occurring in between. After setting the sequence, the animation is defined directly by creating a JavaScript (Fig. 6-8). A script node is defined by at least one EventIn and one EventOut field. A necessary TouchSensor is linked by Route to Script (EventIn). Finally, this script is integrated by using an URL to control the .VRML file.
The defined .VRML model is visualized in stereovision using the VR visualization software VRED (VREC GmbH, Darmstadt). Stereovision glasses are used to display the model in 3D.

The generated nose model consists of 59,000 triangles and its file size is defined to 2,400 Kbyte. The animation procedure generated allows interacting and exploring the 3D model from any geographical position.
The representation of the applied procedure is depicted in Figure 6-9. Here, it is possible to convert 2D image slices into a component-based 3D animation in VR.

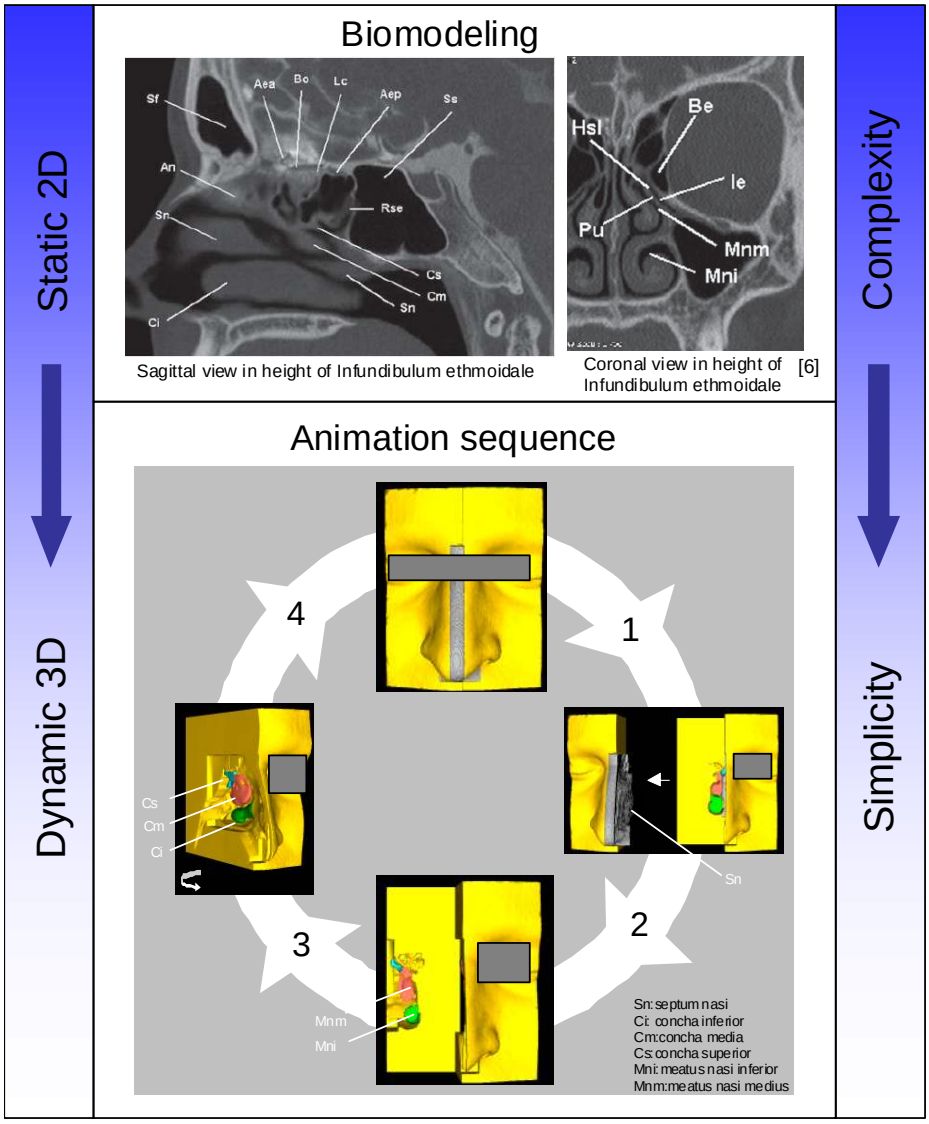

Figure 6-9: Animated components (Mallepree & Bergers, 2009b)

Components that are difficult to visualize, such as the S_n, C_i, C_m, C_s, M_{ni}, and M_{nm}, are displayed in an animated sequence (Table 6-2).

Table 6-2: Animation sequence

Sequence	Components	Plane
1	Complete nose	Coronal
2	Setum nasi (Sn)	Sagittal
3	Meatus nasi: inferior (Mni), medius (Mnm)	Coronal
4	Nasal cavitiy, nasal conchae	Sagittal

First, the animation procedure provides a coronal view of the nasal conchae. Second, after the inspection of the nasal conchae and S_n, a sagittal view is given to explore the nasal conchae in length. The user may change the given direction of view at any time during the animation, thus permitting individual exploration interactively.

The complexity of 2D images is reduced by dynamic 3D animated component-based parts of the human nose. Here, the aim is to establish a process for the generation of animated anatomical models to provide surgeons with the best possible image information for presurgery planning. Moreover, the introduced procedure enables surgeons to communicate with each other, from different sites. This is made possible by analyzing the provided .VRML file in a standard internet browser that includes a .VRML plug-in. An additional field of use can be seen in both medical teaching and patient information. For example, medical students would be able to examine complex anatomical structures interactively. Guided by an animation, they would become familiar with specific sections, which are particularly difficult to find. Surgeons would be able to communicate with patients and family members, especially in situations where diseases and planned treatments, respectively, are difficult to explain using only 2D gray value images. Preoperative and postoperative situations could also be discussed more easily. Overall, due to the work of Hu (2005), 3D visualizations play a significant role in planning surgical intervention by reducing planning time (by approx. by 30 %), compared to 2D images. With the work shown here, it can be concluded that the procedure has potential for use as both a virtual planning and research instrument to reduce the time for understanding the morphology and physiology of such complex parts as the human nose.

6.4 Medical RP application

The generation of an RP model that represents the human nose follows the formulated demands of Chapter 3. The analyzes of Chapter 4 form the basis for the fabrication. In the following, the generation of an exemplary RP model is presented to demonstrate its general ability to produce complex geometries, such as the human nose. The complete fabrication process is based on the MPP shown in Chapter 4. The geometric information, which is derived as an .STL file, is used to set up tool paths for CNC milling. Then, a quasi-additive RP fabrication procedure is applied. Due to experimental setup restrictions, the complete model is derived at a scale of 3:1 and is separated in the coronal direction into 21 slices. The size of each slice is shown in Figure 6-10.

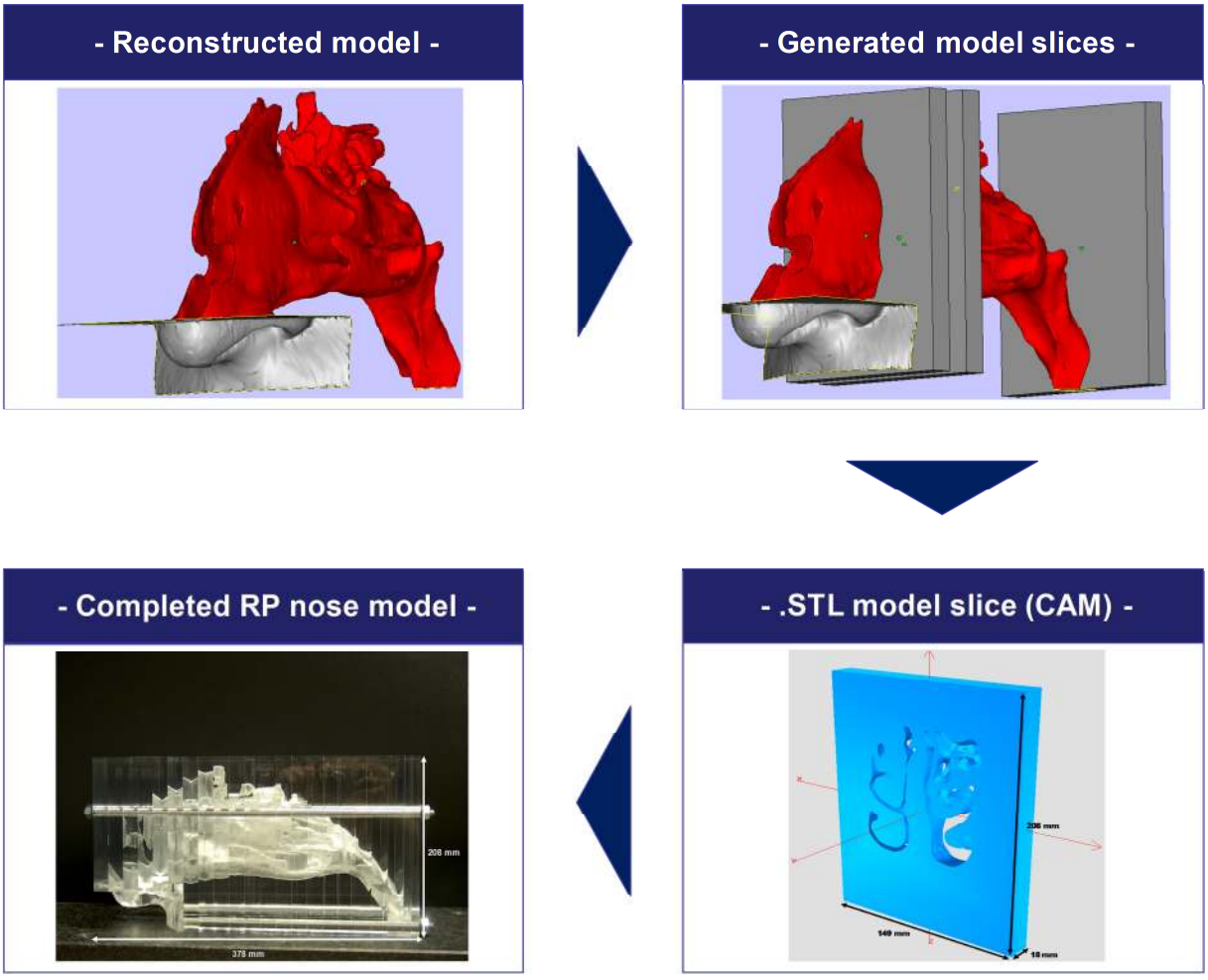

Figure 6-10: Generation of RP nose model

In modeling the human nose, a steady triangulated inner surface is of major importance. The inner surface represents a functional surface. When testing the nasal flow experimentally, the flow behavior should not be influenced by the model itself. The inner surface of the model should represent the original surface structure as truly as possible, with respect to accuracy and smoothness. Once the surface is triangulated and transferred from the 3D reconstruction process to succeeding processes for editing (e.g., cutting, triangle reduction) the surface is

re-triangulated. Re-triangulation leads to another step of approximation. In the present process, the inner surfaces are triangulated once in the step of 3D reconstruction. To achieve the highest possible accuracy, the parameters evaluated in Table 5-12 are used and the inner surface is triangulated once.

To provide a functional model that is reversibly joined, a modular modeling concept is developed. Such a concept requires that the complete model is built of joined slices to realize a preoperative and postoperative situation (Fig. 6-11). The test analyzes shown in Chapter 5.5 demonstrated that all slices can be joined without loss of accuracy.

The procedure applied for rebuilding the human nose should enable an analysis of variances related to pre- and postoperative situations by a model, rapidly and without the necessity of rebuilding a complete model. The modular concept permits mounting measuring instruments for flow analysis directly on slices, which are representative of a specific anatomic situation of interest (pressure, speed, etc.). In cases in which a postoperative situation should be represented by a model, new CT scans have to be made, a 3D model reconstructed, and considered regions need to be exchanged. Running this concept is only possible if the postoperative model fits exactly into the original model. This requirement is related to both the virtual .STL model as well as the physical slices that need to be fabricated in the milling process; a process providing exact repeat accuracy is needed for this. Repeat accuracy is determined by the evaluated parameters for scanning, triangulation, and milling.

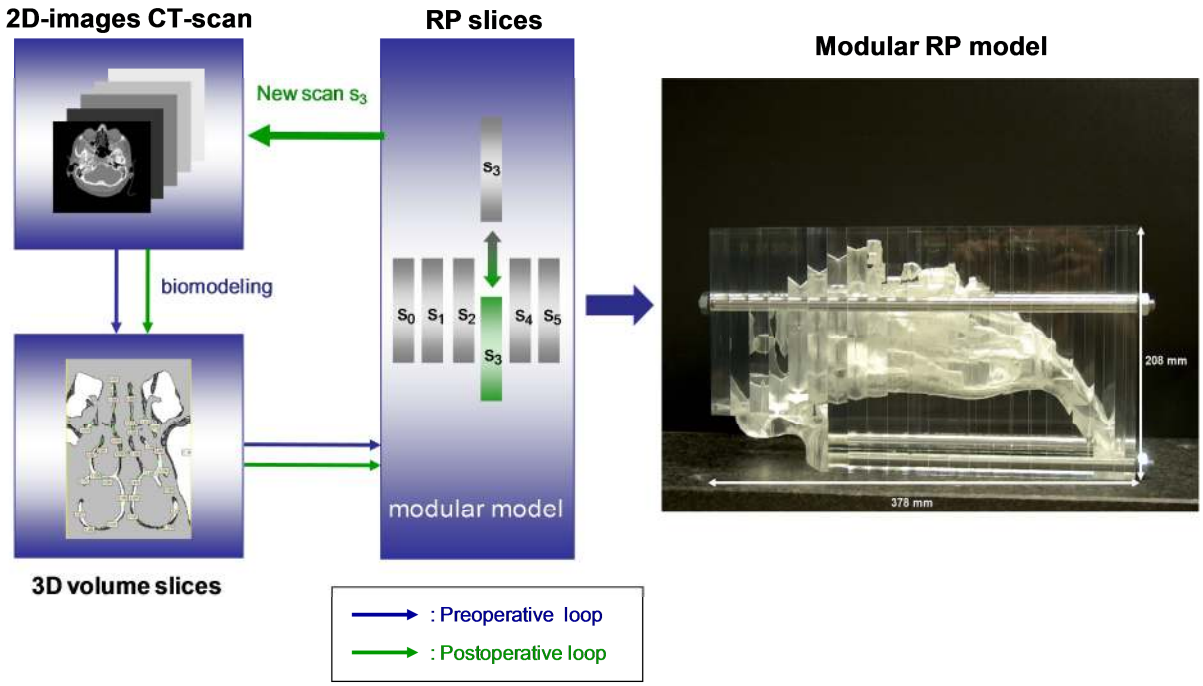

Figure 6-11: Modular RP concept

As depicted in Figure 6-11, a model is built for example using S_0… S_5 slices in a preoperative loop, prior to surgery. A postoperative loop will be conducted if a treatment has been done by

means of exchanging only the focused slice s_3. Hence, only one slice has to be rebuilt and not the complete model.

As shown additionally in Figure 6-11, the model is fabricated successfully meeting the requirements for experimental inspections. In terms fulfilling transparency requirements, the model is built using the evaluated milling parameters shown in Chapter 5.4.3 (Table 5-15).

An experimental set-up passes water through the RP nose model to verify its suitability for nasal flow experiments.

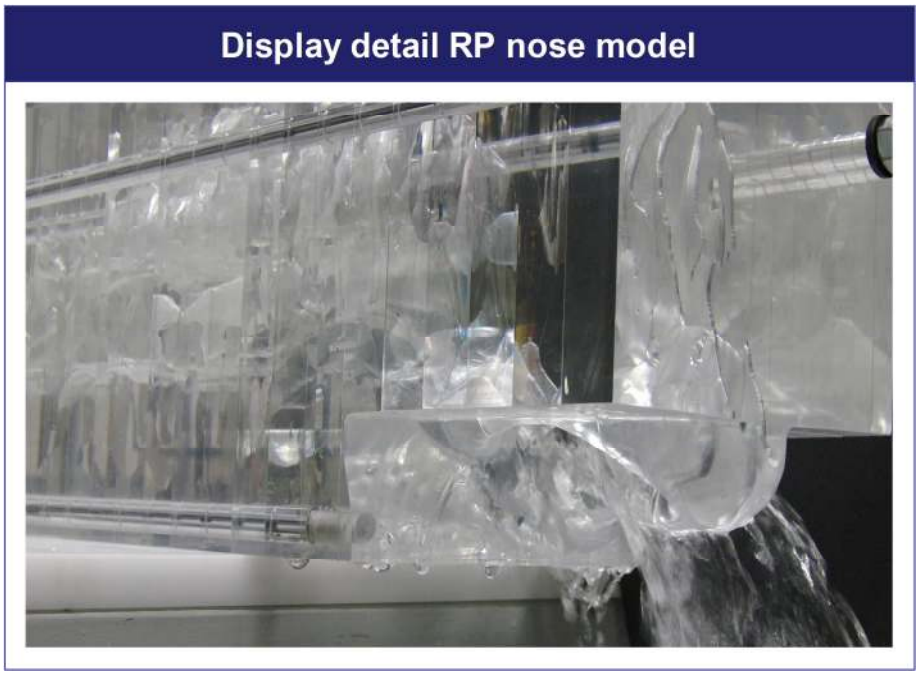

Figure 6-12: Verification: RP nose model

As demonstrated by Figure 6-12, flow-through with water is possible and leakages are not detected.

6.5 Time analysis

The applicability of a VP and RP process is strongly related to processing time. This is not limited to manufacturing time only. It is essential to consider overall processing time in generating medical models by RE and biomodeling processes. To date, a process design that uses as few process steps as possible to produce high-quality medical models in the shortest possible time span, is missing. Thus far, various approaches exist for medical model generation (Chapter 3). The MPP concept enable running an optimal sequence with few

process steps in order to generate medical models of highest quality in the shortest span of time.

Here, the MPP is compared with a process design that produces triangulated 3D models without verified parameters (trial-and-error process). The MPP uses its verified parameters and can be executed in the two steps of biomodeling and application without backward steps for verification. Figure 6-13 shows the steps needed to produce a VR model of the nose. In the present case, typical anatomical features (five features as nasal conchae, nasal septum, are reconstructed; Chapter 6.3).

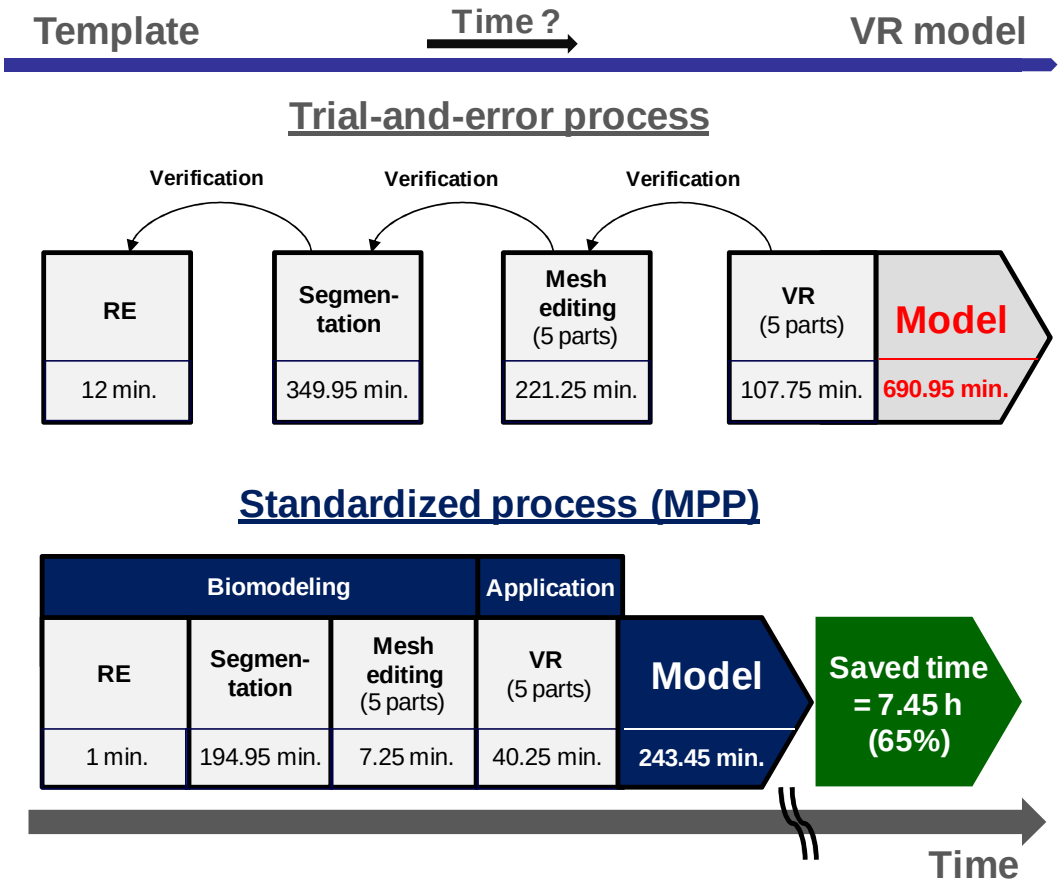

Figure 6-13: Time analysis: VR nose model

The time required for generating the VR nose model amounts to 243.45 minutes compared to 690.45 minutes required for the process that contains needed backward-steps. This is an improvement of 65 %, or saved time of 7.45 hours (Fig. 6-13). This acceleration is a result of avoiding loops that are normally necessary for finding the optimal modeling procedure. The best result for an improvement can be seen at the mesh editing process for generating the triangulated surface meshes (96%). When process parameters for modeling are known, the application can be started immediately.

The generation of the RP nose model (Fig. 6-10) is also based on the MPP. As Figure 6-14 demonstrates, the MPP is reduced to three main steps compared with trial-and-error processing.

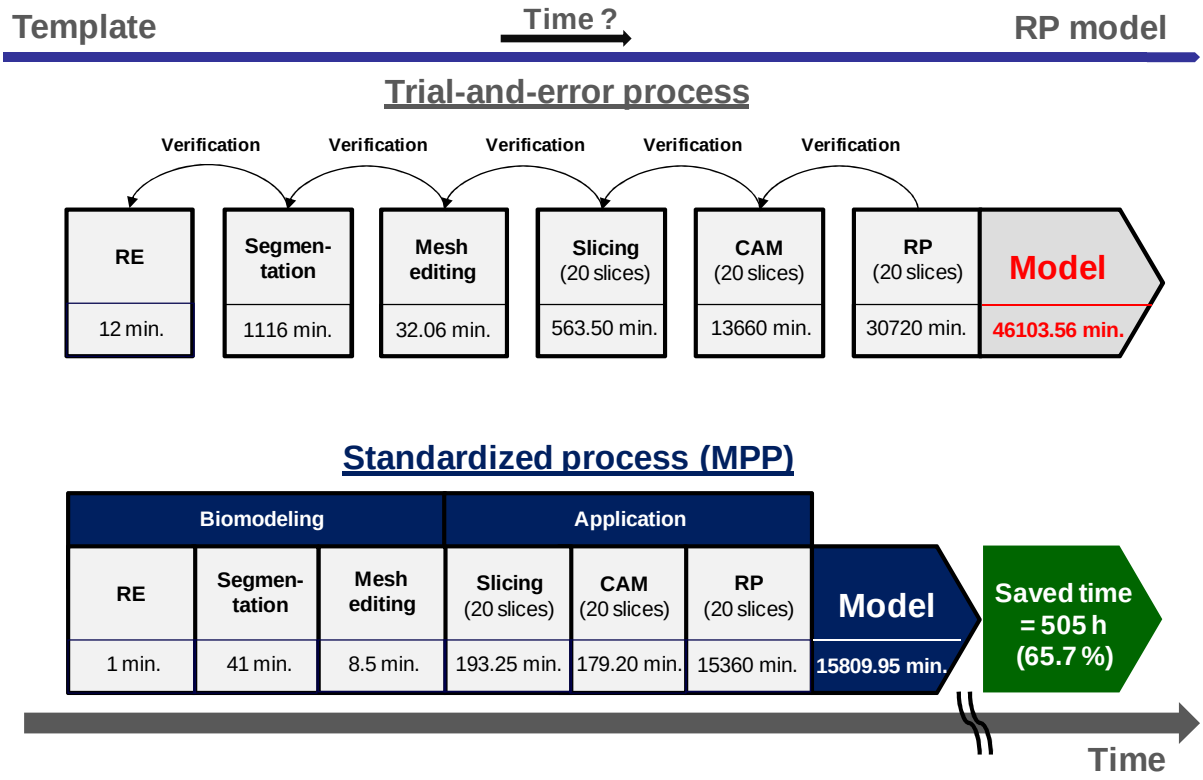

Figure 6-14: Time analysis: RP nose model

The complete processing time of a nose model with 20 model slices is 256 hours (15,360 min.) compared to 512 hours (30,720 minutes) required for the process that contains needed backward-steps. Thus, processing time for the generation of the RP model can be reduced by 505 hours (65.7 %) compared with the processing time in which backward steps for verifications are needed. Specifically, the process of biomodeling could be reduced by 18.49 hours (95 %) and the process of application by 486.85 hours (64 %). The main reason is due to the absence of backward steps that are required in the trial-and-error process. When running the procedure with backward steps, verifications are required to obtain the information as needed. This suggests that various models need to be analyzed, in order to find an optimal sequence.

The MPP presented here permits evaluated parameters to be used in an evaluated software environment to realize a steady process flow. The time profit realized by the MPP implies that variants of a model can be generated even faster by the modular model building. If a variant is needed for the present case (e.g., concha nasalis) the specific slices can be exchanged (Fig. 6-11). A typical scenario evaluated is the exchange of five slices that represent the concha nasalis media. In this case, a second model needs to be reconstructed but only five slices need to be manufactured. Processing time is 122.4 h, which is a reduction of 140.6 hours (46.54 %) because it is not necessary to reproduce the complete model as is the case in a process including backward-steps.

7. Example of use: The human hip

Worldwide, the rate of total hip arthroplasties is approx. 2.8 million (Diehl, 2003). Over the last 13 years, the rate of primary total hip arthroplasties in the United States per 100,000 persons increased by approx. 50% (Kurtz et al., 2005). Approximately 200,000 total hip replacements, 100,000 partial hip replacements, and 36,000 revision hip replacements were performed in the United States in 2003 (Zhan et al., 2007). In Germany, 200,000 hip replacements are performed annually (Hüter-Becker and Dölken, 2005) and the number of reoperations is increasing each year.

In orthopedic surgery, the success of an endoprosthetic reconstruction depends on the precise realization of the operative procedure. The final result is referred to an optimal fit of the prosthesis. Therefore, an exact preoperative planning is of major importance. In order to fulfill the requirements for hip replacement surgeries, a detail preoperative planning is necessary. While presurgery planning is time-consuming, the use of 3D models can decrease planning time in surgery by about 30 % (Hu et al., 2005). Therefore, the MPP presented herein is applied for generating 3D models of the human hip to support planning virtual and physical hip models.

7.1 Medical background

The hip bone is a large, irregularly shaped bone, positioned in the center of the human body. It forms the sides and anterior wall of the pelvic cavity. Figure 6-1 shows that the hip bone consists of three parts, the ilium, ischium, and pubis (Gray, 2000). The union of the three parts takes place in and around a large cup-shaped articular cavity, the acetabulum, which is situated near the middle of the outer surface of the bone (Gray, 2000). The ilium extends upward from the acetabulum. The ischium is the lowest and strongest part of the bone; it is located downward from the acetabulum. The pubis extends medialward and downward from the acetabulum and articulates in the middle line with the bone of the opposite side; it forms the front of the pelvis (Gray, 2000).

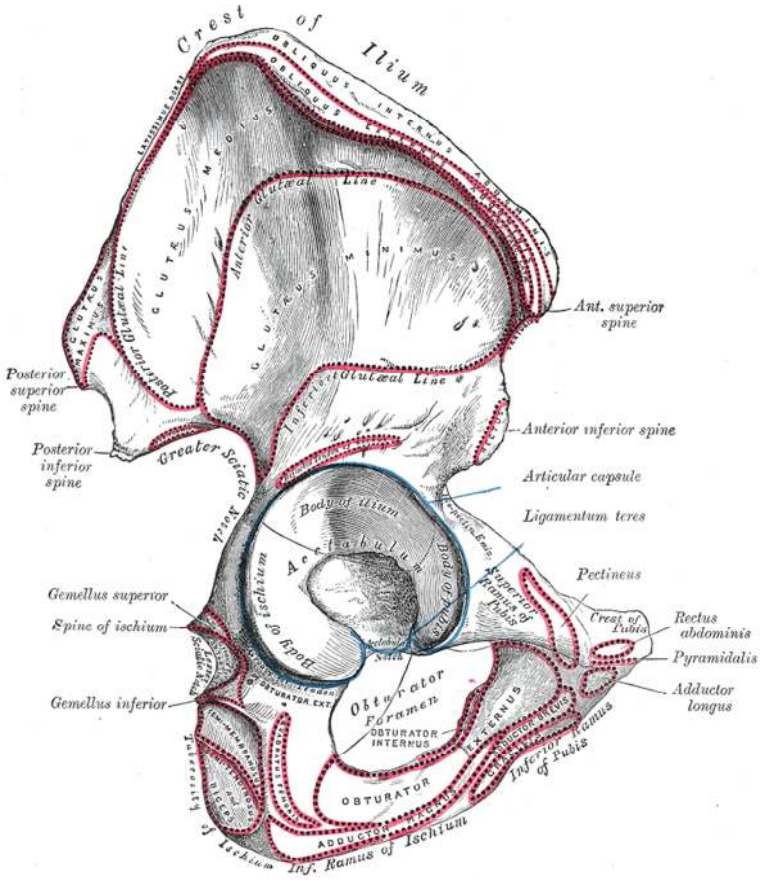

Figure 7-1: Anatomy of the human hip (Gray, 2000)

The thicker parts of the bone consist of cancellous tissue, enclosed between two layers of compact tissue; the thinner parts, at the bottom of the acetabulum and center of the iliac fossa, are usually semitransparent, and composed entirely of compact tissue.
The hip joint is loaded mechanically bearing the weight of the upper body. During walking, running, and jumping nearly the complete body weight is borne by the hip joint.

Due to the increasing number of hip surgeries conducted, the need for geometric information is increasing. On one hand, there is support needed for virtual surgery planning that is conducted using tomographic image data. Virtual 3D models support faster diagnosis and help the formulation of an operation plan. Physical 3D hip models facilitate presurgery planning realistically, in an experimental environment, for example, testing the mounting of different hip prostheses.
The main challenge in reconstructing the human hip is to separate the hip bone from the femur and the pelvis. Moreover, there is a need for accurate reconstruction of the human hip in the shortest possible time, using model material that can withstand load distributions imposed during the testing of implants (Mallepree & Bergers, 2009d). Here, the MPP concept designed in Chapter 4.1 is applied to process virtual and physical 3D models of the hip for presurgery planning.

7.2 Modeling the human hip

The anatomical components needed for 3D reconstruction of the hip anatomy include the identified anatomical landmarks shown in Figure 7-2.

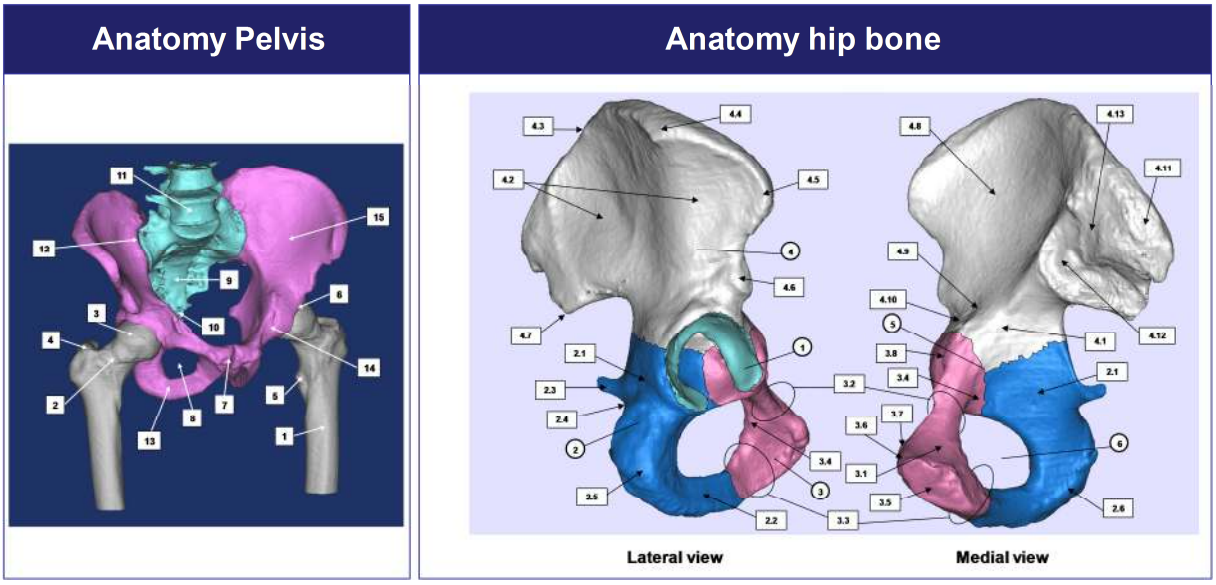

Figure 7-2: 3D Anatomy of the human hip bone (according to Gray, 2000)

Table 7-1: Anatomical elements of the human hip and pelvis

Identifier	Element
1	Acetabulum
2	Os ischii
2.1	Corpus ossis ischii
2.2	Ramus ossis ischii
2.3	Spina ischiadica
2.4	Incisura ischiadica minor
2.5	Tuberositas ischiadica
2.6	Tuber ischiadicum
3	Os pubis
3.1	Corpus ossis pubis
3.2	Ramus superior ossis pubis
3.3	Ramus inferior ossis pubis
3.4	Sulcus obturatorius
3.5	Facies symphysialis
3.6	Crista pubica
3.7	Tuberculum pubicum
3.8	Linea pectinea
4	Os ilium
4.1	Corpus ossis ilium
4.2	Facies glutea
4.3	Crista iliaca
4.4	Tuberculum iliacum
4.5	Spina iliaca anterior superior
4.6	Spina iliaca anterior inferior
4.7	Spina iliaca posterior inferior
4.8	Fossa iliaca
4.9	Linea arcuata
4.10	Tuberositas iliaca
4.11	Spina iliaca posterior superior
4.12	Facies auricularis ossis ilium
4.13	Contact point ligaments
5	Y-gap
6	Foramen obturatum

Understanding the anatomy enables generation of the required tomographic image slices.

7.2.1 Data acquisition

Three different scans were conducted to verify the best possible model accuracy. The quality of images in the image plane (x-y) is determined by the appropriate filter algorithm, which is here B60f (Siemens), and FC30 (Toshiba) (Fig. 7-3).

1

Scan parameters	Values
Scanner	Siemens Somatom VolumeZoom
Scan direction and position	axial
Field of view (FOV)	
X-ray dose	120 kV
Slice thickness	1 mm
Slice increment	1 mm
Filter algorithm	B60f
Resolution	512x512
Artifacts	none

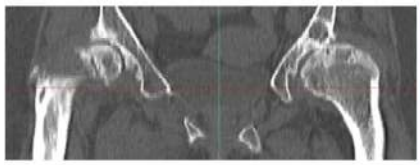

2D view

2

Scan parameters	Values
Scanner	Siemens Somatom VolumeZoom
Scan direction and position	axial
Field of view (FOV)	
X-ray dose	120 kV
Slice thickness	1 mm
Slice increment	1 mm
Filter algorithm	B60f
Resolution	512x512
Artifacts	none

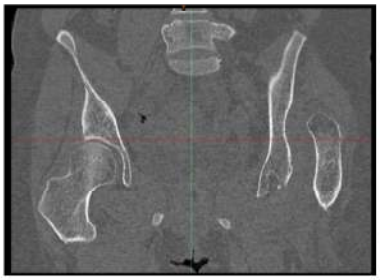

2D view

3

Scan parameters	Values
Scanner	Toshiba-Asteion
Scan direction and position	axial
Field of view (FOV)	
X-ray dose	120 kV
Slice thickness	3
Slice increment	2
Filter algorithm	FC30
Resolution	512x512
Artifacts	none

2D view

Figure 7-3: Acquisition parameters: hip models

The scanning parameters are varied from 1-mm slice thickness and 1-mm slice increment in case 1 to 3-mm slice thickness and 2-mm slice increment in case 3.

7.2.2 Segmentation and 3D reconstruction

CT data are generated by parameters which satisfy the general demands on accuracy as stated in Chapter 4.2.2. In CT image data, air appears with a mean intensity of approximately

–1024 HU, most soft tissue is in the range of –200 to 130 HU, cartilage ranges from 800 to 1000 HU, and bone structures are well above 1000 HU. In order to separate the hip bone from the femur the boundary between bone and cartilage (Fig. 7-4) is set by using the known HU from cartilage and bone.

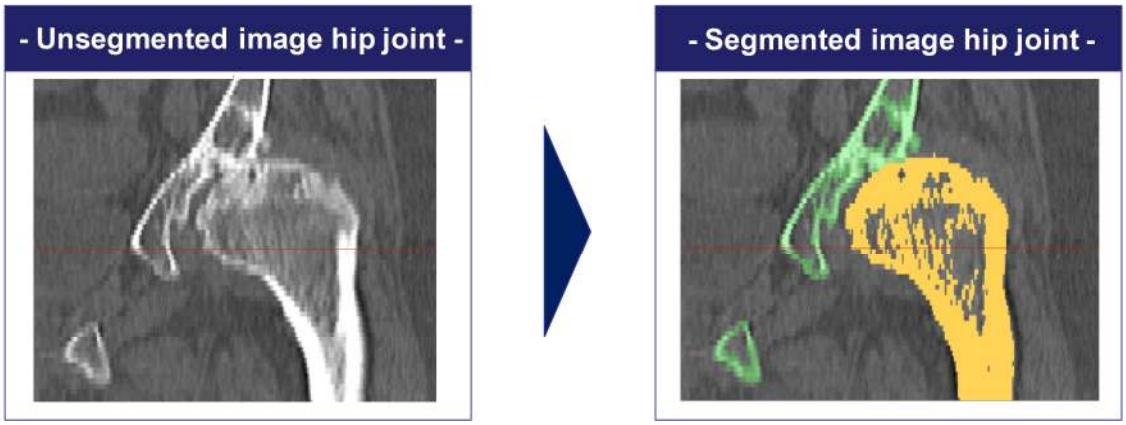

Figure 7-4: Segmentation: hip model 1

By using a slice increment of 1 mm it is possible to define the contours in all three cases. Region growing is used additionally to separate the regions of interest.

7.2.3 Mesh editing

To process high-quality 3D models, threshold-based and region-orientated segmentation results require post processing (Chapter 4.1.1). Three different .STL and .VRML models are generated in order to start a VR and RP application by using the mesh editing parameters as presented in Chapter 4.2.3.2 (Table 5-12).

7.3 Medical VR application

A VR model of the hip enables surgeons to obtain detailed insight of hip anatomy during the planning of complex hip surgery. To provide optimum insight, an exemplary model (case 1) is used for demonstration (Fig. 7-5). The model presented in Figure 7-5, which is used for VR is a .VRML model derived from the editing parameters evaluated in Chapter 4.2.3.2 (Table 5-12).

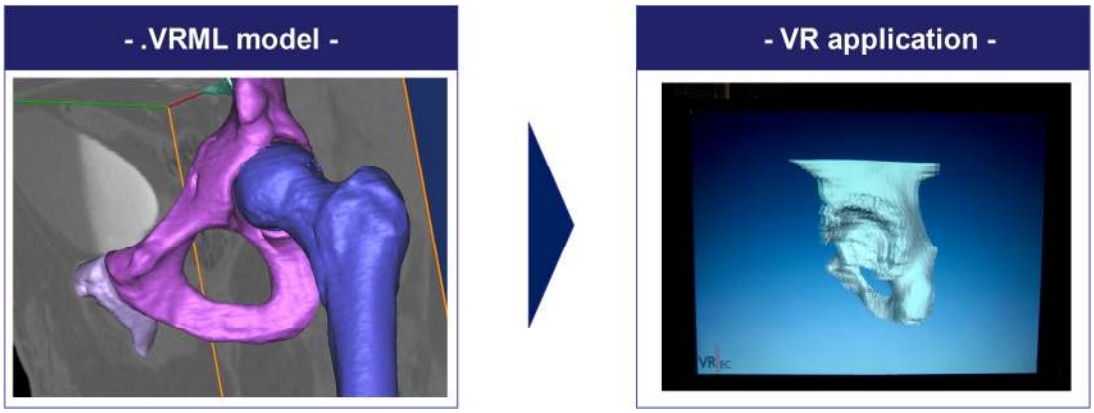

Figure 7-5: VR Hip model

The result is a .VRML file with 86,724 triangles, which results in a file of 4.235 MB. The VR presentation software VRED is applied for stereoscopic display using the generated .VRML file. The animation procedure introduced in Chapter 5.3 could thus be initiated if necessary.

7.4 Medical RP application

For running the quasi-additive RP fabrication procedure, the complete model is derived in 1:1 scale and is separated in five slices as shown in Figure 7-6. The complete .STL file consists of 86,724 triangles, which results in a file size of 4.235 MB.

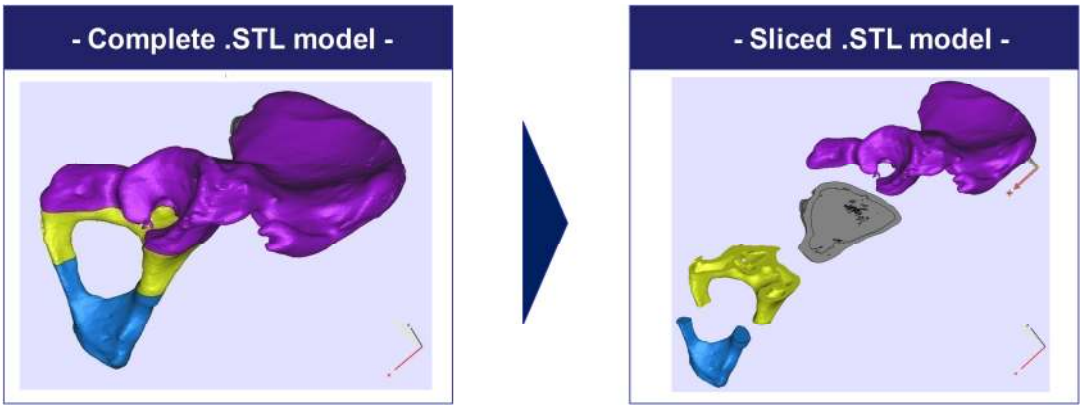

Figure 7-6: RP Slices: hip model

The .STL file slices are then used for running the quasi-additive RP procedure of CNC milling. The complete fabrication process is based on the MP process shown in Chapter 4. Geometric information in .STL file format is used to set up tool paths for CNC milling. In terms of meeting the requirements of accuracy, the model is milled using the evaluated milling parameters shown in Chapter 5.4.3 (Table 5-15). Typical model making material (Necuron) is used for producing the model. Joining is realized using an appropriate model adhesive.

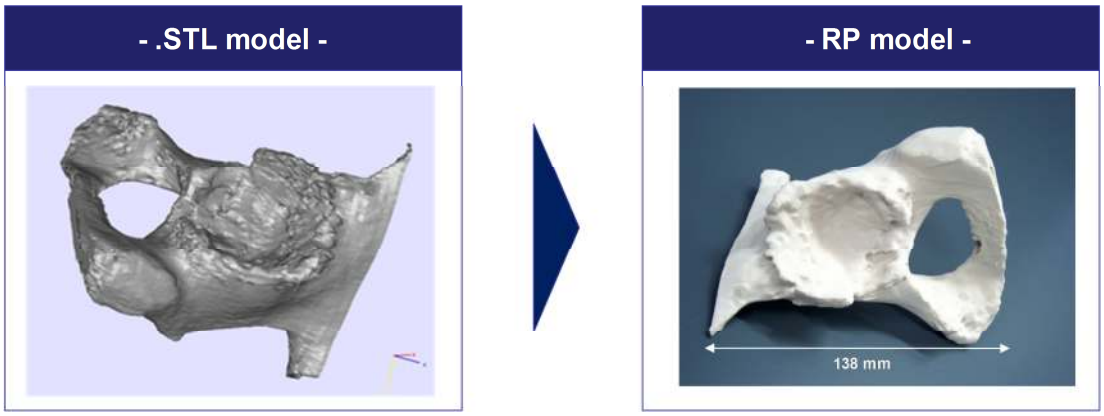

Figure 7-7: RP Hip model

As shown in Figure 7-7, the model is fabricated successfully meeting the requirements for experimental inspections. In clinical praxis various hip models have been used successfully for presurgery planning.

7.5 Time analysis

The generation of the hip model is based on the MPP. The total time for the VR hip modeling amounts to 82.95 minutes when conducting the MPP. However, neglecting MPP parameters leads to a modeling time of 710.95 minutes.

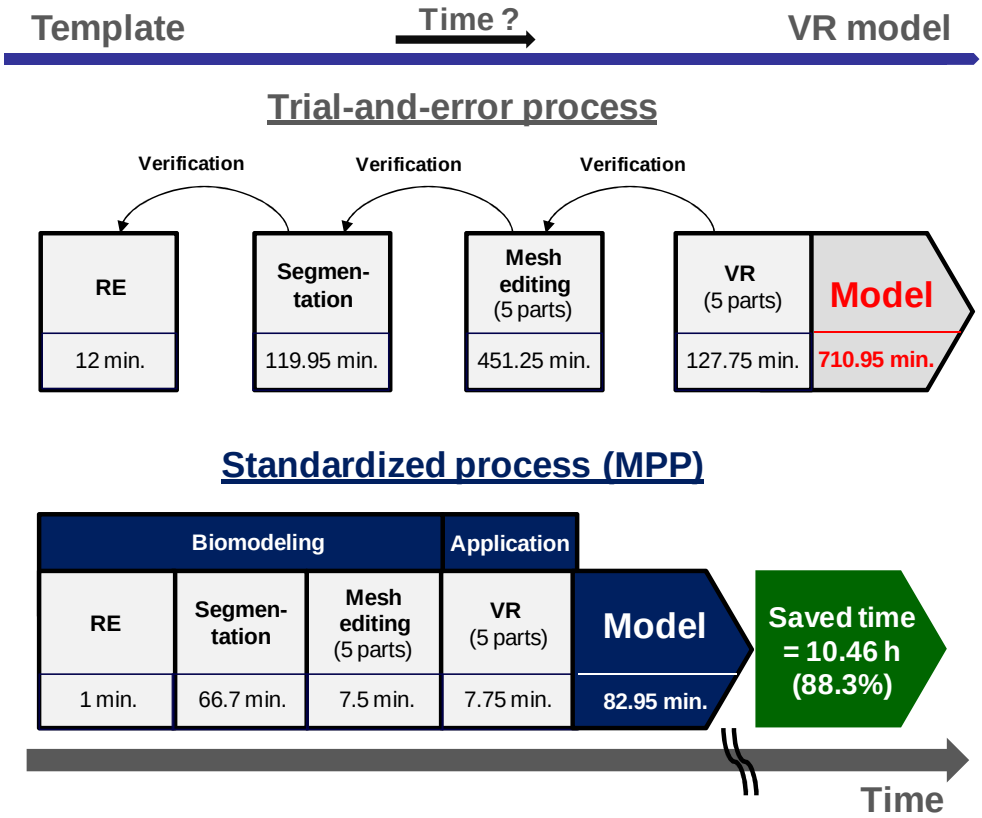

Figure 7-8: Time analysis: VR hip model

This represents a 628 -minute time reduction (88.3%) for the generation of a hip VR model compared to processing without defined process parameters (Fig. 7-8). Compared to the mesh editing in the trial and error process, the mesh editing in the MPP was again, 98.3 % more rapid. The reason for this is the decreased complexity that allows faster modeling in general.

The generation of the RP hip model can also be accelerated. As Figure 7-9 demonstrates the MPP is reduced to three main steps compared with trial-and-error processing.

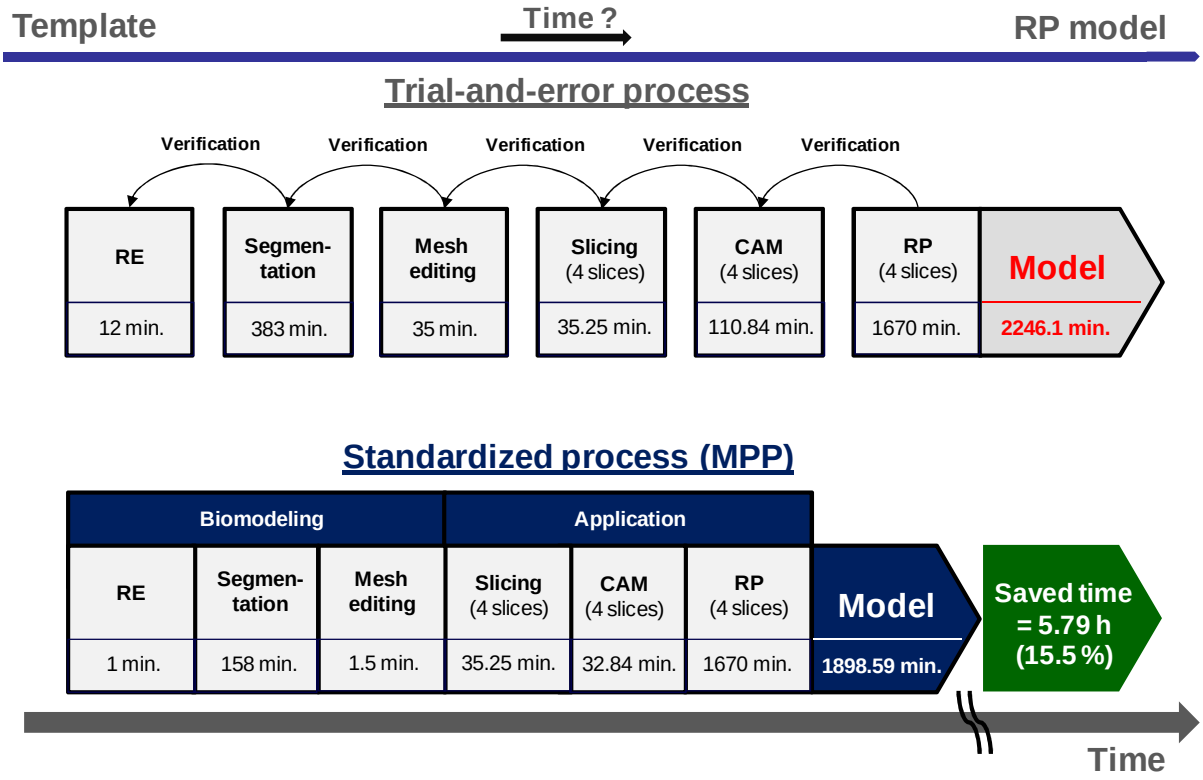

Figure 7-9: Time analysis: RP hip model

The processing time using the MPP for generation of the RP model amounted to a total of 32 hours (1898.59 min.). The trial-and-error process, on the other hand, resulted in a processing time of 37 hours (2246.1 min.). Thus, the MPP results in a reduction of 5.79 hours (15.5 %) compared with the processing time of a trial-and-error process in which backward steps for verifications are needed. Specifically, the process of biomodeling was reduced by 37.30 %. Truscott et al. (2007) reported a time of 48 hours required for the fabrication of a hip model. Comparing the performance (32 hours) achieved with results of fabricating RP hip models to those found in the report of Truscott et al. (2007), a total improvement of 33 % was found. The main reason for this is the absence of backward steps that are normally necessary in the trial-and-error process (Chapter 3). Running the trial-and-error procedure requires that verifications must be done to obtain information as needed. The derivation of various models is frequently required to find the optimal one.

8. Conclusion and outlook

An integrated prototyping process for the derivation of complex medical models is introduced. The use of medical models can support today's medicine by improving diagnosis and surgical planning, teaching and patient information. To withstand the challenges of time and accuracy, a process for generating accurate virtual and physical medical models is needed. The introduced process offers the possibility to derive virtual and physical models for biomedical engineering applications.
Reviewing the current situation of medical VP and RP applications, limitations were found related to the influential variables of data acquisition, data processing, VR use, and RP manufacturing. Moreover, a classification or framework for embedding VP and RP applications in medical applications is still missing.

An integrated prototyping concept (MPP) is introduced for embedding VP and RP in biomedical applications. For the first time, a medical classification is set up that assigns VP and RP to possible applications in medicine, thus supporting the use of a needed prototyping application for a particular case of use.

Data processing and 3D modeling of complex anatomical structures from CT image data were investigated and discussed in detail. Finally, parameter analyses were evaluated to derive optimal parameters needed for preparing 3D models for VP and RP processing in medicine. To obtain accurate volume models, careful attention must be given to selecting scan parameters. Considering the 3D reconstruction quality of the applied cases it was found that parameters of 1-mm slice thickness and 0.5-mm slice increment were well suited for reconstructing complex anatomies using 2D tomographic image slices for transference into a 3D volume model when scanning in the longitudinal direction. Further, when scanning in the transverse direction, a slice thickness of 1 mm and a slice increment of 1 mm was found suitable. Anisotropic voxels, which mostly lead to reduced resolution in the z-direction, can thus be avoided. Generally, overlapping reconstruction processing helps generating isotropic voxels, which in turn produce 3D models without artifacts. The accuracy analysis performed reveals that optimal results in 3D reconstruction may be achieved if the slice increment is one half of the selected slice thickness, when a multi-detector CT scanner is used. This leads to an overlap of 50 %. Further, the shape of the slice profile was found to have an effect on model accuracy. There is evidence that the slice thickness should be set ≤0.4 mm. Summarizing from the accuracy analysis, the present investigation is the first to examine tomographic scanning as decisive factor for inaccuracy of medical RP models.
The optimal selection of an appropriate segmentation filter (curvature flow) leads to less-deviated models when noisy CT images need to be smoothed. Overall, scan parameters

determine a model's final accuracy rather than the manufacturing procedure or the mesh editing used. In mesh editing, smoothing should be conducted carefully to improve the MC algorithm's meshing result.

To provide both a virtual planning instrument to reduce the time for understanding the anatomy of complex anatomies, a medical VR process is introduced. The process can be used for the generation of animated anatomical models to provide surgeons with the best possible image information for presurgery planning.

For fabricating transparent medical models, which are characterized by anatomically shaped free-form surfaces, milling parameters were evaluated. An optimized interplay of cutting speed and feed rate during smoothing allows generation of transparent medical models, even when milling cutters with small diameters are used.

The human nose is an example of a complex anatomical geometry, which has been an object of scientific research interest for several years. One of the applications introduced here uses the developed MPP concept as basis for a procedure that generates animated medical models in a VR environment. Although, attempts are being made to reconstruct the human nose as an experimental RP model, a process for accurate reconstruction as a transparent RP model is still missing. The MPP concept allows fabricating individual models of the human nose with a high level of accuracy and transparency. Thus, the concept is amenable to application in various experimental studies – the model is modularly built of exchangeable slices. Finally, temporal analysis revealed major time improvements in modeling complex anatomical models compared to approaches without optimized process sequences and approved parameters. The process time for displaying the human nose in a VR environment was reduced by 65%. The fabrication time of a transparent nose model was reduced by 65.7%.

The prototyping of the human hip was the second example used. The results of this particular example emphasized the strengths of the medial prototyping process in preparing hip models for presurgery planning. Here, accuracy was enhanced considerably. In addition, the time required for virtual model display in a VR environment was reduced by 88.3% and time for fabrication reduced by 15,5% in comparison to the state-of-the-art. RP hip models can provide assistance as a surgical planning tool in complex cases, especially in improving surgical results and implant stability.

Thus, the accuracy and time of model generation is improved, thereby establishing a defined process for medical model generation. This is the first demonstration of a procedure for processing animated VR models and transparent RP models of the human nose using biomedical engineering. Tested parameters guaranteeing repeat accuracy were applied. Considering the novel findings of broad improvements in accuracy and time, a new field of research is emerging, serving both virtual surgery applications and physical implant generation. Further improvements of model accuracy will contribute to validity of results and thus serve medical applications in VP (e.g., CFD simulation) and RP (e.g., presurgery planning).

The MPP developed in this work can be viewed as an initial approach for launching international standards of prototyping technologies in medicine.

References

Alberti, C. (1980) Three-dimensional CT and structure models. British Journal of Radiology 53:261-262

Assmann, O. (2003) Herstellung hochgenauer Prototypen mittels Fräsen als quasi-generativem Rapid Prototyping Verfahren. Dissertationsschrift Universität Duisburg-Essen

Azmi, A, A.Z. Latiff, and A. Johari (2004) Methyl-methacrylate cranioplasty. Medical Journal of Malaysia 59-3:418-421

Bade, R., F. Ritter, and B. Preim (2005) Usability comparison of mouse-based interaction techniques for predictable 3d rotation. In: Smart Graphics. 138-150. Springer-Verlag Berlin, Heidelberg, New York

Bankman, I.N. (2000) Handbook of medical imaging: processing and analysis. Academic Press, San Diego, USA

Barker, T.M., W.J.S. Earwaker, and D.A. Lisle (1994) Accuracy of stereolithographic models of human anatomy. Australasian Radiology 38:106-111

Barlier, C. and D. Gasser (1995) Stratoconcept an original method for rapid prototyping. International Journal of CADCAM and Computer Graphics 14

Bartz, D. (2005) Visual computing for medicine. Habilitationsschrift Universität Tübingen

Beneke, F., M. Metzen, and D. Bergers (2003) Study of a process chain for the use of medical graphic data in technical applications, Materialise Archives; Leuven

Bennamoun, M. and G.J. Mamic (2001) Object recognition: Fundamentals and case studies. Springer-Verlag Berlin, Heidelberg, New York

Bergers, D. (2009a) Rapid und Virtual Prototyping, Skriptum, Produktionstechnologie und Produktentwicklung, Universität Duisburg-Essen

Bergers, D. (2009b) Mess- und Prüftechnik, Skriptum, Produktionstechnologie und Produktentwicklung, Universität Duisburg-Essen

Bergers, D. and T. Mallepree (2010) Advanced rapid prototyping in medicine. Rapid Prototyping Journal (submitted)

Bergers, D., Lamprecht, J., Montag, M., and F. Peters (2010) Klinische und experimentelle Untersuchungen zur Morphologie und Dynamik des Nasen-Lumens und deren Einfluss auf Atemströmung und Klimatisierung der Atemluft. Abschlussbericht Deutsche Forschungsgemeinschaft, Bonn

Berlage, T. (1997) Augmented reality for diagnosis based on ultrasound images. In: CVRMed-MRCAS'97 - First International Joint Conference on Computer Vision, Virtual reality and Robotics in Medicine and Medical Robotics and Computer Assisted Surgery, Troccaz, J., Grimson, E., Mösges, R. (Eds.), Springer-Verlag Berlin, Heidelberg, New York, pp. 253-262

Bertsche, B. and H.J. Bullinger (2007) Entwicklung und Erprobung innovativer Produkte – Rapid Prototyping. Springer-Verlag Berlin, Heidelberg, New York

Bowers, M.E., E. Trinh, G.A. Tung, J.J. Crisco, B.B. Kimia, and B.C. Fleming (2009) Quantitative MR imaging using "LiveWire" to measure tibiofemoral articular cartilage thickness. http://www.materialise.com (Mimics case study) (Last access 12/2009)

Böge, W. (1995) Das Techniker Handbuch. Vieweg Verlag, Braunschweig/Wiesbaden

Bray, N. (2004) Notes on mesh smoothing. http://mgarland.org/class/geom04/material/smoothing.pdf (Last access 12/2009)

Bundesministerium für Bildung und Forschung (BMBF) (2007) Aktionsplan Medizintechnik 2007-2008, Online-Dokument: http://www.bmbf.de (Last access 10/2008)

Bullinger, H.J. and W. **Bauer** (1994) Strategische Dimensionen der Virtual Reality; in: Proceedings IPA/ IAOForum: Virtual Reality ´94 - Anwendungen & Trends; o. Hrsg. Springer-Verlag Berlin, Heidelberg, New York

Bushberg, W., J.A. Seibert, and E.M. Leidholdt (2002) The essential physics of medical imaging. Lippencott Williams & Wilkins, Philadelphia, USA

Cai, Y.Y., C.K. Chui, X.Z. Ye, J.H. Anderson, K.M. Liew, and I. Sakuma (2004) Simulation-based virtual prototyping of customized catheterization devices. Journal of Computer and Information Science in Engineering 4:132-139

Choi, J.Y., J.H. Choi, N.K. Kim, Y. Kim, J.K. Lee, M.K. Kim, J.H. Lee, and M.J. Kim (2002) Analysis of errors in medical rapid prototyping models. International Journal of Oral and Maxillofacial Surgery 31:23-32

Chong, C.K., C.S. Rowe, S. Sivanesan, A. Rattray, R.A. Black, and A.P. Shortland, (1999) Computer aided design and fabrication of models for in vitro studies of vascular fluid dynamics. Proceedings of the Institution of Mechanical Engineers, Part H: Journal of Engineering in Medicine 213:1-4

Chung, S.K., Y.R. Son, S.J. Shin, and S.K. Kim (2006) Nasal airflow during respiratory cycle. American Journal of Rhinology. 20:379–384,2006.

Conrad, K.J. (2006) Taschenbuch der Werkzeugmaschinen. Fachbuchverlag Leipzig (Carl Hanser Verlag), München, Wien

Croce, C., R. Fodil, M. Durand, G. Sbirlea-Apiou, G. Caillibotte, J.-F. Papon, J.-R. Blondeau, A. Coste, D. Isabey, and B. Louis (2006) In vitro experiments and numerical simulations of airflow in realistic nasal airway geometry. Annals of Biomedical Engineering. 34:997-1007

De Zélicourt, D., K. Pekkan, H. Kitajima, D. Frakes, and A.P. Yoganathan (2005) Single-step stereolithography of complex anatomical models for optical flow measurements. Journal Biomechanical Engineering 127:204-207

Deskproto (2006) Online Resource: www.deskproto.com (Last access 12/2009)

Diehl, K. (2003) Ihre Neue Hüfte. Hüftprothese.fh pp. 8. http://www.orthopaeden-zentrum.de/files/op/hueftprothese.pdf (Last access 12/2009)

DIN 8580:2003-09 (2003) Fertigungsverfahren - Begriffe, Einteilung. Beuth-Verlag, Berlin

DIN 1319-3 (1996) Grundlagen der Meßtechnik - Teil 3: Auswertung von Messungen einer einzelnen Meßgröße, Meßunsicherheit. Beuth-Verlag, Berlin

DIN 4762 (2008) Oberflächenrauheit - Begriffe, Einteilung. Beuth-Verlag, Berlin

Domininghaus, H. (2007) Kunststoffe: Eigenschaften und Anwendungen. Springer-Verlag Berlin, Heidelberg, New York

D'Urso, P.S., T.M. Barker, W.J. Earwaker, L.J. Bruce, R.L. Atkinson, M.W. Lanigan, J.F. Arvier, and D.J. Effeney (1999) Stereolithographic biomodelling in cranio-maxillofacial surgery: a prospective trial". Journal of Cranio-Maxillo-Facial Surgery. 27:30-37

Eccles, R. (2001) Nasal airflow in health and disease. Acta Oto-Laryngologica, 120:580-595

Eufinger, H., M. Wehmöller, E. Machtens, L. Heuser, A. Harders, and D. Kruse (1995) Reconstruction of craniofacial bone defects with individual alloplastic implants based on CAD/CAM manipulated CT-data. Journal of Cranio-Maxillo-Facial Surgery 23:175-181

Falk, A., S. Gielen, and L. Heuser (1995) CT data acquisition as a basis for modern diagnosis and therapy in maxillofacial surgery. International Journal of Oral and Maxillofacial Surgery 24(1):69-75

Finck, M., D. Hänel, and I. Wlokas (2007) Simulation of nasal flow with lattice boltzman methods. Computers in Biology and Medicine 37:739-749

Friedhoff, J. (1997) Aufbereitung von 3D-Digitalisierdaten für den Werkzeugbau, Formenbau und Modellbau. Vulkan Verlag, Essen

Gebhardt, A. (2003) Rapid Prototyping Werkzeuge für die schnelle Produktentwicklung. 2. Auflage, Hanser Verlag, München

Gebhard, A. (2007) Generative Fertigungsverfahren. Rapid Prototyping. Rapid Tooling, Rapid Manufacturing, Hanser-Verlag, München

Gebhardt, A., C. Brücker, and F.-M. Schmitt (2005) RP gestützte Herstellung komplexer transparenter Hohlräume für die Strömungsanalyse. RTE E- Journal Ausgabe 2, www.rtejournal.de (Last access 12/2009)

Gering, D., A. Nabavi, R. Kikinis, N. Hata, and L. O'Donnell (2001). An integrated visualization system for surgical planning and guidance using image fusion and an open MR. Journal of Magnetic Resonance Imaging 13:967–975

Giannatsis, J. and V. Dedoussis (2007) Additive fabrication technologies applied to medicine and health care: a review. International Journal of Advanced Manufacturing Technology 40(1-2):116-127

Gibson, S., J. Samoski, A. Mor, C. Fyock, E. Grimson, T. Kanade, R. Kikinis, H. Lauer, N. McKenzie, S. Nakajima, H. Ohkami, R. Osborne, and A. Sawada (1997) Simulating arthroscopic knee surgery using volumetric object representations, real-time rendering and haptic feedback. In: Proceedings of first joint conference CVRRMed-MR-CAS´97, Grenoble, pp. 369-378, Springer-Verlag Berlin, Heidelberg, New York

Gibson, I. (2005a) Advanced manufacturing technology for medical applications. John Wiley & Sons Inc., New York, USA

Gibson, I. (2005b) Rapid prototyping a review. International Conference on Advanced Research in Virtual and Rapid Prototyping. In: Bartolo et al.; Taylor & Francis, Leiden, The Netherlands

Gibson, I., L.K. Cheung, S.P. Chow, W.L. Cheung, S.L. Beh, M. Savalani, and S.H. Lee (2006) The use of rapid prototyping to assist medical applications. Rapid Prototyping Journal 12:1

Gibson, I., D.W. Rosen, and B. Stucker (2010) Additive Manufacturing Technologies: Rapid Prototyping to Direct Digital Manufacturing. Springer-Verlag Berlin, Heidelberg, New York

Glantz, K., N.I. Durlach, R.C. Barnett, and W.A. Aviles (1997) Virtual reality (VR) and psychotherapy: opportunities and challenges. Presence: Teleoperators and Virtual Environments 6:87-105

Glombitza, G., H. Evers, S. Hassfeld, U. Engelmann, and H.P. Meinzer (1999) Virtual surgery in a (tele-) radiology framework. IEEE Transactions on Information Technology in Biomedicine 3:186-196

Gray, H. (2000) Anatomy of the human body. Philadelphia: Lea & Febiger, 1918; Bartleby.com. www.bartleby.com/107/ (Last access 12/2009)

Greenleaf, W.J. and T. Piantanida (2000) Medical applications of virtual reality technology. In: Bronzino J.D. (ed), The Biomedical Engineering Handbook, 2nd ed, pp. 69.1–69.23. CRC Press, Boca Raton, USA

Grönemeyer, D.H.W., R.M.M. Seibel, A. Schmidt, A. Melzer, and M. Deli (1996) Two and three dimensional imaging for interventional MRI and CT guidance. In: Studies in Health Technology and Informatics 29, Weghorst, S.J., Sieburg, H.B., Morgan, S.B. IOS Press, Amsterdam-Oxford-Tokyo-Washington DC, pp. 62-76

Günther, R. (2002) Entwicklung eines Assistenzrobotersystems für die Knieendroprothetik. Forschungsbericht iwb, Band 165, Herbert Utz Verlag, München

Hahn, I., P.W. Scherer, and M.M. Mozell (1993) Velocity profiles measured for airflow through a large-scale model of the human nasal cavity. Journal of Applied Physiology 75:2273-2287

Handels, H., J. Ehrhardt, W. Plötz, and S.J. Pöppl (2000) Virtual planning of hip operations and individual adaption of endoprostheses in orthopedic surgery. International Journal of Medical Informatics 58-59:21-28

Hastrich, M. (2006) Untersuchung der Einflussparameter bei der Herstellung optisch transparenter Modelle mittels Fräsen als quasi-generativem Rapid Prototyping- Verfahren. Dissertationsschrift Universität Duisburg-Essen

Hess, M.M., J. Lamprecht, and S. Horlitz (1992) Experimentelle Untersuchung der Strombahnen in der Nasenhaupthöhle des Menschen am Nasen-Modell. Laryngo-Rhino-Otologie 71

Hierl, T., G. Wollny, F.P. Schulze, E. Scholz, J.G. Schmidt, G. Berti, J. Hendricks, and A. Hemprich (2006) CAD/CAM implants in esthetic and reconstructive craniofacial surgery. Journal of Computing and Information Technology 1:65-70

Hieu, L.C., N. Zlatov, J. Vander Sloten, E. Bohez, L. Khanh, P.H. Binh, P. Oris, and Y. Tashev (2005) Medical rapid prototyping applications and methods. Assembly Automation 25(4):284-292

Hörschler, I., C. Brücker, W. Schröder, and M. Meinke (2006) Investigation of the impact of the geometry on the nose flow. European Journal of Mechanics: Fluids 25:471-490

Hofmann, E. (2005) Anatomy of nose and paranasal sinuses in sagittal computed tomography. Clinical Neuroradiology 15:258-64

Hopkins, L.M., J.T. Kelly, A.S. Wexler, and A.K. Prasad (2000) Particle image velocimetry measurements in complex geometries. Experiments in Fluids 29:91-95

Hounsfield, G. (1980) Computed medical imaging: Nobel lecture. Journal of Computer Assisted Tomography 4(5):665-674

Hu, Y. (2005) The role of three-dimensional visualization in surgical planning of treating lung cancer. Proceedings 2005 IEEE Eng. in Medicine and Biology 27th Ann. Conf. Shanghai. 646-649

Hüter-Becker, A. and M. Dölken (2005) Physiotherapie in der Orthopädie (Taschenbuch). Auflage 1, Thieme Verlag, Stuttgart

ISO 3002 (part 1-5) (1982) Basic quantities in cutting and grinding. International Organization for Standardization, Geneva, Switzerland

ISO 10791 (part 1-10) (1998) Test conditions for machining centres. International Organization for Standardization, Geneva, Switzerland

Jetschny, W., C. Schöne, J. Hoffmann, and D. Fichtner (2003) Technologietransfer zu Ur- und Umformwerkzeuge. Ausgabe Nr.1, TU Dresden, http://mciron.mw.tu-dresden.de/cimtt/urum/letter/2003_01.pdf (Last access 12/2009)

Jones, A.S., D.J. Willatt, and L.M. Durham (1989) Nasal airflow: resistance and sensation. The Journal of Laryngology and Otology 103:909-911

Jourdan, F. and A. Sabida (2009) An implicit numerical method for wear modeling applied to a hip joint prosthesis problem. Computer Methods in Applied Mechanics and Engineering 198(27-29):2209-2217

Kalender, W.A. (1995) Thin-section three-dimensional spiral CT: Is isotropic imaging possible? Radiology 197:578-580

Kang, M., H. Sadri, L. Moccozet, N. Magnenat-Thalmann, and P. Hoffmeyer (2002) Accurate simulation of hip joint range of motion. Proceedings of Computer Animation, Geneva, Switzerland

Kayser, R. (1895) Die exakte Messung der Luftdurchgängigkeit der Nase. Archiv für Laryngologie und Rhinologie 3:101-120

Kelly, J.T., A.K. Prasad, and A.S. Wexler (2000) Detailed flow patterns in the nasal cavity. Journal of Applied Physiology 89:323–337

Kief, H.B. (2005) NC/CNC Handbuch 2005/2006. Hanser Verlag, München

Kim, S.K. and S.K. Chung (2004) An investigation on airflow in disordered nasal cavity and its corrected models by tomographic PIV. Measurement Science and Technology 15:1090-1096

Kim, J. K., J-H. Yoon, C.H. Kim, T.W. Nam, D. B. Shim, and H.A. Shin (2006) Particle image velocimetry measurements for the study of nasal airflow. Acta Oto-Laryngologica 126:282–287

Kirschner, M. (2006) Marching Cubes. Erstellung von Polygonmodellen aus Voxelgittern http://www.cs.uni-paderborn.de/fileadmin/Informatik/AG-Domik/teaching/lectures/ws0607_advanced_ topics/downloads/mcubes.pdf (Last access 12/2009)

Klein, L.W. (2000) Computerized patient simulation to train the next generation of interventional cardiologists: Can virtual reality take the place of real life? Catheterization and Cardiovascular Intervention 51(4):528-528

Kliegis, U., R. Ascherl, and H. Kärcher (1995) Anatomical models in surgery planning – applications and manufacturing techniques. In: Lemke, H.U., Inamura, K., Jaffe, C.C., Vannier, M.W. (Eds): Computer Assisted Radiology, pp. 1309. Springer-Verlag Berlin, Heidelberg, New York

Kloss, J.H., R. Rockwell, K. Szabo, and M. Duchrow (1998) VRML97. Der neue Standard für interaktive 3D-Welten im World Wide Web, Addison Wesley Longman Verlag GmbH Bonn, Paris, New York, Sydney

Knaur, D. (1988) Lexikon der Technik, Band 2. Droemersche Verlagsanstalt, München

Kurtz, S., F. Mowat, K. Ong, N. Chan, E. Lau, and M. Halpern (2005) Prevalence of primary and revision total hip and knee arthroplasty in the united states from 1990 through 2002. The Journal of Bone and Joint Surgery 87:1487-1497

Lee, T., C.H. Lin, and H.Y. Lin (2001). Computer-aided prototype system for nose surgery. IEEE Transaction on Information Technology in Biomedicine 5:271-278

Lee, T., C. Yan, and M.T. Chi (2007). Stylized rendering for anatomic visualization. IEEE Computing in Science & Engineering 9(1):13-19

Lightman, A.J., B. Vanassche, P. D´Urso, and Y. Shinjiro (1995) Applications of rapid prototyping to surgical planning: a survey of global activities; Proceedings of the 6th International Conference on Rapid Prototyping, pp. 43-49, Dayton, USA

Lill, W., P. Solar, C. Ulm, G. Watzek, R. Blahout, and M. Matejka (1992) Reproducibility of thee-dimensional CT-assisted model production in the maxillofacial area. British Journal of Oral and Maxillofacial Surgery 30:233-236

Lin, R.S. (2002) Adaptive slicing for rapid prototyping. In: Gibson (Eds.): Software Solutions for Rapid Prototyping, Professional Engineering Publishing Limited London and Bury St Edmunds, UK

Lorensen, W.E. and H.E. Cline (1987) Marching cubes: A high resolution 3D surface construction algorithm. Computer Graphics 21(4):163-169

Lorenzen, J. and F. Breitinger (1997) Rapid Tooling – Verfahren zur schnellen Herstellung von Prototypenwerkzeugen. Euroforum Konferenz, Rapid Prototyping, Bad Homburg. http://www.apppex.com/de/knowhow/artikel3.htm (Last access 12/2009)

Lubnau, J. (2009) Konzept zur Unterstützung des Produktentwicklungsprozesses mittels Virtual Reality. Dissertationsschrift Universität Duisburg-Essen

Naito, K., P. Cole, R. Chaban, and D. Oprysk (1988). Nasal resistance, sensation of obstruction, and rhinoscopic findings compared. American Journal of Rhinology, 2:65-69

Ma, D., F. Lin, and C.K. Chua (2001) Rapid prototyping applications in medicine. Part 2: STL file generation and case studies. International Journal of Advanced Manufacturing Technology 18:118-127

Malladi, R. and J.A. Sethian (1995) Image processing via level set curvature flow. Proceedings of the National Academy of Sciences of the United States of America 92(15):7046–7050

Mallepree, T. and D. Bergers (2008) The process accuracy of reconstructed biomodels produced with the quasi-generative rapid prototyping technology. In: Conference proceedings 5th International Conference on Computer Aided Surgery around the Head, Leipzig

Mallepree, T. and D. Bergers (2009a) Complex anatomies in medical rapid prototyping. In: IFBME proceedings Vol. 23, Springer-Verlag Berlin, Heidelberg, New York

Mallepree, T. and D. Bergers (2009b) Advanced pre-surgery planning by animated biomodels in virtual reality. In: IFBME proceedings Vol. 23, Springer-Verlag Berlin, Heidelberg, New York

Mallepree, T. and D. Bergers (2009c) Accuracy of medical RP models. Rapid Prototyping Journal 15(5):325-332

Mallepree, T. and D. Bergers (2009d) Pre-surgery planning in orthopedics by means of medical rapid prototyping. In: Conference proceedings 11th International Essen Symposium on Biomaterials (BIOMAT), Essen

Mallepree, T., D. Bergers, and J. Lamprecht (2010) Virtual applications in ENT medicine in virtual environments. In: Computer Science Research and the Internet. Nova Science Publisher Inc., New York, USA

Mankovich, N.J., A.M. Cheeseman, and N.G. Stoker (1990) The display of three-dimensional anatomy with stereolithographic models. Journal of Digital Imaging 3:200-203

Masing, H. (1966) Experimentelle Untersuchungen über die Strömung im Nasenmodell. Archiv klin. exper. Ohren-, Nasen-und Kehlkopfheilk. 189:59-70

Michaeli, W. (1999) Einführung in die Kunststoffverarbeitung. Carl Hanser Verlag, München

Murphy, S.B. et al. (1985) Computer assisted pre-Operative planning of orthopaedic reconstructive surgery. Proceedings of the International Symposium CAR´85, H.U. Lemke, M.L. Rhodes, C.C. Jaffe, R. Felix, Eds., Springer-Verlag Berlin, Heidelberg, New York

NIH (1997) Working definition of bioengineering. http://www.bmes.org/ (Last access 12/2009)

Noorani, R. (2005) Rapid prototyping – principles and applications. John Wiley & Sons Inc., New York, USA

Preim, B. and D. Bartz (2007) Visualization in medicine. The Morgan Kaufmann Series in Computer Graphics, Elsevier Inc., Burlington, USA

Prokop, M., M. Galanski, C. Schaefer-Prokop, and A.J. van der Molen (2006) Ganzkörper- Computertomographie: Spiral- Multislice- CT. Thieme, Stuttgart

Raphan, Kai. (2004) Integration des DICOM- Standards in ein Programm zur 3D-Gefässrekonstruktion, Diplomarbeit FH- Giessen- Friedberg. http://www.fh-giessen-friedberg.de/imps/content/category/6/19/12/ (Last access 12/2009)

Robb, R.A. (2008) Medical imaging and virtual reality: a personal perspective. Virtual Reality 12:235-257

Russ, J.C. (2006) The image processing handbook. Taylor & Francis, CRC Press, Boca Raton, USA

Said, R., J. Chang, P. Young, G. Tabor, and S. Coward (2008) Image-based meshing of specific patient data. In IEEE proceedings International Conference on Bioinformatics and Biomedical Engineering pp. 1672-1676, Shanghai, China

Sauer, A., F. Beneke, D. Bergers, and G. Witt (2005) Modelle und Prototypen für die Medizin, RTE Journal Ausgabe 2, www.rtejournal.de (Last access 12/2009)

Schreck, S., K.J. Sullivan, C.M. Ho, and H.K. Chang (1993) Correlations between flow resistance and geometry in a model of the human nose. Journal of Applied Physiology 75:1767-1775

Schroeder, W.J., J. Zarge, and W.E. Lorensen (1992) Decimation of triangle meshes. Computer Graphics (SIGGRAPH '92) 26(2):65-70

Schwarz, O., F.W. Ebeling, H. Huberth, H. Schirber, and N. Schlör (2005) Kunststoffkunde. Vogel Verlag, Würzburg

Shi, H., W.C. Scarfe, and A.G. Farman (2006) Maxillary sinus 3D segmentation and reconstruction from cone beam CT data sets. International Journal of Computer Assisted Radiology and Surgery 1:83–89

Soille, P., and H. Talbot (2001) Directional morphological filtering. IEE Transactions on Pattern Analysis and Machine Intelligence 23:1313-1329

Sonek, C. (2004) Entwicklung eines 3D-Visualisierungstools für medizinischen Bilddaten-Redesign, Funktionserweiterung und Integration in das Teleradiologiesystem CHILI, Diplomarbeit Deutsches Krebsforschungszentrum Heidelberg. Technical Report 153. http://www.dkfz-heidelberg.de/de/mbi/pub/tr.html (Last access 12/2009)

Spur, G. and T. Stöferle (1979) Handbuch der Fertigungstechnik (Band 3/1). Carl Hanser Verlag, München

Standke, J. (2008) Rechnergestützte Auslesung von reversiblen Fügetechniken für quasi-generativ hergestellte Funktionsprototypen. Dissertationsschrift Universität Duisburg-Essen

Székely, G. and R.M. Satava (1999) Virtual reality in medicine. British Medical Journal 319:1305-1308

Tashev, Y. (2005) Medical rapid prototyping applications and methods. Assembly Automation 25(4):284-292

Taylor, R.H. (1993) An overview of computer assisted surgery at IBM. T.J. Watson Research Center. Research Report RC 19166 (83465), IBM Research Division, Yorktown Heights, New York

Tillmann, B.N. (2009) Atlas der Anatomie des Menschen. Springer-Verlag Berlin, Heidelberg, New York

Tonndorf, J. (1938) Der Weg der Atemluft in der menschlichen Nase. European Archives of Oto-Rhino-Laryngology 146 (1): 41-63

Truscott, M, D. de Beer, G. Vicatos, K. Hosking, L. Barnard, G. Booysen, and I. Campbell (2007) Using RP to promote collaborative design of customized medical implants. Rapid Prototyping Journal 13(2):107-114

Vartanian, A., J. Holcomb, Z. Ai, M. Rasmussen, M.E. Tardy, and J.R. Thomas (2004) The virtual nose. Archives of Facial Plastic Surgery 6:328-333

Verdonschot, N.J.J, R. Huiskes, and M.A. Freeman (1993) Pre-clinical testing of hip prosthestic designs: A comparison of finite element calculations and laboratory tests. Proceedings of the Institution of Mechanical Engineers, Part H: Journal of Engineering in Medicine 207:149-154

Wagenmann, M. (2002) Prognostische und pathophysiologische Faktoren der chronischen Nasennebenhöhlenentzündung. Habilitationsschrift, Hohe Medizinische Fakultät der Heinrich-Heine-Universität Düsseldorf

Wang, C.S., C.Y. Hsiao, T.R. Chang, and C.K. Teng (2007) STL mesh reconstruction for bio-medical rapid prototyping model. IEEE International Conference on Systems, Man and Cybernetics (ISIC), Montreal, Canada

Wetzel, S., M. Ohta, A. Handa, J.M. Auer, P. Lylyk, K.O. Lovblad, D. Babic, and D.A. Rufenacht (2005) From patient to model: Stereolithographic modeling of the cerebral vasculature based on rotational angiography. American Journal of Neuroradiology 26:1425-1427

Wiltgen, M. (1999) Digitale Bildverarbeitung in der Medizin. Shaker-Verlag, Aachen

Wimmer, D. (1989) Kunststoffgerecht konstruieren. Hoppenstedt Technik Tabellen Verlag, Darmstadt

Wulf, J., K.D. Vitt, and C.M. Erben (2001) Analysis of data collected in the phidias validation study. Phidias Newsletter No. 7, www.materialise.com (Last access 12/2009)

Wulf, J., K.D. Vitt, H.-B. Gehl, and L.C. Busch (2001) Anatomical accuracy in medical 3D modeling. Materialise Archive (Gazette) Leuven, www.materialise.com (Last access 12/2009)

Zäh, M.F. (2006) Wirtschaftliche Fertigung mit der Rapid- Technologien Anwender-Leitfaden zur Auswahl geeigneter Verfahren. Carl Hanser Verlag, München

Zajtchuk, R., and R. Satava (1997) Medical applications of virtual reality. Communications of the ACM 40(9):63-64

Zhan C., R. Kaczmarek, N. Loyo-Berrios, J. Sangl, and R. Bright (2007) Incidence and short-term outcomes of primary and revision hip replacement in the united states. The Journal of Bone and Joint Surgery 89:526-533

Zhang C., M. Zhou, and J. Gao (2001) Conversion between discrete images and organized 3D file formats. pp. 2835-2839. IEEE International Conference on Systems, Man and Cybernetics (ISIC), Montreal, Canada

List of Figures

List of Tables